STUDY OF THE POLAR CAP PLASMA FLOWS WITH THE CLYDE RIVER SUPERDARN RADAR

A Thesis Submitted to the College of

Graduate and Postdoctoral Studies

in Partial Fulfillment of the Requirements

for the Degree of Master of Science

in the Department of Physics and Engineering Physics

University of Saskatchewan

Saskatoon

By

Peter Bankole

PERMISSION TO USE

In presenting this thesis in partial fulfillment of the requirements for a Postgraduate degree from the University of Saskatchewan, I agree that the Libraries of this University may make it freely available for inspection. I further agree that permission for copying of this thesis in any manner, in whole or in part, for scholarly purposes may be granted by the professor or professors who supervised my thesis work or, in their absence, by the Head of the Department or the Dean of the College in which my thesis work was done. It is understood that any copying or publication or use of this thesis or parts thereof for financial gain shall not be allowed without my written permission. It is also understood that due recognition shall be given to me and to the University of Saskatchewan in any scholarly use which may be made of any material in my thesis.

Requests for permission to copy or to make other use of material in this thesis in whole or part should be addressed to:

Head of the Department of Physics and Engineering Physics
Physics Building
116 Science Place
University of Saskatchewan
Saskatoon, Saskatchewan S7N 5E2
Canada

OR

Dean
College of Graduate and Postdoctoral Studies
University of Saskatchewan
116 Thorvaldson Building, 110 Science Place
Saskatoon, Saskatchewan S7N 5C9
Canada

ABSTRACT

Plasma flows in the high latitude ionosphere reflect complex physical processes occurring when the Sun-originated solar wind blows around the Earth. One way of monitoring and quantifying these flows is to use Doppler velocity measurements with ground-based high-frequency (HF) radars such as the Super Dual Auroral Radar Network (SuperDARN) radars.

The research presented in this thesis includes two major topics. First, we investigate quality of SuperDARN HF velocity measurements for a relatively new radar in the network, the Clyde River (CLY) radar. This has never been done in the past while the radar is critical in the network as its field of view allows one to measure plasma flow velocity roughly along magnetic parallels at extremely high latitudes. Second, after successfully validating the Clyde River radar measurements, variations in the plasma flows at radar latitudes are investigated.

To accomplish the first task, measurements of the plasma velocity collected over the year 2016 at Clyde River are compared with nearly simultaneous velocity measurements from the Resolute Bay Incoherent Scatter Radar-Canada (RISR-C). Our results show that the CLY radar velocity measured in beams 4-6 is statistically comparable to the $\mathbf{E \times B}$ component of the plasma drift along these beams (azimuthal plasma flows) measured by the RISR-C. The agreement between the two types of radars was found to be not ideal; the lines of linear fit had slopes in the range of 0.5-0.7. This is comparable with the slopes in other experiments, but slightly lower than usual. We showed that the correction of HF velocities for the index of refraction effect does not increase the slope of the line to 1 mostly because of lower HF velocities at large $\mathbf{E \times B}$ drifts of > 700 m/s. This "underestimation" effect was found to be stronger at nighttime and its compensation by considering the index of refraction effect was less successful than at daytime. We carried out a similar comparison between Rankin Inlet (RKN) SuperDARN radar velocity measurements and that of RISR for the same period of 2016 and found reasonably good agreement as well. We showed that the strongest disagreements between HF and RISR-C velocity occurred for periods with very low CLY and RKN velocities, below 100-200 m/s in magnitude, indicating that some ionospheric echoes could be misidentified by the SuperDARN radar processing technique; this effect is more pronounced for the RKN radar. Finally, we investigated self-consistency of SuperDARN HF measurements by comparing velocities of the CLY radar and the SuperDARN radar at Inuvik (INV) in about the same direction. We found that the CLY-INV agreement is

reasonable for ranges of >1000 km with pure F region echo detection by both radars. Evidence is presented that measurements at short ranges of <800 km, that are traditionally thought to be pure F region scatter as well, is sometimes contaminated with scatter from the E region with velocities below the $\mathbf{E}\times\mathbf{B}$ drift.

On the second task, we considered multi-year CLY data set to assess seasonal variation of the plasma flow velocity in the azimuthal direction, at magnetic latitudes of $\sim 81^\circ$ and at southward orientation of solar-related interplanetary magnetic field (IMF) $B_z < 0$. We noticed several changes from winter to summer and found them to depend on the polarity of the IMF azimuthal component B_y. For IMF $B_y < 0$, we report that summer CLY velocities stay positive much longer over a day duration. For IMF $B_y > 0$, CLY velocities remain much longer negative. In general, we found that CLY velocity data in the azimuthal direction can be interpreted in terms of a more "round" overall pattern in summer.

ACKNOWLEDGMENTS

First of all, I would like to express my sincere gratitude and appreciation to my supervisor, Professor Alexandre Koustov for his advice and guidance in the course of my studies. His immeasurable assistance, positive criticisms, and helpful suggestions, during my MSc program, proved very helpful in understanding the fundamental physics of the ionosphere and the operations of the radar system. Without his support and generous funding for this research, this thesis would not have been completed, and for all these, I am forever grateful.

I would like to also thank Dr. Pasha Ponomarenko for his continual help during this entire work. Our numerous discussions have pushed me to expand my limits and abilities. Also, I thank him for his invaluable technical support with respect to programming.

I thank my Advisory Committee members, Prof. Glenn Hussey, Prof. Chijin Xiao, and Prof. Rob Pywell for their helpful suggestions, comments, and guidance.

I am incredibly grateful for the financial support which I received from the Department of Physics and Engineering Physics and the Institute of Space and Atmospheric Studies at the University of Saskatchewan, and Gerhard Herzberg Fund. Thank you, Cindy Jelinski, Debbie Parker and Marj Granrude for your administrative support and assistance in providing the required degree information and right documentation.

Thank you to my dear parents for their infinite love and many sacrifices they made for the sake of our future and to my beautiful sisters Catherine Bankole, Mary Bankole and Elizabeth Bankole for their love, care, and prayers. I cannot express how grateful I am for having such an amazing family.

I say a huge thank you to all my friends, especially Ridley Clifford, Draven Galeschuk, Maxworth Ashanthi, Kingsley Nwabufo, Hammed Ejalonibu, Stephen Owuamanam, Jude Okolie, and all those whose names I have not written; I am sincerely grateful to you all, God bless you.

CONTENTS

LIST OF TABLES

LIST OF FIGURES

LIST OF ABBREVIATIONS

ACF	Autocorrelation Function
AMIE	Assimilative Mapping of Ionospheric Electrodynamics
CADI	Canadian Advanced Digital Ionosonde
CLY	Clyde River
CPCP	Cross Polar Cap Potential
DMSP	Defense Meteorological Satellites Program
EISCAT	European Incoherent Scatter Radar
FB	Farley Buneman
FFT	Fourier Transform
FoV	Field-of-View
GD	Gradient-Drift
GSM	Geocentric Solar Magnetospheric
HF	High Frequency
HMB	Heppner-Maynard Boundary
IMF	Interplanetary Magnetic Field
INV	Inuvik
l-o-s	Line-of-Sight
MLAT	Magnetic Latitude
MLT	Magnetic Longitude
PolarDARN	Polar Dual Auroral Radar Network
RB	Resolute Bay
RISR-C	Resolute Bay Incoherent Scatter Radar Canada
RKN	Rankin Inlet
STARE	Scandinavian Twin Auroral Radar Experiment
SuperDARN	Super Dual Auroral Radar Network
SW	Solar Wind
UHF	Ultra High frequency
UT	Universal Time
VHF	Very High frequency

LISTS OF SYMBOLS AND CONSTANTS

A_m	Amplitude
$\mathbf{B}$	Magnetic field
c	Speed of light ($2.9979\times10^8 m/s$)
C_s	Acoustic speed
$D_\perp$	Diffusion coefficient
e	Electron charge
$\mathbf{E}$	Electric field
$\mathbf{E_{sw}}$	Electric field of solar wind
f_D	Doppler shift
f_p	Plasma frequency
f_r	Radar frequency
f_T	Frequency of transmitted radio wave
$\mathbf{g}$	Gravitational acceleration
$\mathbf{k}$	Wave vector
$\mathbf{k_i}$	l-o-s direction of the radar beam associated with the observed gridded velocity
$\boldsymbol{k}^i$	Tensor of unit vectors for radar directions in a selected coordinate system
k_s	Wavenumber of scattered wave
$\mathbf{k}_\perp$	Wave vector in the perpendicular direction
L	Scale of the plasma gradient
m_α	Mass of species (ions or electrons)
n	Index of refraction
N	Number of points on the individual map
n_e	Local electron density in m^{-3}
$\mathrm{n}\alpha$	Number density
p_λ	Power of Lorentzian FITACF at time lag $\tau = 0$
p_Σ	Power of Gaussian FITACF at time lag $\tau = 0$
p_0	Maximum power
q_α	Charge of species (ions or electrons)
R	Ratio of SuperDARN HF velocity to RISR velocity
t	Time
T_e	Electron temperature (eV)
T_i	Ion temperature
$\mathrm{T}\alpha$	Temperature in units of energy (eV)
$\mathbf{U}_\mathrm{n}$	Neutral wind velocity

Vel_{HF}	SuperDARN HF velocity
$\mathbf{v_M}$	Merged velocity magnitude
Vel_{RISR}	RISR velocity
$\mathbf{V_{sw}}$	Velocity of solar wind
$\mathbf{V}_\alpha$	Velocity of fluid species
V_0	Collisionless plasma speed of motion in crossed electric and magnetic fields
V//	Velocity parallel to the magnetic field
W_λ	Lorentzian spectral width
W_Σ	Gaussian spectral width
α	Angle between the radar l-o-s and the perpendicular of the magnetic field
α_o	Aspect angle
γ	Growth rate
$\delta\mathbf{E}$	Polarisation electric field
εl	Elevation angle
ε_0	Permittivity of free space
θ_1	Angle between radar beam and the merged velocity direction
λ_D	Debye length
$\nu_{\alpha n}$	Species collision frequency with neutrals
ν_{ei}	Electron-ion collision frequency
ν_i	Full velocity vector
ν_{irr}	Velocity of the irregularity
ν_{los}	Line of sight velocity from radar
σ_i	Velocity error
τ	Pulse lag time
ϕ	Phase of the Autocorrelation function
$\Delta\varphi$	Phase shift due to path length difference
Φ	Electric potential
Φ_{PC}	Cross polar cap potential
χ^2	Minimization parameter
ψ	Angle between the two radar beams for merge technique
Ω_α	Gyro frequency of species
ω	Angular frequency
ω_D	Doppler frequency
ω_r	Radial frequency
ρ	Plasma density

CHAPTER 1

INTRODUCTION

The Sun provides the Earth with the heat and light that renders the Earth habitable. Invisible to that life, however, is the constant stream of energetic particles continuously ejected from the Sun and moving toward the near-Earth environment at supersonic speed. The interaction between this stream of particles (collectively acting as a plasma fluid) and the Earth's magnetic field initiates a number of electrodynamic processes, for example, charged particle acceleration and precipitation into the upper atmosphere resulting in significant increase in the ionization of the upper atmospheric layer, the ionosphere. The ionosphere, stretching from about 50 km to 1000 km, is an integral part of the Earth's environment because it provides an electrical linkage between the charged particles in the solar wind and the neutral particles in the upper atmosphere. On a practical side, the ionosphere supports radio wave propagation so that communication is possible on the ground and in space. Modern communication technologies such as GPS navigation systems and HF radio links depend on the state of the ionosphere, and it is not a surprise that the effects of the solar wind flow around the Earth are becoming, more and more, of interest to practitioners and not only to pure scientists. An entirely new branch of science, Space Weather, and its forecasting is rapidly developing.

Space weather includes several elements. One of these is charged particle (or plasma) circulation at high latitudes. Because of continuous plasma motion, significant volumes of the high-density ionosphere from the sunlit dayside part can detach and set on a global motion, from the dayside to the nightside, bringing high-density blobs, known as polar cap patches, into the otherwise highly-depleted ionosphere at the near North/South Pole areas. Forecasting of such patches development is important for practical applications. The work in this area has been ongoing for years, but patch forecasting remains a formidable task for space weather researchers.

The solar wind flow around the Earth results in a redistribution of charged particles in nearby space so that a special cavity, the magnetosphere, is formed where the particle motion is governed by electric and magnetic fields. A number of special regions within the magnetosphere with common properties have been identified.

It was also discovered that various magnetospheric regions are electrically connected by means of electric currents, and some of the current loops are closed through the ionosphere. As a result, various processes in the magnetosphere are replicated in the ionosphere, making it convenient to investigate the near-Earth's environment by looking at the processes in the ionosphere. The global-scale motion of ionospheric plasma driven by the electric fields, which originated in the solar wind, within the magnetosphere is one such process. Studies of plasma motions in the ionosphere are therefore essential for understanding the physics of solar-terrestrial interactions.

1.1 The Sun-Earth environment

Below we introduce major elements of the Sun-Earth environment, describe their characteristics and discuss some ongoing processes. In the following sections, a description of the solar wind, magnetosphere, and ionosphere is provided following the books by Kelley [2009], Rees [1989], Hargreaves [1992], Kivelson and Russell [1995] and Baumjohann and Treumann [1997].

1.1.1 The solar wind

The solar wind consists mainly of electrons and protons in approximately equal parts, with a small (~ 5% of the total number of particles) admixture of ionized helium and still fewer ions of heavier elements. Near the Earth's orbit (1 AU ~ 150 x 10^6 km), the solar wind has a proton density of ~5 particles per cubic centimeter, and the proton and electron temperatures are of the order of 10^5 K. The solar wind plasma expands outward from the Sun radially at velocities typically around 450 km/s, but can exceed 1000 km/s under strong solar conditions.

E. Parker in 1958 [Parker, 1958] proposed the first theory of solar wind development. He showed that the solar wind flow starts out at a velocity below the ion-acoustic speed (subsonic speed) and quickly becomes supersonic at about four solar radii away from the surface. When arriving at the Earth's environment, it slows down in a transition region called the bow shock (Figure 1.1), and then gets involved with and interacts with the Earth's magnetic field. It was also discovered that the solar wind is highly conductive and carries an embedded magnetic field [Sonett et al., 1960], which is now termed the Interplanetary Magnetic Field (IMF). We discuss the IMF briefly in the next section.

1.1.2 Interplanetary magnetic field and the frozen-in magnetic field concept

The IMF is a part of the Sun's magnetic field that is carried into the interplanetary space by the solar wind. The IMF is a weak field with strength varying from 1 to 30 nT near the Earth's orbit with an average value of ~6 nT. The IMF is a vector quantity, and its components are traditionally defined using the geocentric solar magnetospheric system (GSM) coordinate system where the x-axis points sunward, the z-axis is parallel to the Earth's magnetic dipole, and the y-axis completes a right-handed coordinate system. The IMF lines are said to be "frozen in" to the solar wind plasma, i.e., the magnetic flux is carried unchanged in each parcel of the moving plasma. This is explained by the fact that in the time it takes the solar wind to travel from the Sun to the Earth ($\sim 10^{11}$ m), the magnetic field is only able to diffuse a fraction of that distance ($\sim 10^{3}$ m). As a consequence, in a highly conducting plasma, there is no electric field in the frame moving with the plasma. The electric field arises with respect to an observing frame, such as the Earth. This electric field is given by

$$\mathbf{E}_{sw} = -\mathbf{V}_{sw} \times \mathbf{B}, \tag{1.1}$$

where $\mathbf{V}_{sw}$ and $\mathbf{B}$ are the solar wind velocity and IMF respectively. This electric field has a typical value of several millivolts per meter, but it is enhanced by an order of magnitude as it reaches the ionosphere.

1.2 The magnetosphere

As the solar wind approaches the near-Earth environment, it interacts with the Earth's magnetic dipole to form a magnetic cavity called the magnetosphere. On the sunward side of the magnetosphere a shock wave, or the bow shock, is established at ~ $10\,R_E$ (R_E = 6370 km, Earth radius), where the solar wind plasma decelerates to subsonic speeds dissipating the kinetic energy of its particles (Figure 1.1). The shock is essential because it modifies the properties of the solar wind before the flow interacts with the Earth's magnetic field. The solar wind particles then arrive at a transition region, called the magnetosheath, and finally reach the outer boundary of the magnetosphere, known as the magnetopause (Figure 1.1). The front-side of the magnetopause is round and converges towards two points known as the polar cusps, and these are the only points

where the magnetopause connects directly to the Earth's surface and allows solar wind particles direct access to the innermost regions of the magnetosphere and ionosphere.

When the subsonic solar wind reaches the magnetopause with a southward-directed IMF, as depicted in Figure 1.1, the IMF merges with the terrestrial field lines and these field lines become "open" to the solar wind. As the solar wind travels past the magnetosphere, these open field lines are dragged along to the night side forming the magnetotail. The magnetotail (~40 R_E in diameter) is comprised of three main sections, the plasma sheet, and the northern and southern lobes. Figure 1.1 shows the typical sizes of the magnetospheric regions described above. Less evident from this diagram is the fact that the magnetotail can extend up to ~ 100 R_E depending on the solar wind conditions.

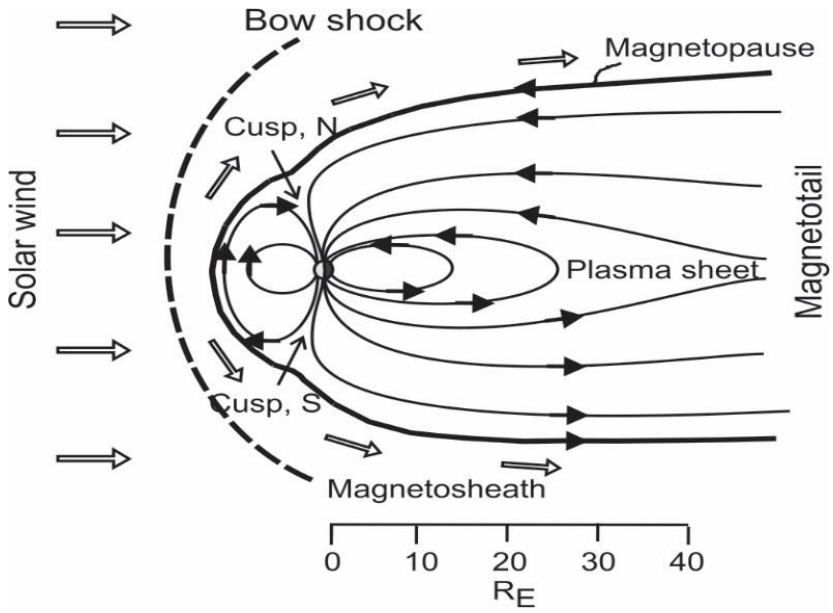

Figure 1.1: A cross-section of the magnetosphere in the plane containing the geomagnetic dipole. Hollow arrows show solar wind flow around the magnetopause. Adapted from Hargreaves [1992].

Of the three main sections of the magnetotail listed above, the plasma sheet is of great significance. This is because here the particles are concentrated and eventually pushed towards the Earth. The central plasma sheet is about 10 R_E thick and is centered in the equatorial plane of the magnetotail separating the oppositely directed magnetic fields of the north and south magnetotail lobes. Particle densities in the plasma sheet are typically of the order of ~0.1 cm^{-3}, and it is

comprised mostly of *H*+ ions and electrons. Typical particle energies lie between 0.1 keV and 10 keV with an average energy of 5 keV for protons and 0.6 keV for electrons [Hargreaves, 1992].

1.3 Solar wind-magnetosphere coupling

The solar wind interacts with the magnetosphere through two physical processes: the quasi-viscous interaction [Axford and Hines, 1961], and reconnection [Dungey, 1961]. In quasi-viscous interaction, the solar wind flows around the egg-shaped magnetosphere dragging along the IMF, see Figure 1.2a. Energy and momentum are transferred from the solar wind to the outer magnetosphere causing anti-sunward flow in the boundary layer of the enclosed plasma. Because the system is closed, the flow reverses in the magnetotail causing the plasma to move toward and around the inner magnetosphere (circular region). Energy and momentum of the sunward motion of the inner edge of the outer magnetosphere are transferred to the outer edges of the inner magnetosphere. This flow reverses on the dayside, causing anti-sunward flow in the central region of the inner magnetosphere.

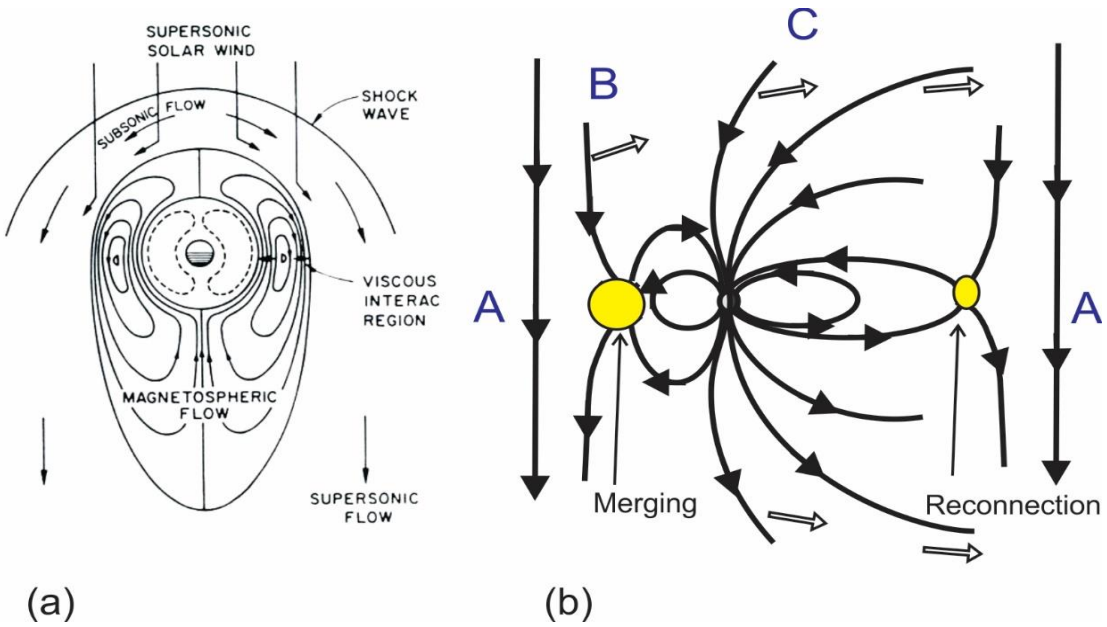

Figure 1.2: Solar wind-magnetosphere interaction processes: (a) quasi-viscous interaction (from Kelley [2009]) and (b) reconnection process for a southward IMF (adapted from Craven [1997] and Mori [2011]). Yellow circles indicate regions where magnetic field reconnection processes occur.

Reconnection is a process that occurs in plasma where magnetic field lines from different domains can couple and form two topologically different field lines. This occurs at the front side

magnetopause when the southward oriented IMF ($B_z < 0$) line (B) approaches the northward-oriented geomagnetic field line at the front-side magnetosphere. The geomagnetic field lines are closed with both ends connected to the Earth. When the anti-parallel lines meet, the net field goes to zero, and the IMF and geomagnetic field lines interconnect in the reconnection region (yellow shading) to form an open magnetic field line (C) in either hemisphere. "Merging" is the term often used for the dayside process. The open field lines are then carried downstream by the solar wind and stretched into a long cylindrical tail. Eventually, the open field lines close again by reconnection in the center of the magnetotail (smaller circle) in Figure 1.2b. After reconnection, some of the open field lines are converted back to regular IMF lines in the solar wind (line A on right in Figure 1.2b). The remainder of the reconnected lines become closed terrestrial field lines. These field lines shrink as they move sunward along the magnetosphere flanks and eventually get into the dayside subsolar part of the magnetosphere, where they become subject to the dayside merging), and this cycle repeats over and over again.

About 50% of the time the IMF is oriented northward and the above frontside –magnetotail reconnection (Dungey) cycle cannot occur. However, reconnection processes can be initiated in the regions called the magnetospheric lobes. The lobes are the outer parts of the magnetopause poleward of the cusp/cleft regions. Lobe reconnection is illustrated in Figure 1.3 for the northern hemisphere geometry.

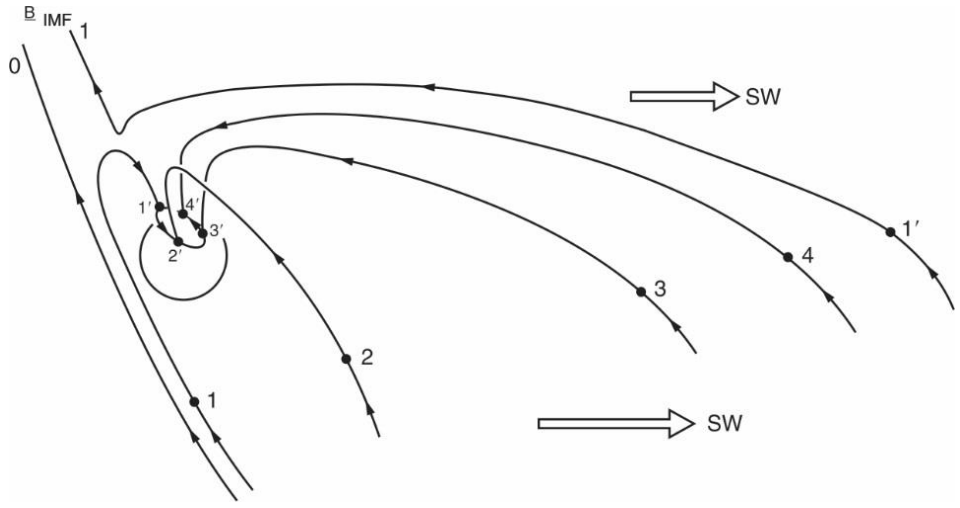

Figure 1.3: Lobe reconnection process for northward IMF that produces a dominant high-latitude convection cell (from Kelley [1989]). Arrows marked as "SW" indicate the solar wind flow.

Magnetic field lines that extend into this region have the right orientation for merging to occur with a northward IMF at position 1. The subsequent antisunward motion of open field lines to points 2 and 3 (along the flanks of the magnetosphere) produces antisunward motion in the ionosphere from $1'$ to $3'$. After passing the magnetospheric flank, the field line remains open and is driven by the solar wind farther down the tail. At this time, the footprint of the line starts moving towards the Sun, from position $3'$ to $4'$. This is because the magnetic flux line has a certain tension. Eventually, the open flux line assumes the position of the original field tube ($1'$-1). Thus, the evolution of magnetic flux line in the magnetosphere (labeled as 1, 2, 3, 4, 1) corresponds to the antisunward flow toward the Earth-Sun line at the magnetopause and sunward flow in the ionosphere, along the path $3', 4', 1'$. At a position $4'$ the flux tube can reconnect again. The convective motions due to lobe reconnection exist in addition to motions driven by the viscous interaction described earlier, and a four-cell convection pattern can occur with two normal cells at lower latitudes and two reverse cells at high latitudes.

Recently, it has been proposed that the lobe reconnection can involve another reconnection process, in the southern hemisphere (e.g., Watanabe and Sofko [2009]). In this scenario, the open flux line, e.g., line 2 in Figure 1.3, can merge with the closed flux line in the southern hemisphere forming a new closed line and a new open line. This process has been termed the "exchange" cycle. Although the circulation pattern at the ionospheric level is still expected to be four-celled, some details are different from the standard lobe reconnection scenario of Crooker [1992], as discussed by Watanabe et al. [2009]. One consequence of the interchange reconnection cycle is the formation of convection cells that cross the open-closed field line boundary twice in one cycle in the hemisphere of IMF-lobe reconnection, and a convection cell circulating exclusively in the closed field line region in the hemisphere of lobe-closed reconnection.

The mode of interaction between the IMF and Earth's magnetic dipole depends on the IMF orientation. Other factors are important as well. When processes in the combined magnetosphere-ionosphere system are studied, information on the IMF and solar wind parameters become crucial. Over the last decade, this information is usually obtained from the so-called OMNI database located at https://omniweb.gsfc.nasa.gov/ow_min.html. The OMNI database comprises data obtained from 4 satellites: ACE, Wind, Geotail and IMP 8. It is continuously updated by NASA's Goddard Space Flight Center personnel. The available parameters include the IMF B_x, B_y and B_z components, solar wind velocity magnitude and components, flow speed, proton density, and

proton temperature. The OMNI dataset also includes additional data from other sources. These include various magnetic indices such as the planetary Kp index, the ring current Dst index, the substorm-characterizing AE index, and the polar cap energy inflow PCN index. Information on some parameters derived from the existing measurements is also given. A good example is the dynamic solar wind flow pressure, which is the product of the plasma density, and squared velocity of the solar wind, $P = \rho V_{SW}^2$.

1.4 The ionosphere

The ionosphere is that part of the upper atmosphere where electrons and ions are present in quantities sufficient to affect the propagation of radio waves [Rishbeth and Garriott, 1969]. It is a quasi-neutral, weakly ionized plasma region stretching from ~ 60 km to ~1000 km, although the limits are not well defined. The existence of the ionosphere is owing to solar ionizing radiation and energetic particle precipitation from the magnetosphere into the atmosphere. The books by Kelley [2009], Rees [1989], Hargreaves [1992], Kivelson and Russell [1995] and Baumjohann and Treumann [1997] are a good introduction into this topic, and these books were used for the formulations and discussions in this section.

1.4.1 Formation of ionospheric layers

The ionosphere is conventionally divided into three distinct regions, the D, E and F regions [Hargreaves, 1992]. Typical electron density profiles for day and night at solar maximum and solar minimum conditions are given in Figure 1.4.

The F region forms the uppermost ionospheric layer extending from ~150 to 350 km, with a peak electron density of ~ 10^6 cm^{-3} at ~250 km. At F region heights atomic oxygen is the most abundant neutral particle. Therefore, photoionization produces an abundance of O^+, resulting in O^+ being dominant. In the absence of photoionization at night time, recombination of ions and electrons result in a depletion of the F region electron density. With increasing solar activity, the daytime F region develops a double peak structure: a weaker layer known as F_1 at ~200 km and, above it, a denser dominant layer called F_2 at ~300 km (See Figure 1.4). Photoionization produces the former, while both photoionization and vertical transport processes control the latter.

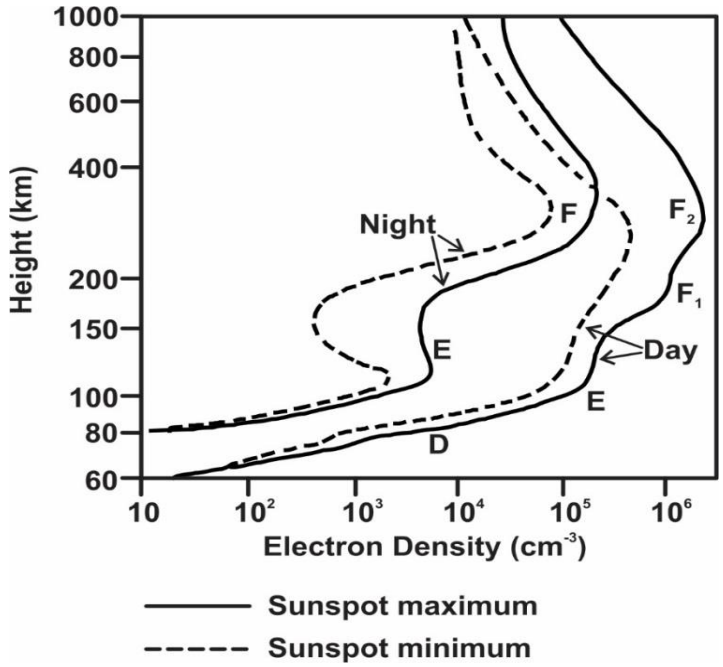

Figure 1.4: Ionospheric electron density profiles for day and night at solar minimum (dashed line) and maximum (solid line) conditions with various layers designated. Adapted from Hargreaves [1992].

The E region forms the middle part of the ionosphere extending from ~ 90 to 120 km with an electron density peak of $\sim 10^5$ cm^{-3} at altitudes of $\sim 120 - 130$ km. At these heights, the dominant neutrals are O, O_2, and N_2, with N_2 being the most abundant. The ionized component is formed primarily due to photoionization and, at high latitudes, ionization by precipitating energetic particles. All three neutrals are photoionized with a reaction such as $X + h\nu \rightarrow X^+ + e^-$, where X represents the neutral species O, O_2, and N_2. Although N_2 is the most dominant neutral, there is no build up of N_2^+, due to an important series of interchange reactions that occur between ionized and neutral N_2 and O. The two most frequent reactions are $N_2^+ + O \rightarrow NO^+ + N$ and $O^+ + N_2 \rightarrow NO^+ + N$, which lead to an accumulation of NO^+ instead of N_2^+. No interchange reaction occurs with O_2^+, which leads to a build-up of O_2^+, and the dominant ions in the E region are then NO^+ and O_2^+. In the absence of photoionization during night hours, recombination of ions and electrons in the E region results in significant weakening and even disappearance of the E layer. In the high-latitude ionosphere, particle precipitation, which can produce some ionization at night time, reduces this effect.

The D region is the lowest ionospheric region extending from ~60 to ~90 km. It has a typical electron density of ~ 10^4 cm^{-3}. Like the E region, the D region contains NO^+ and O_2^+, but these ions only dominate in the uppermost five kilometers of the D region. The D region is also known to contain numerous other positive and negative ions. Also, due to the high neutral density, a chain of complex chemical reactions (three body chemical processes) occurs here. In many cases, the minor species densities and chemical reaction rates are not well known, and this partly explains why the D region is considered separately from the E region, despite the lack of a local peak in the electron density. The D region completely disappears at night in the absence of photoionization.

1.4.2 Ion and electron motions in the ionosphere

Ionospheric plasma is in constant motion. Along with the magnetic field, the electric field and neutral wind are two significant sources that drive this motion. To illustrate their contribution to the velocity of electrons and ions at various heights and their relative importance quantitatively, we consider a configuration with a vertical magnetic field **B**, oriented in the negative *z*-direction, an electric field **E** and neutral wind $\mathbf{U}_n$ directed in the *x* and *y* directions respectively, as shown in Figure 1.5.

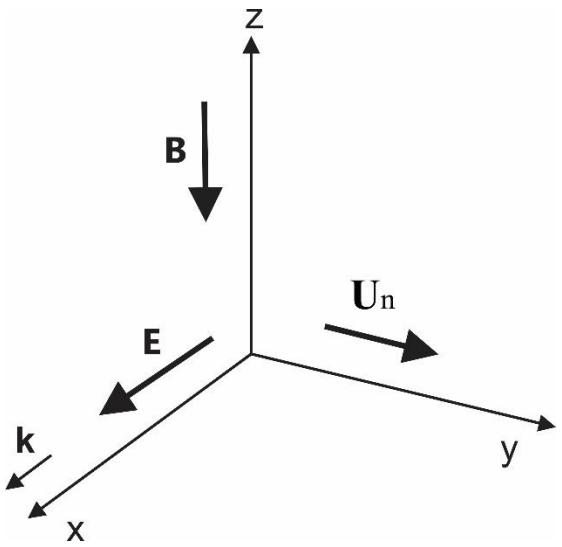

Figure 1.5: Coordinate system showing the configuration of the magnetic and electric fields and background plasma density gradient adopted for the analysis.

The fluid equation of motion in the ionosphere is given by Kelley [2009]

$$m_\alpha \frac{d\mathbf{V}_\alpha}{dt} = q_\alpha \left[\mathbf{E} + \mathbf{V}_\alpha \times \mathbf{B}\right] - m_\alpha \nu_{\alpha n} \left(\mathbf{V}_\alpha - \mathbf{U}_n\right) \pm m_\alpha \nu_{ei} \left(\mathbf{V}_e - \mathbf{V}_i\right) - \frac{\nabla\left(n_\alpha T_\alpha\right)}{n_\alpha} + m_\alpha \mathbf{g}\,, \tag{1.2}$$

where α represents the species, ions or electrons, m_α and q_α are the mass and charge of the species respectively, $\mathbf{V}_\alpha$ is the velocity, $\nu_{\alpha n}$ is the species collision frequency with neutrals, $\mathbf{U}_n$ is the neutral wind velocity, ν_{ei} is the electron-ion collision frequency, n_α is the species number density, T_α is the species temperature in units of energy (eV) and $\mathbf{g}$ is the gravitational acceleration. The third term on the right-hand side of Equation 1.2 describes Coulomb collisions (friction) between electrons and ions; it is positive for ions and negative for electrons. To simplify the analysis, we neglect the electron-ion interactions (which is valid below the F region peak), consider no neutral particle motions, no gravity and neutral wind effects and, finally, also assume the cold plasma approximation ($T_\alpha = 0$). Equation 1.2 then reduces to

$$m_\alpha \frac{d\mathbf{V}_\alpha}{dt} = q_\alpha \left[\mathbf{E} + \mathbf{V}_\alpha \times \mathbf{B}\right] - m_\alpha \nu_{\alpha n} \mathbf{V}_\alpha\,. \tag{1.3}$$

For steady state conditions ($d/dt = 0$), the fluid species velocity $\mathbf{V}_\alpha$ from Equation 1.3 can be written in a form

$$\mathbf{V}_{0\alpha} = \frac{\Omega_\alpha \nu_{\alpha n}}{\Omega_\alpha^2 + \nu_{\alpha n}^2} V_0 \frac{\mathbf{E}}{|\mathbf{E}|} + \frac{\Omega_\alpha^2}{\Omega_\alpha^2 + \nu_{\alpha n}^2} V_0 \frac{\mathbf{E}\times\mathbf{B}}{|\mathbf{E}\times\mathbf{B}|}\,, \tag{1.4}$$

where Ω_α is the particle gyro frequency given by $\Omega_\alpha = \frac{q_\alpha B}{m_\alpha}$ and $V_0 = E/B$ is the collisionless plasma speed of motion in crossed electric and magnetic fields, which can be derived from Equation 1.3 assuming no collisions.

In Equation 1.4, the first term on the right describes particle fluid motion along the direction of the electric field, and the second term describes particle motion along the $\mathbf{E}\times\mathbf{B}$ direction, both in a plane perpendicular to the magnetic field. In the F-region $\nu_{\alpha n} << \Omega_\alpha$ and the first term in Equation 1.4 is small and can be neglected, while for the second term, the coefficient $\frac{\Omega_\alpha^2}{(\Omega_\alpha^2 + \nu_{\alpha n}^2)}$ can be approximated as 1, so that Equation 1.4 reduces to

$$\mathbf{V}_{0e} = \mathbf{V}_{0i} = V_0 \frac{\mathbf{E}\times\mathbf{B}}{|\mathbf{E}\times\mathbf{B}|}. \tag{1.5}$$

Equation 1.5, applicable to a collisionless plasma, implies that both electrons and ions move with the same velocity along the $\mathbf{E}\times\mathbf{B}$ direction. This process is often referred to as plasma convection.

There are nonzero particle fluid velocities along the electric field as well, although they are small. The ion velocity is more significant and can be described by the equation

$$\mathbf{V}_{0i} = \frac{\nu_{in}}{\Omega_i} V_0 \frac{\mathbf{E}}{|\mathbf{E}|}. \tag{1.6}$$

For the bottom side of the F region, $\nu_{in}/\Omega_i \approx 10^{-2}$ which implies that there is a relative drift between electrons and ions ~$0.01 V_0$ along the direction of the electric field. This drift is called the Pedersen drift. Its existence is essential for the generation of small-scale irregularities that we discuss in the following section.

For the bottom of the E region the expression for the fluid velocity of electrons is the same but for ions it changes because at these heights $\nu_{in}/\Omega_i >> 1$. The velocity of ions can be expressed (from Equation 1.4) as

$$\mathbf{V}_{0i} = \frac{\Omega_i}{\nu_{in}} V_0 \frac{\mathbf{E}}{|\mathbf{E}|}. \tag{1.7}$$

An important conclusion from this equation is that electrons and ions do not move with the same velocity in the E region. Instead, there is a significant relative drift in the $\mathbf{E}\times\mathbf{B}$ direction, called the Hall drift. The velocity of ions is ~$0.1 V_0$ (from Equation 1.7), and it is along the direction of the E field (Equation 1.7). The Hall drift vector is oriented precisely along the $\mathbf{E}\times\mathbf{B}$ direction, and its magnitude is equal to $\left|\frac{E}{B}\right|$. The presence of a strong relative drift between the electrons and ions coupled with significant electron density in the E region leads to excitation of a strong current detectable with magnetometers, instruments sensitive to changes of the geomagnetic field. We mention that the Pedersen drift still exists at these heights, but it is of secondary importance.

The existence of relative drift between electrons and ions in the ionosphere can lead to the development of plasma instabilities. The result of these instabilities is the creation of microstructures of the electron density in the ionosphere, ionospheric irregularities, capable of scattering radio waves.

1.4.3 Gradient drift plasma instability as a source of ionospheric irregularities

Plasmas can support some wave motions, for example, electrostatic waves at the plasma frequency. These oscillations would generally die because of diffusive damping. However, in the presence of sources of free energy, and in a case of a possibility of this energy to be transferred to waves, the spontaneous weak waves can grow and lead to the so-called plasma instability. The unstable waves would grow to some amplitude, and thus electron density waves/irregularities would be excited in the plasma. It is important to know the growth rate and threshold for a plasma instability as this indicates conditions for which ionospheric irregularities would occur, and various systems, such as coherent radars, can be used for their detection and investigation. It is also crucial to know the velocity of plasma waves as scatter from them would give information on the electric field, and therefore one can remotely diagnose the plasma conditions in the ionosphere.
The Gradient-Drift (GD) plasma instability is essential for the irregularities of interest in this thesis.

To explain how the GD instability emerges, let us consider an F region plasma configuration as shown in Figure 1.6. We assume that there is a downward directed magnetic field, an electric field in the *x*-direction and plasma density gradient in the *y*-direction. Let us consider blob-like perturbations in the electron density established in the ionosphere. The dark shading indicates a density enhancement in the perturbation, and the light shading suggests a density depletion. As these blobs are set, the polarisation electric fields $\delta\mathbf{E}$ will be established inside the blobs as shown in Figure 1.6. This happens because the ions move along the direction of the electric field with Pedersen speed of V_{0i} and the electrons have almost no Pedersen drift speed. As a result, charges would build up on blob edges as shown in Figure 1.6. Because plasma (electrons and ions) are moving in the $\mathbf{E}\times\mathbf{B}$ direction at the F region heights, blobs with enhanced (depleted) plasma would $\delta\mathbf{E}\times\mathbf{B}$ drift in the negative (positive) *y*-direction. This means that, if there is a plasma density gradient in the *y*-direction as shown, then the blobs with enhanced

(depleted) density move to the low (high) density regions, implying wave amplitude increase (instability) of the density perturbation.

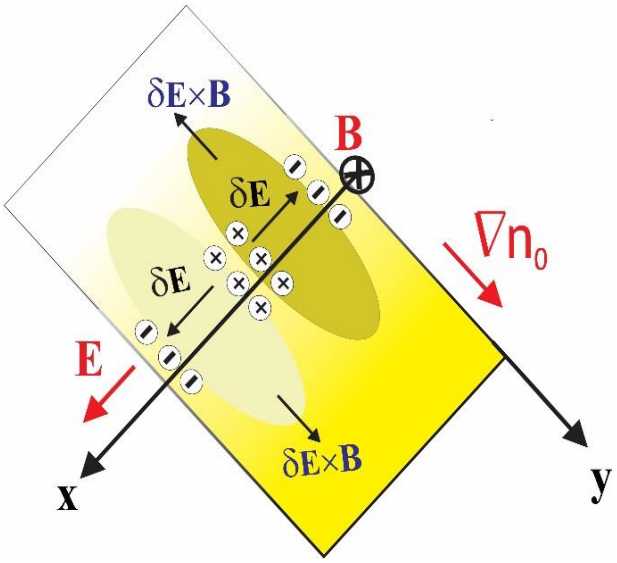

Figure 1.6: Ionospheric configuration for the gradient drift instability in the F region. Dark and light shading indicates density enhancement and density depletion respectively. Adapted from Liu [2010].

To describe the instability quantitatively, we consider one Fourier component of the perturbation blob with wave vector **k** and frequency ω. We also consider a more general case where **k** is directed away from the *x*-axis. The frequency and growth rate of the sinusoidal perturbation can be determined as follows. First, one must consider the simplified equation of motion, but neglect the effects of particle inertia. Also, one must consider the continuity equation for ions and electrons

$$\frac{\partial n_\alpha}{\partial t} + \nabla \cdot (n_\alpha \mathbf{V}_\alpha) = 0 . \tag{1.8}$$

Linearizing these equations and requiring the non-trivial solution of two equations for two unknowns (usual perturbation in the electrostatic potential and electron density), one obtains the dispersion equation. By assuming $\omega = \omega_r + i\gamma$, where ω_r and γ are the frequency and the growth rate of the perturbation, respectively, one can solve the dispersion equation to obtain

$$\gamma = \frac{V_0}{L}\cos^2\theta - k_\perp^2 D_\perp , \tag{1.9}$$

where $\theta = \cos^{-1}\left(\frac{k_x}{k_\perp}\right)$ is the azimuthal angle of the **k** vector with respect to the *x*-axis, $D_\perp = \left(\frac{\nu_{en}}{\Omega_e \Omega_i}\right) C_s^2$ is the diffusion coefficient, $C_S = \sqrt{\frac{T_e + T_i}{m_i}}$ is the ion-acoustic speed (T_e and T_i are the temperatures of electrons and ions), and *L* describes the scale of the plasma gradient as

$$\frac{1}{L} = \frac{\nabla n}{n}. \tag{1.10}$$

Equation 1.9 implies that a perturbation propagating along the *x*-axis would grow faster than perturbation along any other direction. At large angles θ, the plasma is stable, and no linear wave generation is possible. According to (1.9), the growth rate γ is more significant for larger $|\mathbf{E}\times\mathbf{B}|$ drift and stronger plasma gradient. It is important to note that the GD plasma instability in the F region can directly generate only irregularities with a scale-size of tens of meters (otherwise, the last term in (1.9) is larger than the first term, and the growth rate is negative). The ~10 m irregularities observed by HF radars such as the SuperDARN radars (whose data will be used in this Thesis) are obtained through the non-linear cascading of energy from large to small scales [Tsunoda, 1988]. One should also note that waves of more massive scale (hundreds of meters), corresponding to smaller $|\boldsymbol{k}|$ values, cannot be linearly generated because of recombination effects [Tsunoda, 1988]. The value of $1/\gamma$ gives an estimate of how much time is needed to develop an ionospheric irregularity. For typical auroral F region parameters $D_\perp = 2\ \mathrm{m^2/s}$ [Kelley, 1999, p. 383, Figure 8.19], $E_0 = 10\ \mathrm{mV/m}$, and $L =$ 10 km, one can find that the growing modes with a wavelength of ~100 m have growth time of $\gamma^{-1} \approx 240\ \mathrm{s}$.

1.4.4 Farley-Buneman instability as a source of ionospheric irregularities

Farley Buneman (FB) plasma instability occurs in homogeneous plasmas when the relative drift between the electrons and ions exceeds the ion-acoustic speed of the medium. Magnetized electrons undergo an $\mathbf{E}\times\mathbf{B}$ drift and stream through stationary ions which are unmagnetized due to a large collision frequency with neutrals. This instability is most effective at meter-scale wavelengths, and it is believed that the FB instability is the cause for the onset of Type 1 coherent

echoes. Analysis of the FB instability is like that of the GD instability described above and therefore will not be reviewed here. The wave frequency (ω_r) and growth rate (γ) of the FB instability as given by Kelley [2009] are then

$$\omega_r = \frac{\mathbf{k} \cdot \mathbf{V}_{0e}}{1+\psi} \tag{1.11}$$

and

$$\gamma = \frac{\psi_0}{\nu_i(1+\psi_0)}\left[\omega_r^2 - k^2 C_s^2\right], \tag{1.12}$$

where $\mathbf{V}_{0e}$ is the velocity of the electron drift as defined in Equation 1.5 and $\psi_0 = \frac{\nu_e \nu_i}{\Omega_e \Omega_i}\left(1+\frac{\Omega_e^2}{\nu_e^2}\sin^2\alpha_o\right)$ is a parameter that depends on the collision frequencies, gyro-frequencies and the aspect angle α_o, the angle between the wave propagation direction and the perpendicular to the magnetic field. This instability requires an enhanced electric field of > 20 mV/m. These are typical values for high latitudes.

Although Equation (1.11) implies that the velocity of irregularities ($V_{phase} = \omega / k$) produced by the FB plasma instability is proportional to the electric field magnitude (because $\mathbf{V}_{0e}$ is proportional to the E field) a number of nonlinear theories suggest that, in the final state, the irregularity velocity will be close to the ion-acoustic speed of the medium C_s. This purely theoretical notion is consistent with numerous radar observations of such irregularities, termed the Type 1 irregularities, at VHF and their occasional detection at HF (e.g., Fejer and Kelley [1980]; Schlegel [1996]; Gorin et al. [2012]).

Small-scale irregularities in the Earth's ionosphere, whose mechanism of generation has just been discussed above, can be viewed as minor "ripples" in the main body of the ionosphere. Using radars, these irregularities can scatter radio waves in the range of 10-1000 MHz. This gives an opportunity to measure the drift of the plasma as well as plasma density with ground-based radars, which are the instruments used in this thesis.

1.5 Global-scale plasma flow patterns at high latitudes and in the polar cap

At high latitudes, plasma motion in the ionosphere is predominantly driven by the electric field established due to the interaction between the IMF and the Earth's magnetosphere, as explained in Section 1.2. This electric field is continuously mapped down from the magnetosphere to the ionosphere, and as a result, magnetospheric processes are being replicated in the ionosphere. For this reason, plasma patterns at the ionospheric level have been studied for many years by using various techniques, and more recently, by computational methods.

Empirical statistical convection models have been developed from various instruments such as drift on meters satellites [Hairston and Heelis, 1990; Rich and Hairston, 1994; Weimer, 1995], magnetometers [Papitashvili et al., 1994], and indeed with the SuperDARN radars [Ruohoniemi and Greenwald, 1996, 2005; Cousins and Shepherd, 2010] to establish standard ionospheric convection patterns based on the magnitude and polarity of the IMF. While clearly defined ionospheric plasma configurations have been established for periods with the IMF in a quasi-steady state, especially pointing southward, the pattern configurations for the northward IMF are still not well documented.

1.5.1 Case of southward IMF ($\mathbf{B_z^-}$)

When the IMF is southward-oriented $(B_z < 0)$, the Dungey reconnection process occurs (see Section 1.3) resulting in the high-latitude ionospheric convection pattern with a two-cell geometry: antisunward plasma flow across the near Pole region and sunward plasma flow at the lower latitudes, both on the dawn and dusk sides (Figure 1.7a). This pattern is associated with a dawn-dusk electric field within the plasma sheet. These two high-latitude cells show a dependence on the IMF y-component (Figures 1.7b and 1.7c). In the northern hemisphere, non-zero B_y leads to domination of the clockwise circulating dusk cell when B_y is positive (Figure 1.7b), while the dawn cell dominates when B_y is negative (Figure 1.7c). When the IMF B_y component is small (close to 0), the convection cells are roughly symmetric, but interestingly enough, the flow is aligned along the 23-11 magnetic longitude (MLT) line. It is said that the region of stagnant flow,

the so-called "throat," is shifted toward prenoon hours. Such a shift is stronger for increasing IMF $B_y > 0$, and the throat is often shifted toward afternoon hours for strong IMF $B_y < 0$.

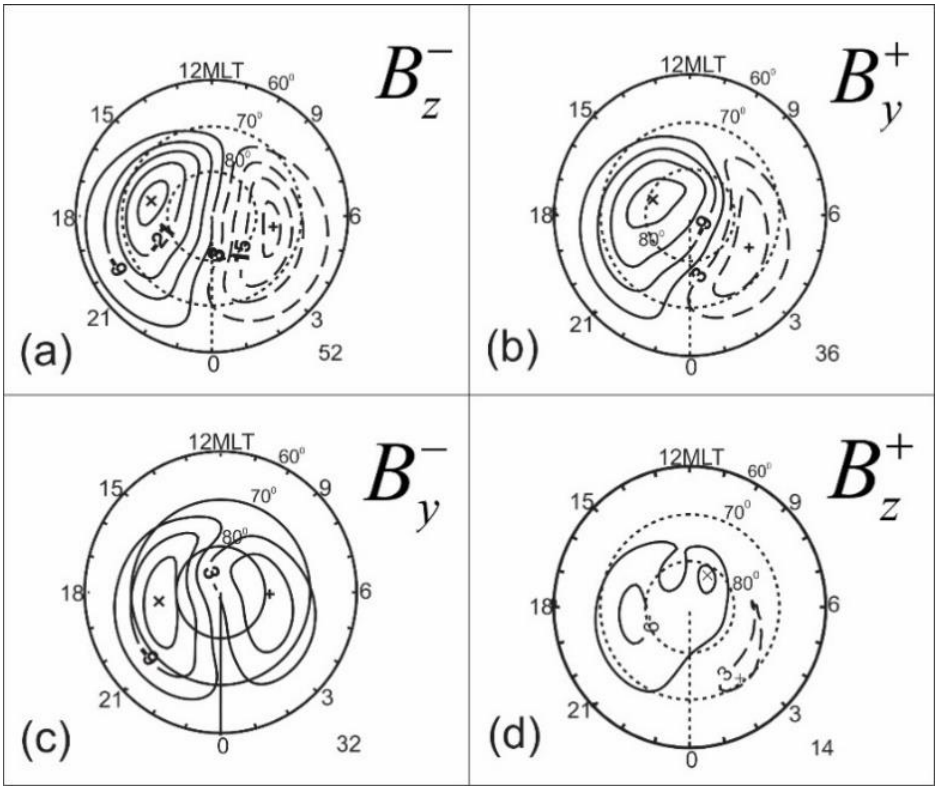

Figure 1.7: Schematic representation of high-latitude convection patterns and their dependence on IMF B_z and B_y. Shown in each plot are voltage contours in kV. The number in the left bottom corner is the potential difference between the maximum and minimum of the potential. Adapted from Ruohoniemi and Greenwald [2005].

1.5.2 Case of northward IMF ($\mathbf{B_z^+}$)

When the IMF is oriented northward, the convection pattern becomes complicated and often consists of a number of cells. It is believed that the 4-cell convection pattern dominates, although 3 cells are also frequent (e.g., Watanabe and Sofko [2009]). Figure 1.7d gives an example of the convection pattern under strongly dominant IMF B_z^+ conditions. Here the weak viscous cell is evident at dawn hours. The large dusk side cell is a superposition of the clockwise circulating viscous cell and two reverse convection cells on the dayside. The reverse cells are not seen as a separate entity, but the flow is sunward at the noon meridian where they dominate.

As is the case for southward IMF, the shape of the convection pattern for northward IMF shows a dependence on the magnitude of IMF B_z and the polarity of the IMF B_y (e.g., Reiff and Burch [1985]). When B_y is positive, the inner/reverse morning cell dominates, and when B_y is negative, the inner/reverse dusk cell becomes more significant. In a situation where B_z is only weakly dominant, the inner cells merge into one large cell with eastward flowing plasma for $B_y < 0$ and westward flowing plasma for $B_y > 0$.

1.6 Objectives of the undertaken research

The main goal of this thesis is to gain knowledge on the plasma flow patterns and their relationship with external drivers in the polar cap by involving data from the PolarDARN/SuperDARN radars, and Resolute Bay incoherent scatter radar (RISR). The primary focus is on the Clyde River PolarDARN radar. It is a special one in the family of SuperDARN radars as its field of view is oriented roughly along magnetic parallels. Only two other high-latitude SuperDARN radars have similar geometry – at Longyearbyen in Northern Europe and at South Pole in Antarctica. Both of these radars, however, monitor echoes at lower magnetic latitudes (MLAT) in close vicinity to the auroral zone. Also, these radars started operation very recently, and their datasets are limited. In fact, no data from Longyearbyen were available at the beginning of this Thesis project.

Information on plasma flows at high latitudes is crucial for many applications. For example, the AMIE (Assimilative Mapping of the Ionospheric Electrodynamics) electrodynamic model [Richmond and Kamide, 1988; Richmond, 1992] digests data from numerous data sources (including SuperDARN) to predict global-scale distributions of many fundamental electrodynamical parameters of the high-latitude ionosphere: for example, horizontal and vertical (field-aligned) currents and overall electrical energy input into the Earth's ionosphere from the Sun.

Continuous monitoring of plasma flows in the high-latitude ionosphere is a daunting task, firstly, because global coverage is required and, secondly, because the timescale of flow variations is on the order of one minute. These limitations are significantly alleviated by the SuperDARN radars as will be discussed in Chapter 2. However, these radars have some weaknesses in the way they measure the patterns, as also will be discussed in Chapter 2. Incoherent scatter radars provide

continuous data, but in localized areas [Bahcivan et al., 2010, 2013]; they also have limitations especially when no crossed beams are used.

For practical applications and modeling/predictions of the near Earth's plasma parameters, an important question is whether various systems monitoring plasma flows produce compatible data. The concerns are not so much with respect to their methods as conceived, but mostly related to differences caused by different spatial and temporal resolutions of the systems and specifics of their operation modes. Despite the great importance of this question, inter-comparison between various systems monitoring plasma flows remains very limited.

The first objective *of this thesis is to validate the Clyde River PolarDARN/SuperDARN radar measurements of the plasma flow by comparing the measured Doppler velocity of F region echoes with the convection data provided by the incoherent scatter radar RISR-C in the overlapping observation areas. We also investigate the differences between 2-D convection vectors produced by the SuperDARN network as a whole and by the RISR-C radar alone.*

It is important to realize that the CLY radar velocity data have never been tested against any other instrument contrary to the other two PolarDARN radars at Rankin Inlet and Inuvik [Koustov et al., 2009; Mori et al., 2012; Bahcivan et al., 2013; Koustov et al., 2016; Gillies et al., 2018]. Data from this radar, however, were used for validation work for the Swarm satellite measurements of plasma drifts [Koustov et al., 2017].

Besides the general necessity to validate the CLY radar velocity measurements, there are ongoing concerns about the quality of velocity measurements with SuperDARN radars. One unresolved issue is low velocities observed at all ranges [Gillies et al., 2018]. The work to be undertaken can lead to a better understanding of how coherent echoes detected by SuperDARN are formed. One example of this kind of work is the recent revelation that HF coherent radars are very likely sensitive to plasma blobs within the large scattering volume, and this affects the velocity of observed echoes (e.g., Koustov et al. [2016]).

The second objective *of this thesis is revealing and assessing some potential reasons for the differences between PolarDARN-based plasma drifts and the convection vectors inferred from the incoherent scatter radar RISR-C measurements.*

Besides assessment of the two radar system products, the plan is to investigate self-consistency between measurements of two HF radars when they measure the Doppler velocity in about the same directions. This is possible to do with the CLY radar because one of its beams is

looking in about the same direction (with an azimuthal difference of ~180°) as the SuperDARN radar at Kodiak.

After performing these velocity comparisons and making certain that the CLY radar works consistently with other radars of the network, data gathered by this radar over the years will be considered to gain knowledge on the plasma flows in the central polar cap. Although the plasma flow patterns are under investigation for decades, many issues remain unsettled. One is seasonal and solar cycle variations of the flow intensity. Since conductance of the ionosphere changes dramatically with season, one would expect a strong seasonal variation of the flow intensity. Strangely enough, the SuperDARN-based statistical models do not show significant seasonal change [Ruohoniemi and Greenwald, 2005]. Koustov et al. [2015] attempted to address this question by averaging 2-D vectors over monthly portions of data. They revealed some peculiar features in diurnal and seasonal variations of the flow intensity that explained the occurrence of meter-scale irregularities detectable by VHF coherent radars.

The third objective *of this thesis is to study plasma convection pattern features in the polar cap ionosphere by using multi-year datasets available for the Clyde River PolarDARN radar*. Research was focused on the zonal component of the plasma flows at magnetic latitudes around $80°$. More specific targets of the investigation were diurnal, seasonal and annual variations of the zonal flow velocity. The investigation started by considering the entire database without considering conditions in the solar wind. Then the data was sorted according to the IMF B_z sign and according to the IMF B_y sign. Although these targets have been covered by many statistical models (e.g., Heppner and Maynard [1987]; Rich and Hairston [1994]), including recently developed statistical model of plasma flows by Cousins and Shepherd [2010; 2012], our focus was on finer features that were very likely smoothed out during the model development.

Thesis outline

The thesis is organized as follows. Chapter 2 describes the principle of operation of the two major instruments involved in this work: the coherent HF SuperDARN radars and the incoherent scatter radar RISR-C. Chapter 3 presents a comparison of HF radar velocities and $\mathbf{E}\times\mathbf{B}$ plasma drifts as measured by the incoherent scatter radar RISR-C. Velocity measurements of the CLY and Inuvik SuperDARN HF radars (looking toward each other) are considered in Chapter 4. After validating

the Clyde River PolarDARN velocity measurements in Chapters 3 and 4, Chapter 5 investigates the high-latitude convection pattern change with season through the analysis of Clyde River radar velocities. Finally, the results obtained in this thesis are summarized in Chapter 6, where suggestions for future research are also outlined.

CHAPTER 2

INSTRUMENTS AND DATA PROCESSING TECHNIQUES

This project considers data from multiple instruments. Two major ones were the Super Dual Auroral Radar Network (Super DARN) high-frequency (HF) radars and the Resolute Bay Incoherent Scatter Radar - Canada (RISR-C).

2.1 The Super Dual Auroral Radar Network

The Super Dual Auroral Radar Network (SuperDARN) is a network of coherent HF radars installed around the northern and southern polar regions to continuously monitor the $\mathbf{E}\times\mathbf{B}$ plasma drift in the Earth's ionosphere [Greenwald et al., 1995]. These radars measure the Doppler velocity of coherent echoes arising from radar waves (transmitted obliquely into the ionosphere) scattering off ionospheric structures such as field-aligned plasma irregularities in the E and F regions. Regarding the location and viewing zone, we categorize the radars into three groups: mid-latitude, auroral zone, and polar cap radars. These radars are synchronized and use the same principle of operation. There are currently 36 radars in operation combined to cover large regions of both the northern and southern hemisphere ionospheres as presented by the radars fields-of-view (FoVs) in Figure 2.1. Many SuperDARN radar fields-of-view overlap as they are arranged in pairs. The choice of pair arrangement comes from the original idea of the experiment which was to determine the actual direction that a target is moving by combining a pair of independent line-of-sight (l-o-s) velocities to form a 2-D vector velocity of the target. Later on, this idea was abandoned because the number of common points was not significant. Instead, a new technique, based purely on individual l-o-s data, was introduced to produce global-scale plasma convection maps. Three of the radars, at Inuvik (INV), Rankin Inlet (RKN) and Clyde River (CLY), referred to as the Polar Dual Auroral Radar Network (PolarDARN), produced the data that we used in this study.

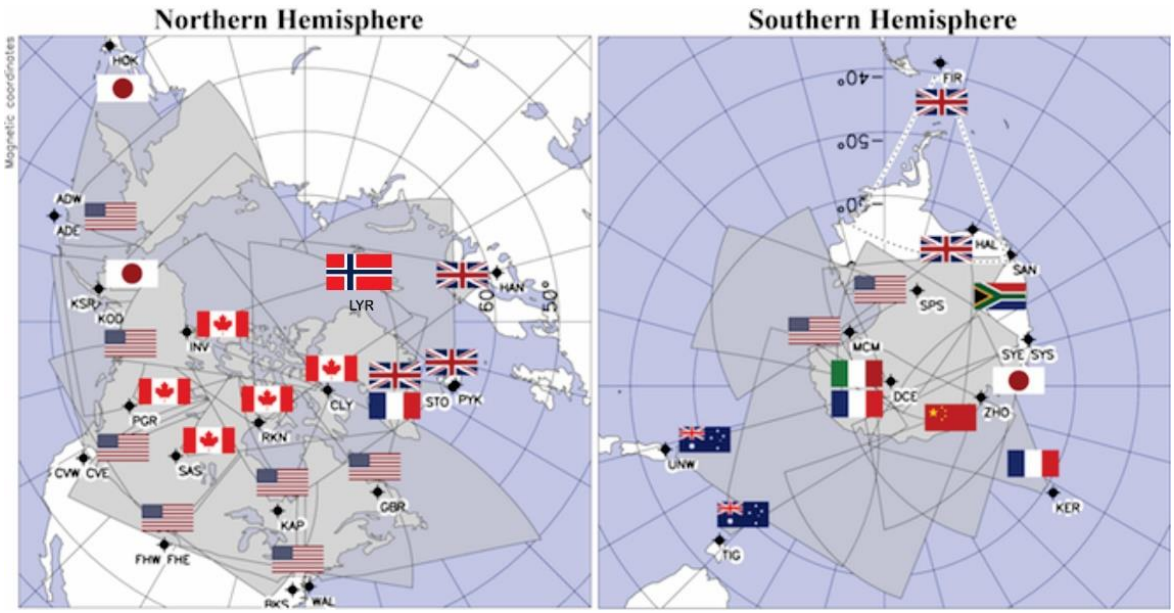

Figure 2.1: Fields of view of the SuperDARN radars in the Northern Hemisphere and Southern Hemisphere. From https://superdarn.ca/superDARN (last access: May 2018).

The plasma irregularities that SuperDARN detects are plasma waves excited when electron density gradients are present, commonly attributed to the gradient-drift (GD) instability. The GD instability is driven by the background electric field and becomes active when plasma moves in the direction of the background plasma density gradient as described in Section 1.4.2. These irregularities are highly aligned with the geomagnetic field. The radars are able to detect echoes from such irregularities, provided the transmitted radio waves propagate perpendicular to the wavefronts of the irregularities, and thus perpendicular to the geomagnetic field. This geometry is made possible by choosing radio wave frequencies that allow ionospheric refraction to be significant enough to turn the radio waves towards being normal to the geomagnetic field. The radars operate at HF frequencies in the range of 8-20 MHz, with a peak transmitted power of 10 kW.

Each SuperDARN radar transmits a fixed sequence of seven 300 μs wave pulses along one of its sixteen beam directions. A beam direction is achieved by using a phasing network to delay the transmission to the 16 transmitters. Typically, there are about 30 pulse sequences averaged for each beam position before moving on to the next beam direction, $3.24°$ away. In total, the 16 beam directions cover an azimuthal range of $52°$. A full scan through all 16 beam directions is done in a 1-minute interval. Figure 2.2 shows the current pulse sequence used. The numbers in the diagram

(0, 9, 12, 20, 22, 26, 27) are multiples of the pulse lag time of τ (currently 2.4 ms). The length of each pulse is fixed at 0.3 ms, providing a range gate of length 45 km assuming that the pulse travels at the vacuum speed of light *c* (3.00×10^8 m/s). Typically, a total of 75 range gates are sampled for each beam position, with the first gate selected at 180 km from the radar site, and the last gate at 3555 km, giving a total range span of 3375 km. The backscattered signals returned from the pulse sequence are then processed to produce the autocorrelation functions (ACFs), as a function of the lag delays between pulses, for all range gates [Villain et al., 1987].

Figure 2.2: SuperDARN normal 7-pulse scheme.

2.1.1 Autocorrelation function (ACF) analysis

The SuperDARN radars provide information on the backscattered power, mean Doppler velocity and spectral width in each range cell, achieved through the use of complex autocorrelation functions (ACFs). The effectiveness of the ACF method can be illustrated using a two-pulse sequence with the pulse lag time τ, as shown in Figure 2.3. Scattering occurs at three different distances (or ranges), namely d_-, d_0 and d_+. This scenario is the simplest case of a multipulse transmission technique with backscattering from different distances.

At time $t = t_0$, the first pulse (p_1) is transmitted, followed by the second pulse (p_2) transmitted at time $t_0 + \tau$. Pulse p_1 is scattered from a distance d_0 and returns with an amplitude $A_1(d_0)$ at time $t_1 = t_0 + 2d_0 / c$. The time t_1, however, is also the time pulse p_2 returns with amplitude $A_2(d_-)$ from a distance d_-. The total amplitude $A(t_1)$ at t_1 is [Baker, 2003]

$$A(t_1) = A_1(d_0) + A_2(d_-). \tag{2.1}$$

On the other hand, at time $t_1 + \tau$, p_2 returns from d_0 with amplitude $A_2(d_0)$, and p_1 from a distance d_+ as $A_1(d_+)$ resulting in a total amplitude $A(t_1 + \tau)$

$$A(t_1 + \tau) = A_1(d_+) + A_2(d_0). \tag{2.2}$$

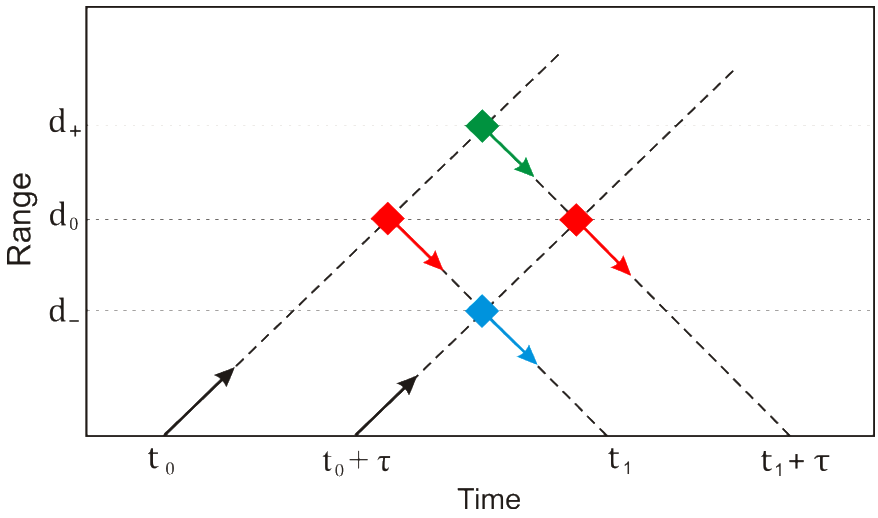

Figure 2.3: Range-time diagram for the 2-pulse sequence.

The contribution to the ACF at lag τ is thus $A_1(t_1)\cdot A(t_1+\tau)$. The ACF contains four terms; this causes uncertainty and is resolved by transmitting the pulse sequence multiple times, thereby reducing the uncorrelated signals. By taking the average in time of these many double pulses, Equations 2.1 and 2.2 give

$$\langle A_1(t_1)\cdot A(t_1+\tau)\rangle = \langle A_1(d_0)\cdot A_2(d_0)\rangle + \langle A_1(d_0)\cdot A_1(d_+)\rangle + \langle A_2(d_0)\cdot A_2(d_-)\rangle + \langle A_1(d_+)\cdot A_2(d_-)\rangle. \quad (2.3)$$

Because the last three terms of Equation 2.3 are contributions from uncorrelated signals received from different distances, they will go to zero in the mean, thus reducing Equation 2.3 to

$$\langle A_1(t_1)\cdot A(t_1+\tau)\rangle \approx \langle A_1(d_0)\cdot A_2(d_0)\rangle. \quad (2.4)$$

The ACF can also be written regarding its amplitude A_m and phase ϕ as follows

$$\langle A_1(t_1)\cdot A(t_1+\tau)\rangle \approx A_m e^{i\phi}. \quad (2.5)$$

Equation 2.4 contains power only from the desired height d_0, with lag τ. The two-pulse technique yields an ACF only at lag τ. In the case of a multi-pulse sequence of many pulses separated by

different integer values of τ, the ACF can be evaluated at a sufficient number of lags to produce a good power spectrum from the Fourier transform (FFT) or from other spectral techniques. The ACF has both real and imaginary parts, coming from the in-phase and quadrature (phase shifted by $\pi/2$) components of each return signal. The phase of the ACF is determined by comparing the real and imaginary components (Figure 2.4c)

$$\phi = \tan^{-1}\left(\frac{Im(ACF)}{Re(ACF)}\right). \tag{2.6}$$

The SuperDARN radars transmit multiple-pulse sequence with different values of τ (Figure 2.2) because the measurement of phase in this way is more accurate compared to a two-pulse sequence. Furthermore, it is impossible to determine the spectral width of the backscattered signal by transmitting a 2-pulse sequence.

2.1.2 Doppler shift measurements and computing the Line-of-Sight velocity

The Line-of-Sight (l-o-s) velocity (i.e., the component of the plasma drift along a radar beam) of an irregularity can be determined from the Doppler shift of the backscatter. Figure 2.4a shows the real and imaginary components of a good ACF, having the shape of a decaying sinusoid, with the real and imaginary components plotted against lag. The l-o-s velocity is determined from the slope (rate of change) of the phase angle ϕ of the ACF [villain et al., 1987]. The phase angle is assumed to be $\phi =< \omega_D > k_T$ (where the lag number is k_T). The phase has a linear relationship with lag, the slope of which is the mean Doppler frequency of the echo (Figure 2.4c). The relationship between the Doppler frequency and the Doppler velocity (velocity of irregularity) is given as

$$v_{irr} = \frac{\omega_D c}{4\pi f_T}, \tag{2.7}$$

where c is the speed of light. To derive Equation 2.7, it is important to take into account two shifts in the frequency of the radio wave due to the Doppler effect. If f_T is the frequency transmitted by the radar, the radio wave frequency received by the radar is $f_R \approx f_T(1+2v_{irr}/c)$, where v_{irr} is the velocity of the irregularity, then the frequency captured by a moving irregularity would be

$$f_I = f_T(1+v_{irr}/c) \tag{2.8}$$

due to Doppler effect. When the signal is returning, there is another Doppler shift (since the irregularity is moving with respect to the radar), which leads to the radar-measured frequency of

$$f_R = f_I(1+v_{irr}/c). \tag{2.9}$$

Substituting for f_I in Equation 2.9 by using Equation 2.8, we obtain

$$f_R = f_T\left(1+2\frac{v_{irr}}{c}\right), \tag{2.10}$$

$$f_D = f_R - f_T = 2f_T\left(\frac{v_{irr}}{c}\right). \tag{2.11}$$

Given the mean Doppler shift angular frequency (and using $\omega_D = 2\pi f_D$), the irregularity velocity is determined by

$$v_{irr} = \frac{c}{2}\left(\frac{f_D}{f_T}\right) = \frac{c}{2}\left(\frac{\omega_D}{2\pi f_T}\right) = \frac{\omega_D c}{4\pi f_T}. \tag{2.12}$$

Equation 2.7 accounts for both directions of radar wave motions, toward and away from the radar. In this equation, positive velocities correspond to flows toward and negative velocities to flows away from the radar.

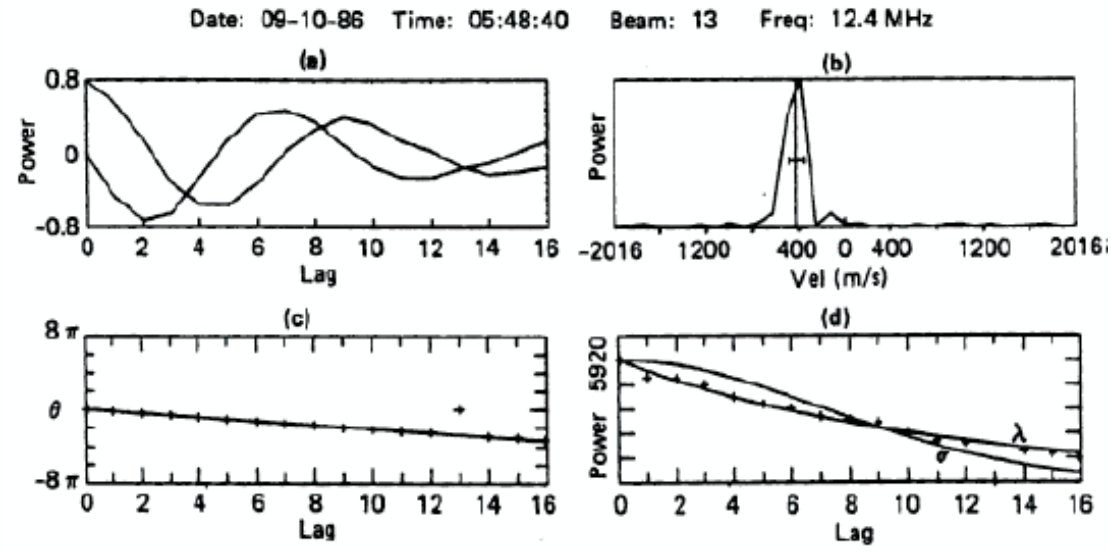

Figure 2.4: An example of the radar signal processing techniques. (a) Real and imaginary parts of the ACF. (b) Doppler spectrum obtained through FFT of the ACF. (c) Phase angle as a function of lag and its linear squares fit. (d) Power variation of the ACF as a function of lag with exponential (λ) and Gaussian (σ) least squares fit. From Villain et al. [1987].

2.1.3 Spectral power and width determination

Figure 2.4a shows that the imaginary part of the ACF is maximized at lag number zero. Also noticeable is the decay of the ACF as lag number increases. The ACF decays because signals become less correlated as the time lag between them increases. One possible way to determine the backscattered power (p_0) is to consider the measured amplitude at this lag number zero (i.e., where the Imaginary part of the ACF is zero) [Baker, 2003]. Alternatively, the Lorentzian or Gaussian least-square fits of the ACF (Figure 2.4d) can also be used to find the backscattered power. The Lorentzian FITACF is given by a Lorentzian function with the decay constant l as follows

$$p_l(\tau) = p_0 \exp(-l\tau), \tag{2.13}$$

where p_0 defines the maximum Lorentzian backscattered power. The Gaussian FITACF meanwhile is given by a Gaussian function with the decay constant g as follows

$$p_g(\tau) = p_0 \exp(-g^2\tau^2), \tag{2.14}$$

where p_0 defines the maximum Gaussian backscattered power.

The spectral width of the backscattered signal can be obtained by using the Wiener-Khinchin theorem [Wiener, 1964]. The theorem implies that the Fourier transform of the ACF yields the power spectrum of the backscattered signal in terms of the velocity. Then the full width at the maximum half power specifies the spectral width of the backscattered signal. In the case of the Lorentzian FITACF (Equation 2.13), the Lorentzian spectral width (W_l) obtained from the Wiener-Khinchin theorem can be written as

$$W_l = \frac{cl}{2\pi f_T}. \tag{2.15}$$

For the Gaussian FITACF (Equation 2.14), the Gaussian spectral width (W_g) is given by

$$W_g = \frac{cg\sqrt{ln2}}{\pi f_T}. \tag{2.16}$$

Figure 2.3b shows an example of the Fourier transform of the ACF with spectral width (horizontal line) and velocity (vertical line) where the Lorentzian least-square fit is considered. Villain et al. [1996] showed experimentally that the Lorentzian and Gaussian functions are suitable for representing the ACF from the F region and E region respectively.

2.1.4 Interferometry technique to measure the angle of elevation

The angle of arrival of the returned signal, when measured with respect to the ground, is known as the elevation angle. Ponomarenko et al. [2011] showed how the critical plasma frequency of the F layer and subsequently the background electron density of the F region could be determined by measuring the elevation angle of backscatter. The SuperDARN radars are comprised of 16 main antennas and an additional 4 antennas behind the main array as a secondary (interferometer) array. The latter is used to calculate the elevation angle of the arriving signal [Andre et al., 1998]. Figure 2.5 illustrates the fundamental principle for determining the elevation angle.

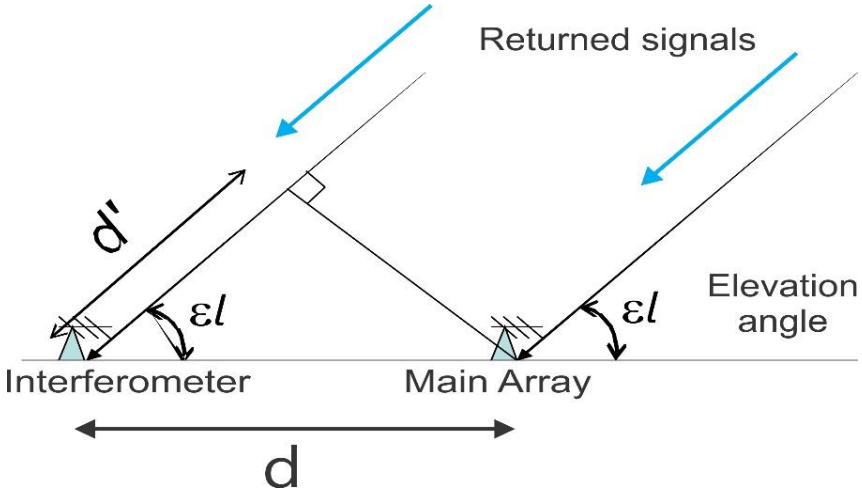

Figure 2.5: The geometry of the interferometry technique to measure the elevation angle.

At the elevation angle εl, the path length difference between backscattered signals received by the main and interferometer arrays is $d' = d\cos(\varepsilon l)$, where $d \sim 100\,\mathrm{m}$ is the distance between the

two arrays. Given the phase shift due to this path length difference is $\Delta\varphi = (2\pi/\lambda)d'$, the elevation angle εl can be expressed as

$$\varepsilon l = \cos^{-1}\left(\frac{\lambda}{2\pi d}\Delta\varphi\right). \tag{2.17}$$

The phase shift is determined by calculating the time difference between backscattered signals received by the main and interferometer arrays.

2.1.5 SuperDARN merge technique

When the SuperDARN radars were first designed, they were arranged strategically such that pairs of radars would have overlapping fields-of-view. The primary objective of this was to combine line-of-sight measurements from both radars to get 2-D velocity vectors on a global scale. As shown in Figure 2.6, the l-o-s velocities from each radar beam are cosine components of the full vector and are expressed as

$$v_1 = \mathbf{v_M}\cos\theta_1, \tag{2.18a}$$

$$v_2 = \mathbf{v_M}\cos\theta_2, \tag{2.18b}$$

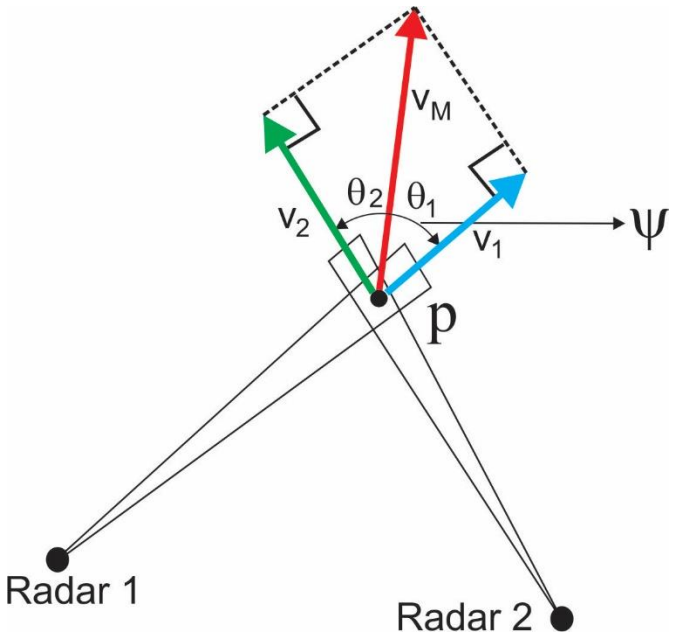

Figure 2.6: A scheme illustrating the SuperDARN merge technique.

where $\mathbf{v_M}$ is the merged velocity magnitude equal to the $\mathbf{E}\times\mathbf{B}$ drift, θ_1 and θ_2 are the angles between each radar beam and the merged velocity direction, while v_1 and v_2 are the l-o-s velocities measured by each radar. To fully determine $\mathbf{v_M}$ at a given point P, one only needs the magnitude and one of the angles, say θ_1, which will tell us the direction of the $\mathbf{E}\times\mathbf{B}$ drift relative to the radar beam direction. Since both angles are unknown, one more piece of information is required to find the full velocity vector. This last piece is found by observing that the sum of the two angles θ_1 and θ_2 is equal to the angle ψ formed between the radar beams. This angle is a fixed value and is calculated by finding the difference in the bearings from point P to each radar site by using the coordinates of all 3 locations. Solving for $\mathbf{v_M}$ and θ_1 gives [Mori, 2011]

$$\theta_1 = \arctan\left(\frac{v_2 - v_1\cos\psi}{v_1\sin\psi}\right), \text{ and} \tag{2.19}$$

$$\mathbf{v_M} = \frac{v_1}{\cos\theta_1}. \tag{2.20}$$

SuperDARN observations over its first several years of operation showed that only a small number of merged vectors is generated because one of the radars often does not have echoes while the other does. The amount of l-o-s data available is nevertheless significant. Due to this limitation, more advanced techniques for making 2-D vectors at points beyond the points where merged data are available, have been developed.

2.1.6 SuperDARN FIT technique

The primary objective of the SuperDARN community is the production of global-scale maps of the electric field (or equivalently plasma circulation) in the ionosphere with a temporal resolution of about a minute. The technique used for this map generation is known as the Potential FIT technique [Ruohoniemi and Baker, 1998]. In this approach, the l-o-s velocity data from all available radars (in each hemisphere separately) are used to generate the global-scale convection map for each radar scan (1- or 2-minute intervals) or multiple scans. The results are usually presented in the form of lines of equal potential, including potential maxima and minima so that a crucial parameter, the cross polar cap potential (CPCP), can be estimated directly.

The Potential FIT technique has several steps. The ground scatter, as well as l-o-s data with error estimates greater than 200 m/s, are excluded from the analysis. Median filtering is then applied to each l-o-s measurements at time t_i and location $(b,g)_i$ in the radar beam/gate coordinates. Weighted medians are computed for all the measurements in the 3×3 region of beam/gate cells centered at $(b,g)_i$ for three consecutive scans centered at t_i. If the number of velocity values in the weighted dataset is sufficiently large, the median value of the dataset is assigned to $(b,g)_i$. Otherwise, no value is assigned for the cell $(b,g)_i$ at the time t_i.

Once spatiotemporal filtering is complete, the filtered data are placed in a grid with cells of equal area to avoid oversampling of data near the radar. The grid cells are separated by $1°$ width in latitudinal dimension, corresponding to ~ 111 km, and in the longitudinal dimension by ~111 km. For each grid cell, the average of all filtered velocities is selected if there are greater than 25% of possible measurements in the cell with values. Velocities obtained in this way are called the gridded velocities. The gridded velocities are smoothed out l-o-s velocity values in space and time which are placed on the equidistant grid. Gridded velocities are then used to find the electrostatic potential distribution on the sphere.

The electrostatic potential is a solution of Laplace's equation in spherical coordinates. It is related to the electric field and convection velocity through the equations

$$\mathbf{E} = -\nabla\Phi, \qquad \mathbf{v} = -\frac{\nabla\Phi \times \mathbf{B}}{B^2}. \tag{2.21}$$

The global convection pattern is found using the best fit observed l-o-s velocities v_{los_i}. This procedure is done by minimizing the expression [Ruohoniemi and Baker, 1998]

$$\chi^2 = \sum_{i=1}^{N} \frac{1}{\sigma_i^2}(\mathbf{v_i}\cdot\hat{\mathbf{k}}_\mathbf{i} - v_{los_i})^2, \tag{2.22}$$

where $\mathbf{v_i}$ is the full velocity vector, $\hat{\mathbf{k}}_\mathbf{i}$ is the line-of-sight direction of the radar beam associated with the observed gridded velocity and N is the number of points on the individual map. The expression is weighted using the uncertainty, σ_i. The minimization of χ^2 is done using singular

value decomposition, which then is applied to Equation 2.21 to determine the electric potential everywhere in the polar region.

For the grid cells where there is no l-o-s velocity measurements, values from a statistical model are added as a constraint. In the past, 24 different statistical models were used, covering eight different Interplanetary Magnetic Field (IMF) clock angle conditions and 3 IMF $B_T = \sqrt{B_z^2 + B_y^2}$ magnitude ranges (0-4 nT, 4-6 nT and 6-12 nT), as developed by Ruohoniemi and Greenwald [1996], the RG96 model. Lately, the startup convection model has been replaced by a better quality model by Cousins and Shepherd [2010], CS10. The CS10 model is based on a significantly larger data set, tabulated by finer steps of the solar wind parameters and it encompasses data in the southern hemisphere, contrary to the RG96 model based solely on the Goose Bay radar data. Another constraint is the addition of a Heppner-Maynard boundary (HMB) to the edge of the auroral zone to specify a low latitude convection boundary at magnetic latitude Λ_0.

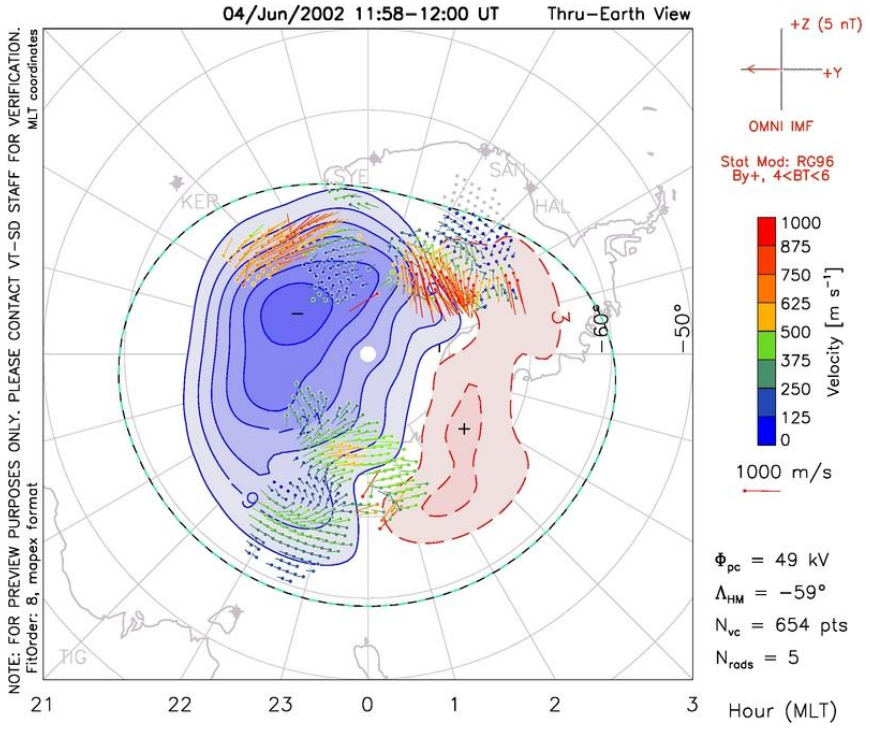

Figure 2.7: SuperDARN convection pattern for 12:00 UT on 04 June 2002. The plot is produced using the FIT technique and the Ruohoniemi and Greenwald 1996 statistical model (RG96 model). From http://vt.superdarn.org (last access: September 2018).

An example of a global-scale plasma convection map obtained with the map potential technique is shown in Figure 2.7. The statistical model used is for $4 < B_T < 6$, B_z^- / B_y^+ (shown in the top right corner). The vectors represent the measured SuperDARN l-o-s velocities, and the green dash line represents the HMB. Blue solid and red dashed lines denote the fitted equipotentials with a total cross polar cap potential of Φ_{PC} = 49 kV for this map. The CPCP is determined by calculating the potential difference between the highest and lowest electrostatic potentials.

2.1.7 Index of refraction effect on measured HF Doppler velocity

We discussed in Section 2.1.2 how SuperDARN radars measure the Doppler velocity of coherent echoes. Equation 2.8 indicates that the measured velocity is proportional to the speed of light in vacuum. The procedure assumes that the radar electromagnetic waves propagate with the speed of light in vacuum. In reality, this is not the case because radio waves get scattered from irregularities in a medium with the index of refraction *n* that is not unity. It has been shown that for such scattering, the value of the velocity should be replaced by c/n [Ginzburg, 1964]. To give a sense of the effect, for ionospheric plasma at F region heights, the index of refraction at high frequencies is

$$n = \sqrt{1 - f_p^2 / f_r^2}, \tag{2.23}$$

where f_r is the frequency of the radio wave, $f_p = 8.98\sqrt{n_e}$ is the plasma frequency in Hz, if the local electron density n_e is given in m^{-3} [Hargreaves, 1992]. For electron densities of $\sim 3\times10^{11}\,\mathrm{m}^{-3}$, Equation 2.23 gives *n*=0.9, meaning that the measured (and reported) Doppler velocity is smaller than that in a vacuum. Although this has been known for many years, only recently it was realized that the effect is indeed acting in HF measurements and leads to the so-called "HF velocity underestimation" with HF radars [Gillies et al., 2009; Ponomarenko et al., 2009]. The issue arose when the Doppler velocity of HF coherent echoes was compared with the true $\mathbf{E}\times\mathbf{B}$ drift of the plasma, and it was found that the coherent HF velocity is systematically smaller than the expected velocity values (see Section 2.3). Although the importance of the index of refraction effect is well accepted, the standard SuperDARN data files contain Doppler velocities

which are not corrected for this effect. One reason is that the electron density is typically not known, except for a few special experiments. The other reason is that the index of refraction effect cannot explain all the differences between the velocity of HF echoes and the $\mathbf{E}\times\mathbf{B}$ drift [Koustov et al., 2016]. In this thesis, we will consider the standard velocities of HF echoes, as reported by SuperDARN (Chapters 3 - 5), and the corrected ones whenever it was possible (Chapter 3).

The dependence of HF velocity upon the index of refraction spurred research into using electron density estimates from SuperDARN velocity measurements at two close frequencies [Gillies et al., 2012; Spaleta and Bristow, 2015; Sarno-Smith et al., 2016]. Unfortunately, a direct comparison of HF electron density estimates with electron density measurements in the scattering volume with the European incoherent scatter radar (EISCAT) proved that the method does not work [Sarno-Smith et al., 2016]. The reasons for this are unknown. One possibility is that HF coherent echoes from a scattering volume come from localized blobs with enhanced electron density and decreased plasma drift. How to investigate this possibility with the currently available instruments is not clear.

2.2 Principles of incoherent scatter radar measurements

The incoherent scatter radar (ISR) has proven to be the one ground-based radio technique which can provide the most information about the terrestrial ionosphere. Contrary to HF radars, ISRs transmit VHF (meter) or UHF (tens of cm) radio waves and receive echoes at large elevation angles of $> 45°$. ISRs provide high-resolution measurements in both time (down to second scales) and space (as low as kilometer scales) of many parameters including the electron and ion temperature, l-o-s Doppler velocity (electric field), and plasma density. ISRs are particularly useful because temperature values from ground-based instruments are generally difficult to come by, and they provide more detailed electron density profiles than other instruments, like ionosondes. Although ISRs are expensive and their data require complex fitting routines, they relay detailed plasma diagnostics, give data for a wide variety of scale sizes, and their scatter is always present even when the ionosphere is exceptionally perturbed, for example during a massive geomagnetic storm.

2.2.1 Theory of ISR

The first ISR plasma theory was developed in the 1960s [Dougherty and Farley, 1960; Fejer, 1960; Salpeter, 1960], and then refined further to include the magnetic field effect [Farley et al., 1961;

Fejer, 1961; Hagfors, 1961; Salpeter, 1961; Rosenbluth and Rostoker, 1962]. Additional theoretical aspects were the inclusion of the effects of ion-ion collisions [Dougherty, 1964 and Woodman, 1967], and more recently, the influence of plasma-beam interactions on the ion spectrum measurements [Diaz et al., 2011].

All new theories are in agreement that it is inappropriate to consider electrons as 'free' to move in the ionosphere, as was initially suggested during the construction of the first ISR. This is because of the electrostatic forces that exist between electrons and neighboring positively charged ions. Due to these forces, ions tend to be attracted towards individual electrons, while at the same time their thermal motions and their mutual repulsion tend to disperse the electrons. As a result, the ions form a shielding layer around each electron, the scale of which is determined by the balance between electrostatic potential energy and random thermal energy. The Debye radius or Debye length quantitatively represents this scale. The Debye length is given as

$$\lambda_D = \sqrt{\frac{\varepsilon_0 T_e}{n_e e^2}}, \tag{2.24}$$

where e and n_e are the electron charge and the electron density, respectively, T_e is the electron temperature in eV and ε_0 is the permittivity of free space [Hargreaves, 1992]. The shielding is such that the potential around the point charge is zero for distances larger than the Debye length, meaning that Coulomb interactions stop at the Debye length due to the screening by other charges. For the ionospheric plasma, a typical value of the Debye length is ~1 cm.

When there are no structures within a quasi-neutral plasma, the scattered radiation from the electrons will be randomly phased. This means that there will be no coherent addition of any kind as electromagnetic waves (transmitted by a radar) are scattered by plasma fluctuations, and the scattered power will be weak. If the radar wavelength is much less than a Debye length, the observed spectrum would agree with the original expectation that the scatter comes from individual electrons, and we refer to this as "incoherent scatter." However, if the radar wavelength is much larger than a Debye length, as is usually the case, the scattered radiation from the electrons will oscillate in phase, increasing the signal. This is because electrons can no longer be considered free and independent, but controlled by the surrounding ions. As a result of electrostatic forces between electrons and neighboring positively charged ions, the ion-acoustic waves and electron plasma waves are excited. These waves dominate the plasma perturbations (because they decay slower

than other types of waves) and excite electron density fluctuations that give rise to the scattered electromagnetic waves/signals received on the ground by an ISR.

2.2.2 Method of observation

ISR radars can be pulsed or of continuous (CW) wave radiation type. Pulsed radars transmit short or long pulses and measure the time delay for the echo signal between transmission and reception to determine the range to the scattering medium. A CW radar involves a continuous-wave signal transmitted vertically upward by one aerial, and the scattered signal is received by a second aerial at a suitable distance so that the intersection of the two beams defines the altitude. This method is sometimes referred to as bistatic or multistatic method, depending on whether two or more separate aerials are used. The multistatic method is currently being employed by the European Incoherent Scatter Scientific Association (EISCAT) radar [Folkestadt et al., 1983]. One advantage of EISCAT is that it provides 3-D measurements of the plasma drift. The disadvantage of this method is that it can only provide a measurement of one height profile at a time and requires three radar sites to achieve a total vector of the plasma drift velocity.

2.2.3 Spectral features and parameters measured

There are three sets of spectral peaks associated with the solutions to the electrostatic dispersion relation for a cold magnetized plasma, such as the ionospheric plasma. These are a double-humped ion line, distributed on either side of the transmitted frequency (typically around +/-5 KHz), a gyro line, and a plasma line. Of the three spectral lines, the ion line is the most commonly used for inferring ionospheric parameters.

The ion line is produced by Bragg scattering of electromagnetic waves from ion-acoustic waves and, as a result, its structure depends greatly on two factors, the ion thermal motions, and Landau damping. The latter, in particular being the primary mechanism of attenuation, broadens the frequencies of two independent peaks, resulting in them overlapping to form a double-humped shape, see in Figure 2.8. From the shape, many ISR parameters can be inferred. The velocity is found by determining the Doppler shift of the entire ion line, which is proportional to the $\mathbf{E}\times\mathbf{B}$ l-o-s bulk plasma drift component. The vertical distance from the tip of the peak to the bottom of the trough of the ion line relates to the electron-ion temperature ratio (T_e/T_i). Lastly, since the total

scattered power in the volume irradiated is approximately equal to $n_e/(1+T_e/T_i)$, the electron density can be extracted given that the ratio of electron temperature to ion temperature can be determined from the spectral shape [Evans, 1968].

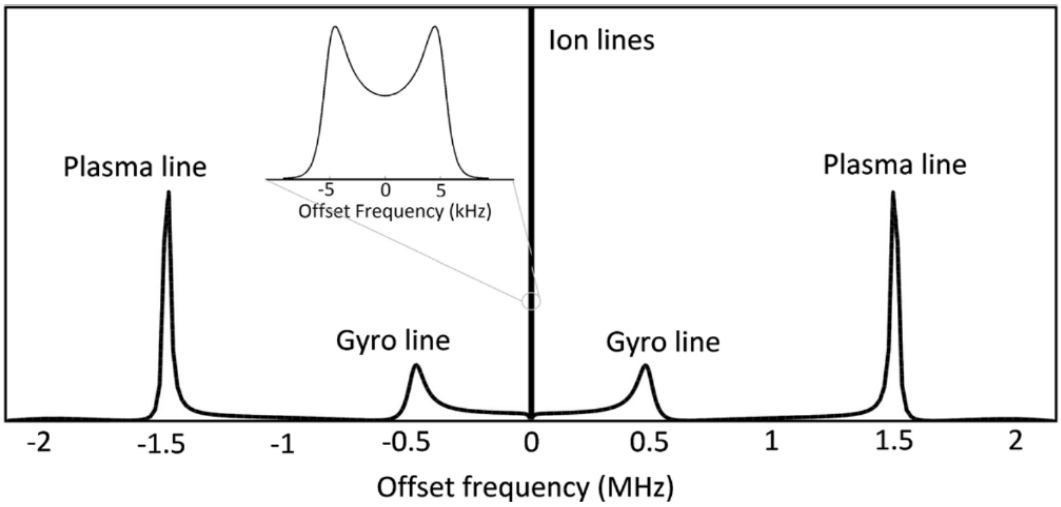

Figure 2.8: An example of the ISR backscatter spectrum. From Akbari et al. [2017].

At altitudes below 120 km, ion-neutral collision frequency can also be determined from the spectral width. At these heights, ion-acoustic waves can no longer propagate as a result of the ion-neutral collision frequency being far greater than the frequency of the ion-acoustic wave so that the spectrum loses its double-humped feature and becomes narrower. Once the parameters listed above have been determined, other parameters such as static electric fields and the temperature of the neutral atmosphere can be inferred [Evans, 1968].

The electron lines comprise the gyro line and the plasma line. The contribution of the ionic component to the gyro and plasma lines is negligible when the condition $m_e/m_i \ll \sin^2\alpha$ (where the symbol α is the angle between the radar l-o-s and the perpendicular of the magnetic field) is satisfied. This condition is usually satisfied except at the geomagnetic equator where the wavevector may be perpendicular to the magnetic field. Notably, the energy in the electron line is less than that in the ion line by a factor of $k_s^2\lambda_D^2$ [Akbari et al., 2017]. Thus amplitudes of the gyro and plasma lines are much smaller than that of ion lines. As a result of this, signal levels of the electron lines often fall below radar detectability in the measured ISR spectra.

2.2.4 RISR incoherent scatter radars

The beginning of the 21st century marked the age of the Advanced Modular Incoherent Scatter Radar **(**AMISR) development. Unlike earlier models of ISRs, AMISR is operated remotely and designed for easy dismantling and relocation. Currently, three of these radars have been developed. One near Fairbanks, Alaska (Poker Flat ISR, PFISR) and two at Resolute Bay (Resolute Bay ISR-North, RISR-N [Bahcivan et al., 2010], and Resolute Bay ISR-Canada, RISR-C [Gillies et al., 2016]). Figure 2.9 shows the RISR faces deployed at Resolute Bay, Canada. Each radar uses a set of panels each consisting of 128 individual transmit-receive units to produce either 11 or 51 narrow (1°) beams electronically steerable in azimuth and elevation angle. The number of beams generated depends on the mode of operation. The former is the World Day mode, while the latter represents the Imaging mode. The radar operates in the UHF band of 430-450 MHz with a total peak transmit power of approximately 2 MW. Typical pulse lengths are from $1\,\mu$s to 2 ms. The range resolution varies from 600 m to 72 km, depending on the pulse length. Time resolutions are approximately 3 min and 1 min for the E region and F region measurements, respectively. Figure 2.10 shows all 22 beam directions for RISR-C and RISR-N during a World Day mode experiment to study ionospheric polar cap flows [Gillies et al., 2016].

Figure 2.9: The Resolute Bay ISR-N and RISR-C radar transmit-receive panels. Adapted from https://www.sri.com/blog/sri-research-ends-earth (last access: September 2018).

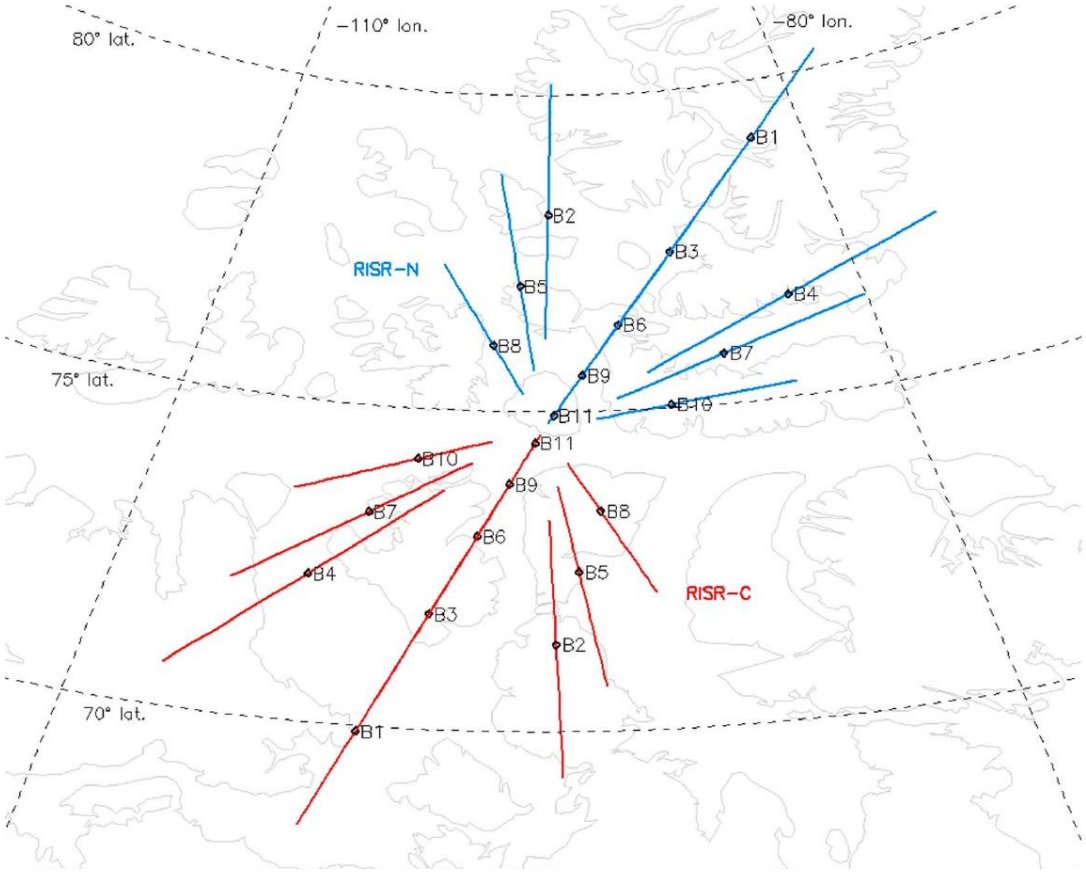

Figure 2.10: The 11 beam directions for the RISR-C and RISR-N radars in the World Day mode. The diamonds on the beam lines represent the locations of the ionospheric pierce points at 300 km. Beams numbered 1–11 north of ~75° latitude are for RISR-N (blue lines), while beams numbered 1–11 south of ~75° are for RISR-C (red lines). From Gillies et al. [2016].

2.2.5 Derivation of $\mathbf{E}\times\mathbf{B}$ plasma drift velocity by RISR

All the l-o-s velocity data V_{los}^{i} collected by an ISR can generally be described as

$$V_{los}^{i} = \boldsymbol{k}^{i} \cdot \boldsymbol{V}_{i}, \tag{2.25}$$

where $\boldsymbol{V}_{i}$ is the true vector $\mathbf{E}\times\mathbf{B}$ drift with North, East and vertically Up components, and $\boldsymbol{k}^{i}$ is a 2×3 tensor characterizing the unit vectors of the radar directions in a selected coordinate system, traditionally the geomagnetic coordinate system. L-o-s velocities are determined in some points and some directions. The task is to determine $\boldsymbol{V}_{i}$ from V_{los}^{i}.

The most straightforward way of inferring a full $\mathbf{E}\times\mathbf{B}$ drift vector from individual l-o-s velocity measurements would be to merge two velocities from two different directions, as described in Section 2.1.5. This is often referred to as the "two-point" solution [Heinselman and Nicolls, 2008]. The two-point solution requires an assumption that the flow is uniform over the space separating the beams. Also, in this case, one must assume that the velocity of plasma flow along the magnetic field is zero ($V_{//} = 0$). For HF (coherent) radars, this condition is almost certainly satisfied since the off-orthogonality of F region backscatter is minimal owing to the ionospheric irregularities being strongly magnetically field-aligned. For the case of ISRs, this condition is generally not valid, but the velocities are typically small, $V_{//} \sim 50$ m/s [Yamazaki et al., 2017]. In the standard RISR method [Heinselman and Nicolls, 2008], $V_{//}$ is assumed to be zero and the task is to find a solution that would be optimal. One approach is to select only beams that are significantly apart in azimuth so that merging would not be a subject of significant errors [Heinselman and Nicolls, 2008]. The two-point solution would be unique and unambiguous, but not all information would be used, and in this sense, the solution would be not optimal. The advantage of the RISR radar is that it provides simultaneous $\mathbf{E}\times\mathbf{B}$ l-o-s components along its many beams and gates, and the primary task is to determine an optimal solution that would take into consideration all the information available. In the current version of the vector field derivation with the RISR radars, the Bayesian approach to the problem solution has been adopted [Heinselman and Nicolls, 2008]. In this approach, Equation 2.25 is presented as

$$V_{los}^{i} = \boldsymbol{k}^{i} \cdot \boldsymbol{V}_{i} + e_{los}^{i}, \tag{2.26}$$

where e_{los}^{i} is an error associated with the l-o-s velocity determination, which comes from the fitting procedure of the autocorrelation function for the backscatter ISR ion spectrum line. Equation 2.26 is a vector equation valid for each point of measurements. It can be written as

$$\begin{bmatrix} v_{los1}^{1} \\ v_{los1}^{2} \\ \vdots \\ v_{los1}^{n} \end{bmatrix} = \begin{bmatrix} k_{pe}^{1} & k_{pn}^{1} & k_{ap}^{1} \\ k_{pe}^{2} & k_{pn}^{2} & k_{ap}^{2} \\ \vdots & \vdots & \vdots \\ k_{pe}^{n} & k_{pn}^{n} & k_{ap}^{n} \end{bmatrix} \begin{bmatrix} v_{pe} \\ v_{pn} \\ v_{ap} \end{bmatrix} + \begin{bmatrix} e_{los}^{1} \\ e_{los}^{2} \\ \vdots \\ e_{los}^{n} \end{bmatrix} \tag{2.27}$$

or

$$\boldsymbol{V}_{los} = \boldsymbol{A} \cdot \boldsymbol{V}_{i} + \boldsymbol{e}_{los},$$

where subscripts v_{pe}, v_{pn}, and v_{ap} are the perpendicular east, perpendicular north, and antiparallel, respectively. Assuming $\boldsymbol{V}_i$ to be a Gaussian random variable (hence, the Bayesian model) and taking it to have a zero mean with covariance Σ_v, a linear theory can be used to derive a least squares estimator. Consider also the measurement error vector e_{los}^i to be Gaussian, zero mean and with a covariance Σ_e. With these constraints, it can be shown that the least squares estimator is a linear function of the zero-mean case.

The Bayesian approach assumes that $\boldsymbol{V}_i$ is a Gaussian random variable, and the linear inverse solution of Equation 2.27 is sought. Generally, this is an ill-posed problem, and the solution is not unique so that specific additional information is required to select a solution relevant to the problem. Heinselman and Nicolls [2008] proposed to assume $\langle \boldsymbol{V}_i \rangle = 0$ with covariance Σ_v. The covariance matrix includes the a priori information to be imposed on the data – the projected range of variability of the velocity in different directions. It is assumed that the error vector is Gaussian in shape with zero mean and covariance Σ_e. In general theory of ill-posed problems, it has been shown that the solution for a linear function with zero mean cases can be presented as [Aster, 2005; Tarantula, 2005]

$$\hat{\boldsymbol{V}}_i = \Sigma_v A^T \left(A \Sigma_v A^T + \Sigma_e \right)^{-1} v_{los} . \tag{2.28}$$

The covariance of the estimate is thus given by

$$\Sigma_{\hat{v}} = \Sigma_v - \Sigma_v A^T \left(A \Sigma_v A^T + \Sigma_e \right)^{-1} A \Sigma_v ,$$

$$\Sigma_{\hat{v}} = \left(A^T \Sigma_e^{-1} A + \Sigma_v^{-1} \right)^1 . \tag{2.29}$$

The second expression for the covariance matrix reveals how the new information from the measurements (with covariance Σ_e) reduces the covariance of the estimate. The effectiveness of details is determined by the geometry information in the matrix A. The approach has several advantageous features. The most important one is accounting for the measurement variances (via Σ_e) for any number of measurements. It favors using three line of sights or more at each point because the additional information is weighted accordingly. However, the solution can take a single measurement and assign additional components determined from the a priori estimates

(assumed to be 0 over the FoV). This enlarges the data considered, except that the relatively large Σ_v variances will drive the variance estimate in the directions not supported by the measurements. The method applies to measurements of the l-o-s velocities within a particular magnetic latitude bin. The adopted step is $0.25°$. Producing this estimation in bins of magnetic latitude gives the vector velocities as a function of latitude automatically. So, instead of using two-point measurements and then averaging in magnetic latitude, the approach described here optimally uses the full coverage of the measurements.

2.3 Previous comparisons of velocities measured by coherent HF radars and ISRs

The idea that HF coherent radars can measure the $\mathbf{E}\times\mathbf{B}$ plasma drift came from the original work of French scientists who set up a crossed beam experiment in Northern Scandinavia and compared HF Doppler velocities with plasma drift data supplied by the incoherent scatter radar EISCAT [Hanuise et al., 1981; Villain et al., 1985]. One reason for this experiment was that the VHF experiments with the STARE radars (Scandinavian Twin Auroral Radar Experiment) had shown that VHF radars do not show large velocities, because the velocity of E region irregularities do not exceed the ion-acoustic speed of the plasma [Greenwald et al., 1995]. The reasonable agreement of the velocity data from the two systems, as shown by Villain et al. [1985], was the justification for construction of some HF radars in the US, and later in Europe, which resulted in establishing the SuperDARN network [see Greenwald et al., 1995]. Despite the hardly undisputed suggestion that the F region plasma wave/irregularity velocity is not much different from the $\mathbf{E}\times\mathbf{B}$ drift of the bulk plasma, the uncertainties in the propagation paths of HF radio waves and the specifics of coherent signal formation have continuously urged researchers to evaluate how precise this assumption is experimentally.

The early studies by Ruohoniemi et al. [1987] and Eglitis et al. [1998] insisted that the velocity agreement is satisfactory, although the data showed occasional significant disagreements between instruments. In fact, in Ruohoniemi et al. [1987] data, the velocity of HF irregularities was >100 m/s above plasma drifts according to the Soderstrom ISR, which is unexplainable by any theory of F region irregularity formation. The authors attributed the differences to somewhat different temporal and spatial resolutions of the instruments. This idea has dominated for a long time starting from the study by Davies et al. [1999], who considered data from the SuperDARN

HF radar at Hankasalmi and the $\mathbf{E}\times\mathbf{B}$ drift measurements by the EISCAT ISR. Davies et al. [1999] acknowledged that the HF velocities are smaller whenever the Hankasalmi radar detects E region echoes. Low velocities for E region echoes is an expected effect due to the occasional occurrence of the Farley-Buneman instability and a strong velocity depression owing to high collisionality of the bottom side E region plasma [e.g., Uspensky et al., 1994; Gorin et al., 2012]. The data by Davies et al. [1999], and later on by Milan et al. [1999], did show a trend of the HF velocities being below the $\mathbf{E}\times\mathbf{B}$ velocity component. Fewer differences were seen in Eglitis et al. [1998].

New insight on this issue has been offered with the study by Xu et al. [2001], and the subsequent Ph.D. Thesis by Xu [2003], who analyzed plasma velocity data collected by the Soderstrom ISR and the Stokkseyri and Goose Bay SuperDARN radars. These authors, for the first time, concluded that the velocity differences are systematic and significant. They showed that the HF radar velocity is smaller than the l-o-s component of the $\mathbf{E}\times\mathbf{B}$ drift measured by the ISR. Moreover, the effect was seen progressively stronger for larger $\mathbf{E}\times\mathbf{B}$ drifts. The authors considered observations in co-aligned SuperDARN and ISR beams and 2-D vectors (inferred from ISR measurements) projected onto HF radar beams. The discovered differences have been attributed to some factors including the physics of coherent signal formation. The effect eventually become loosely referred to as the $\mathbf{E}\times\mathbf{B}$ velocity "underestimation" by the SuperDARN radars. Subsequent comparisons of HF velocities with instruments such as the Defense Meteorological Satellite Program (DMSP) satellites and the Canadian Advanced Digital Ionosonde (CADI) data have confirmed the "underestimation" effect [Draton et al., 2005; Xu et al., 2008; Koustov et al., 2009; Mori et al., 2012].

A new impetus in this area has been given by the studies of Gillies et al. [2009] and Ponomarenko et al. [2009], who realized that there is a deficiency in SuperDARN velocity measurements because the reported velocity is computed by assuming that radar waves propagate in a vacuum, as discussed in Section 2.1.7. Ponomarenko et al. [2009] and Gillies et al. [2009, 2010] showed that, after taking into account the index of refraction of the medium, the agreement between the SuperDARN velocity and the $\mathbf{E}\times\mathbf{B}$ drift improves (ISRs and DMSP data were considered). The correction factor was found to be on the order of 10-15%, corresponding to the index of refraction values between 0.85 and 0.95.

Bahcivan et al. [2013] presented RKN data showing that occasionally the radar can detect E region echoes at relatively far ranges, where one usually would expect only F region echoes. The HF signals were assumed to propagate through 1 & 1/2 mode with refraction/reflection at E region heights and bouncing from the ground (on the way to the scattering volume and back). Since the velocity of E region irregularities can be well below the $\mathbf{E}\times\mathbf{B}$ drift magnitude (as mentioned above), a scenario heavily promoted by LaCroix and Moorcroft [2001], then the result can be easily understood. However, it was clear that such events are not very frequent.

Recently, more extensive analysis with the Resolute Bay ISR (RISR) and the PolarDARN radars has been done by Koustov et al. [2016] and Gillies et al. [2018]. The first study focused on l-o-s HF velocity and $\mathbf{E}\times\mathbf{B}$ plasma drift (measured by the RISR-North radar) averaged over several range gates for both systems. The reason for this was that the PolarDARN radars do not see many echoes in the FoV of the RISR-N radar (whose beams are looking toward the North Magnetic Pole), so that typical ranges of echoes were ~ 1500 km. The RKN and INV SuperDARN radars were considered. The authors confirmed that the HF velocity is affected by the index of refraction effect, but simultaneously argued that there are a significant amount of points (~37%) for which the index of refraction correction leads to worsening of the agreement, due to the overestimation of RKN radar l-o-s velocity, especially at low $\mathbf{E}\times\mathbf{B}$ drifts. Moreover, the authors presented one event for which the HF velocity overestimation was, very likely, owing to strong lateral refraction of radio waves as they propagate to the scattering volume. They suggested that the $\mathbf{E}\times\mathbf{B}$ overestimation effect in SuperDARN measurements is a persistent phenomenon and cannot be attributed to just differences in spatial/temporal resolutions of the instruments and hypothesized that the disagreements can be caused by anomalous HF propagation conditions and signal collection from microstructures in the scattering volume, as initially suggested by Uspensky et al. [1989].

The paper by Gillies et al. [2018] is a comprehensive analysis of Rankin Inlet l-o-s velocity data and RISR measurements in almost co-aligned beams and co-located gates. Data from the RISR-Canada and RISR-North ISR radars were considered. The work has been going on simultaneously as the author of this Thesis was working with RISR-Canada and CLY HF radar data. It is not a surprise that some conclusions in this Thesis and the work by Gillies et al. [2018] are similar although not quite the same. The most important outcome of Gillies et al. [2018] is that for the intermediate radar ranges of ~ 1000 km, the RKN radar l-o-s velocities are reasonably

close to the l-o-s component of the $\mathbf{E}\times\mathbf{B}$ drift provided the index of refraction effect on measured velocity be taken into consideration. At shorter and farther ranges, however, HF velocities were found to be consistently below the $\mathbf{E}\times\mathbf{B}$ drift due to contributions of some signals from the E region. The authors also assumed that many PolarDARN echoes are contaminated with the ground-scattered signals. Such echoes can be identified as low-velocity echoes of < 100 m/s. The authors suggested a simple procedure to remove this kind of echoes from the data by considering only those observations where HF echoes exist in all adjacent radar cells. The cleaned RKN data set showed almost perfect agreement with RISR measurements. One detail is worthy to note; the agreement was much worse for large $\mathbf{E}\times\mathbf{B}$ drifts of ~ 1000 m/ s.

To summarize, we would like to make several important statements relevant to the relationship between the Doppler velocity of coherent HF echoes and the $\mathbf{E}\times\mathbf{B}$ plasma drift as measured by incoherent scatter radars.

1. The HF Doppler velocity is typically below the $\mathbf{E}\times\mathbf{B}$ l-o-s component of the $\mathbf{E}\times\mathbf{B}$ drift about 60% of the time. If the index of refraction correction is applied to these cases, the corrected SuperDARN velocities are in reasonable agreement with ISR data.
2. There are occasional cases when the HF velocity is somewhat above the $\mathbf{E}\times\mathbf{B}$ l-o-s component. These cases account for 30% of overall records. The effect is particularly demonstrated at low $\mathbf{E}\times\mathbf{B}$ drifts.
3. It is not clear whether the agreement holds at substantial plasma drifts > 1000 m/s.

Despite positive progress in establishing SuperDARN-ISR velocity relationship, the reasons for minor differences in velocity measurements are not entirely understood and warrant further investigation.

CHAPTER 3

POLARDARN RADAR LINE-OF-SIGHT (L-O-S) VELOCITY AND $\mathbf{E \times B}$ PLASMA DRIFT

HF radars are well suited for $\mathbf{E \times B}$ plasma drift measurements, as explained in Chapter 2. However, a number of shortcomings of $\mathbf{E \times B}$ full vector derivation from HF radar measurements of the l-o-s velocity have been identified in the past, as described in Section 2.2.5. Despite obvious progress, HF-based $\mathbf{E \times B}$ estimates require further investigation if one wants to further improve the quality of convection mapping with HF radars. In addition, although all the SuperDARN radars work on the same principle and often even have identical hardware, validation for every unit is highly desirable to be confident in reliability and consistency of measurements across the network.

In this chapter, we undertake a validation work for the Clyde River (CLY) PolarDARN radar. This effort is complementary to the previous validation work for the RKN and INV PolarDARN radars by Koustov et al. [2009], Mori et al. [2012], Bahcivan et al. [2013], Koustov et al. [2016], and Gillies et al. [2018]. As of May, 2017, the beginning of this project, such work had not been done for the CLY radar. We also investigated here the RKN radar velocities for completeness. The other important aspect of the RKN work is that we assess the velocities differently, as compared to all the previous studies. We had been aware that Dr. R. Gillies at the U of Calgary was pursuing the RKN validation by employing gate-by-gate comparison of both RISR-N and RISR-C incoherent scatter radars (this work is now published as Gillies et al. [2018]). Unlike Gillies et al. [2018], our database was limited to RISR-C incoherent scatter radar data. Some materials presented in this chapter have been recently published in 'Validation of Clyde River SuperDARN radar velocity measurements with the RISR-C incoherent scatter radar' by A.V. Koustov, R.G. Gillies and P. Bankole [Koustov et al. 2018].

3.1 Introduction

Traditionally, a gate-by-gate comparison of data from two radar systems making measurements in roughly the same directions has been used for validation of SuperDARN radar velocity measurements, e.g., Gillies et al. [2018]. Such an approach cannot be implemented for the CLY

radar and RISR-C geometry because none of their beams are close enough (see map in Figure 1 of Gillies et al. [2018]). For this reason, we adopt here a different approach. Namely, we consider RISR-C 2-D vectors (which are inferred by merging data from individual beams) in a certain area and compare them with highly averaged PolarDARN data (over 3 beams and 4 gates). Thus we assess the data in terms of the average (median) velocities over a large space. The RISR velocity vectors are inferred by merging l-o-s data collected in multiple beams by employing the traditional RISR approach (e.g., Heinselman and Nicolls [2008], as described in Section 2.2.5).

Our general objective here is to assess whether SuperDARN l-o-s velocities used for the construction of 2-D maps are consistent with RISR-C $\mathbf{E}\times\mathbf{B}$ vectors in a statistical sense. We recall that, for construction of global-scale maps of plasma convection, the SuperDARN Potential FIT technique uses median-filtered l-o-s velocities. For a certain grid of measurements, the median velocity is computed by considering 27 raw velocity l-o-s values in the beam/gate and in plus/minus one range gate for plus/minus one radar beam and for plus/minus one scan (the so-called grid velocities). This implies that what eventually goes into the Potential Fit procedure is a highly median-filtered l-o-s HF velocity covering 3-6 min of raw data and a significant space domain. In this view, there is a sense in considering 5-min RISR-C data (that have much smaller errors than alternatively available 1-min data) and compare them with HF velocity medians over the same time periods and large spatial areas.

Although we are aiming in this chapter validation of the CLY velocity measurements, there is more value in the work to be undertaken. This is because the RISR method of velocity estimations has deficiencies as well [Heinselman and Nicolls, 2008]. One of these is an assumption that the flow velocity is spatially uniform over periods of 5 min, which is not always satisfied. The plasma velocity along the magnetic field is also only estimated. In a case of strong inconsistencies found, one can argue that the RISR-C procedure of $\mathbf{E}\times\mathbf{B}$ velocity determination has some deficiencies as well. Thus, our approach can be considered as a mutual validation of radar system performance of both radars.

3.2 Geometry of RISR-C and PolarDARN radar observations

Figure 3.1 shows the fields of view (FoVs) of the PolarDARN radars at CLY and RKN starting from range gates 5, and the location of the RB incoherent scatter radar, which we will refer to,

starting from here, as the RISR radar. We also show here, by colored bars, specific beams of RISR measurements in the "world-day" mode with 11 beams. In this configuration, the data from all 11 beams are used to infer the $\mathbf{E}\times\mathbf{B}$ full vector every $0.25°$ step of magnetic/geographic latitude. The pierce points of the beams at the height of 300 km are shown in Figure 3.1 by color; the majority of the beams are colored in pink except the central beams (oriented in the same direction but at various elevation angles) that are denoted by blue and green color. The actual centerline for the merging points depends on data availability in specific beams; however, it is roughly along the magnetic meridian as shown in Figure 3.1 by the black dots. We note that in the "imaging mode" with 51 beams [Heinselman and Nicolls, 2008], the procedure and data output are the same except for more data are involved.

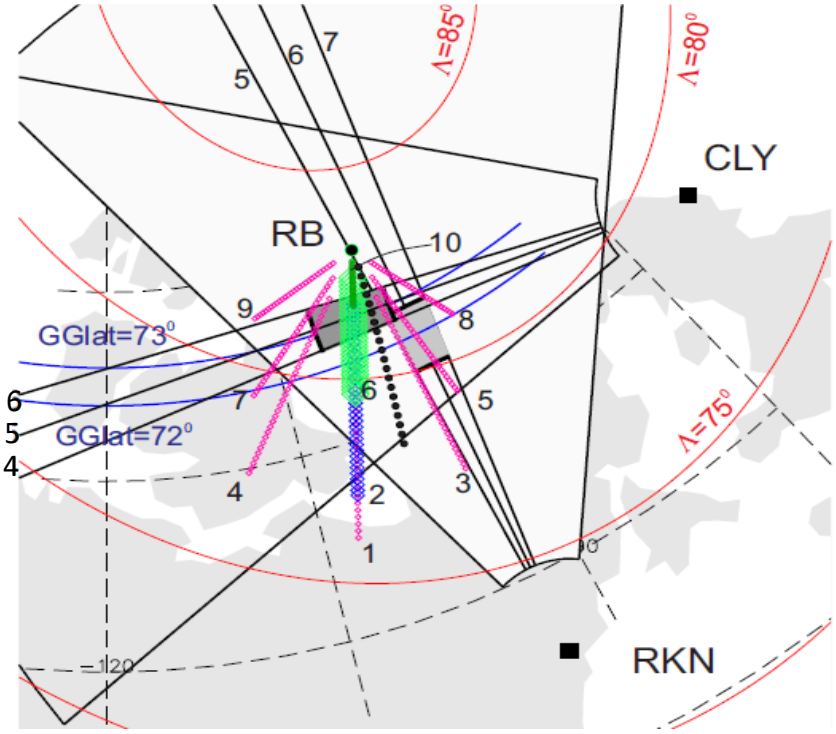

Figure 3.1: Fields of view of the PolarDARN radars at Rankin Inlet (RKN) and Clyde River (CLY). The black straight lines are the orientation of specific beams (4-6 for CLY and 5-7 for RKN) whose data were investigated. Shaded areas represent areas of HF radar data averaging. RB is the location of the RISR-C incoherent scatter radar. The radar reports $\mathbf{E}\times\mathbf{B}$ vectors with a resolution of $0.25°$ geographic latitude as the points shown as black circles stretching roughly along the magnetic meridian crossing the RB zenith. The blue-colored circles are the locations where data were used for comparison with the CLY measurements. The solid red lines are the magnetic latitudes of $75°, 80°$ and $85°$.

Figure 3.1 also shows the orientation of the CLY beams 4, 5, 6 (their centers) that we considered and the area where data were considered, the shaded rectangle outlined by beams 4 and 6 between range gates 18-21. An important feature of this area is that here the beams are almost parallel to the lines of equal geographic latitude at the chosen radar range gates (18-21), as shown in Figure 3.1. This means that one can directly compare CLY l-o-s velocity and the Eastward component (in geographic coordinates) of RISR velocity vector.

We also show in Figure 3.1 the area and RKN beam orientations for the joint RKN-RISR comparison that we will consider as well, for completeness of the investigation and to confirm the consistency of these radars within the adopted, somewhat different approach as compared to other studies. We consider here RKN data in beams 5, 6 and 7 and radar range gates 20-22. The monitored ionospheric region is centered at a geographic latitude of $\sim 72°$, and the RKN beam look directions are close to the geographic meridian of this radar location so that the HF velocity can be directly compared with the Northward component of the RISR velocity.

3.3 Methodology of the l-o-s velocity comparison

We consider here an extensive data set comprised of observations from the entire year 2016. Table 3.1 presents the periods of RISR measurements. Overall, about 1,065 hours of RISR measurements are available. The radar typically operated for 24 hours switching, once in a while, its mode of operation, except world-day mode, which usually covers an entire day. The data are from two seasons, winter and equinoxes, with no measurements for summer time. In Table 3.1, some events are marked in gray. Data from these events have been investigated but eventually dropped from statistics because ionosphere measurements there are highly contaminated by ground scatter signals existing in neighbouring gate.

Figure 3.2 shows the total number of 5-min intervals of RISR measurements compared with RKN and CLY versus UT. The diurnal variations of the number of intervals in Figure 3.2 are similar, with a minimum between 4 and 12 UT and a maximum between 16 and 2 UT. The minimum corresponds to nighttime, while the maximum corresponds to daytime. The number of intervals for RKN is greater than that of CLY most of the time. The data availability in Figure 3.2 is strongly influenced by HF coherent echo occurrence rates that vary significantly [Ghezelbash et al., 2014].

Table 3.1: List of all RISR periods of measurements considered in this study. Rows highlighted by gray color represent CLY-RISR events that were investigated, but eventually dropped from the database.

Date		**RISR**		**Date**		**RISR**	
Month	Day	Start_time	End_time	Month	Day	Start_time	End_time
1	14	18.55	23.53	3	7	0.00	23.59
1	16	2.14	23.55	3	8	0.04	23.58
1	19	19.21	23.56	3	9	0.03	19.55
1	20	0.02	22.56	3	16	0.04	23.57
1	21	20.21	23.54	3	17	0.02	23.55
1	22	0.00	23.56	3	18	0.00	19.57
1	23	0.02	23.58	9	24	0.00	8.25
1	24	0.04	23.22	9	26	17.47	22.45
1	25	1.30	23.57	9	27	1.53	23.41
1	26	0.02	23.54	9	28	3.01	21.52
1	27	0.00	23.55	9	29	3.01	23.54
1	28	0.00	23.57	9	30	2.31	23.54
1	29	0.02	23.59	10	1	2.31	10.56
1	30	0.05	23.55	10	12	21.41	23.55
2	1	0.01	23.58	10	13	0.00	23.57
2	2	0.03	23.56	10	14	0.02	23.57
2	3	0.02	23.59	10	15	0.02	13.75
2	4	0.05	23.58	11	21	22.12	23.59
2	5	0.03	19.08	11	22	0.05	22.23
2	6	7.00	23.59	11	23	0.01	23.58
2	7	0.04	23.55	11	24	0.04	23.55
2	8	0.01	4.30	11	25	0.01	23.59
3	2	17.04	23.59	11	26	0.05	23.59
3	3	0.04	23.57	11	27	0.04	23.59
3	4	0.02	23.58	12	3	0.00	23.56
3	5	0.04	23.56	12	4	0.01	23.54
3	6	0.01	23.55	12	5	0.00	15.54

Our approach to the CLY-RKN-RISR comparison was as follows. We considered every 5-min period of RISR velocity measurements at latitudes $72.375°$ for CLY and RKN. We then considered the median values of the CLY or RKN velocity over matched 5-min intervals in 3 beams and 4 gates, as described in Section 3.2. One might have a concern that the RISR

observations were limited to a relatively narrow span of latitudes, while the span of latitudes for the HF radars was much wider. To address this concern, we compared RISR data for a wider span of latitudes (all blue circles in Figure 3.1) and found no significant differences with what we will report in this chapter.

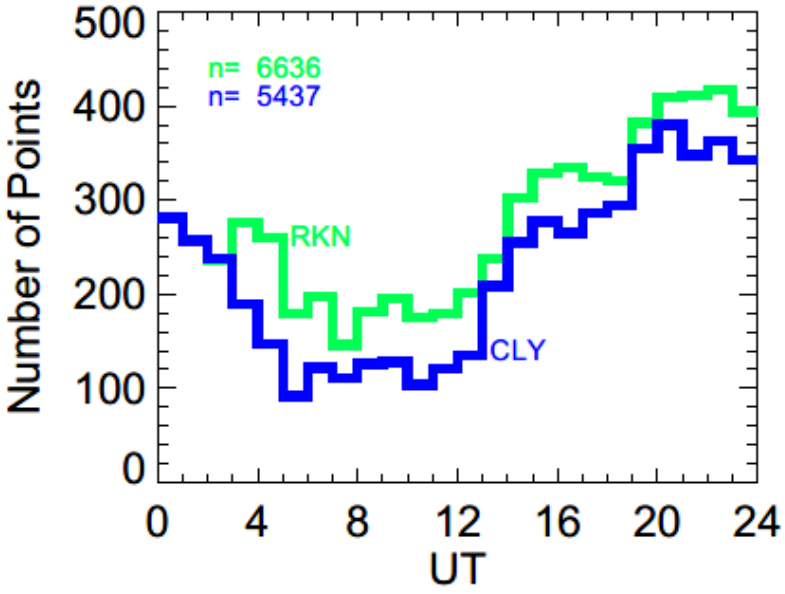

Figure 3.2: Histogram distributions of RKN-RISR (green) and CLY-RISR (blue) 5-min intervals of joint observations for all events considered. Total number of available intervals is shown in the top-left corner for each radar pair.

3.4 An example of individual event analysis: 04 March 2016 case

To demonstrate how the analysis has been done we consider here in detail one event from 04 March 2016. Figure 3.3 shows the distribution of CLY and RISR velocities, in the common areas as explained in Section 3.2, versus UT for the entire day. No CLY echoes were detected between 05 and 09 UT. Both data sets show significant variability with the RISR point spread being much larger. To some extent, this is because the CLY velocities shown are the velocity medians that were computed from individual 1-min measurements and matched with 5-min intervals of RISR observations.

In Figure 3.3, one can recognize a clear diurnal variation of the velocity with largest magnitudes at ~13-16 UT (negative values, correspond to the plasma flow away from the CLY radar) and 21-23 UT (positive values, correspond to the plasma flow toward the CLY radar). Such

a variation is highly expected since about 75% of the time the global-scale pattern of the high-latitude plasma convection is 2-celled with flows along magnetic parallels at dawn and dusk (see, for example, SuperDARN statistical model output in Cousins and Shepherd [2010]). In Figure 3.3 we observe that the RISR data are clustered around certain values much better during daytime as compared to nighttime. This is probably an inherent property of the high-latitude plasma flows.

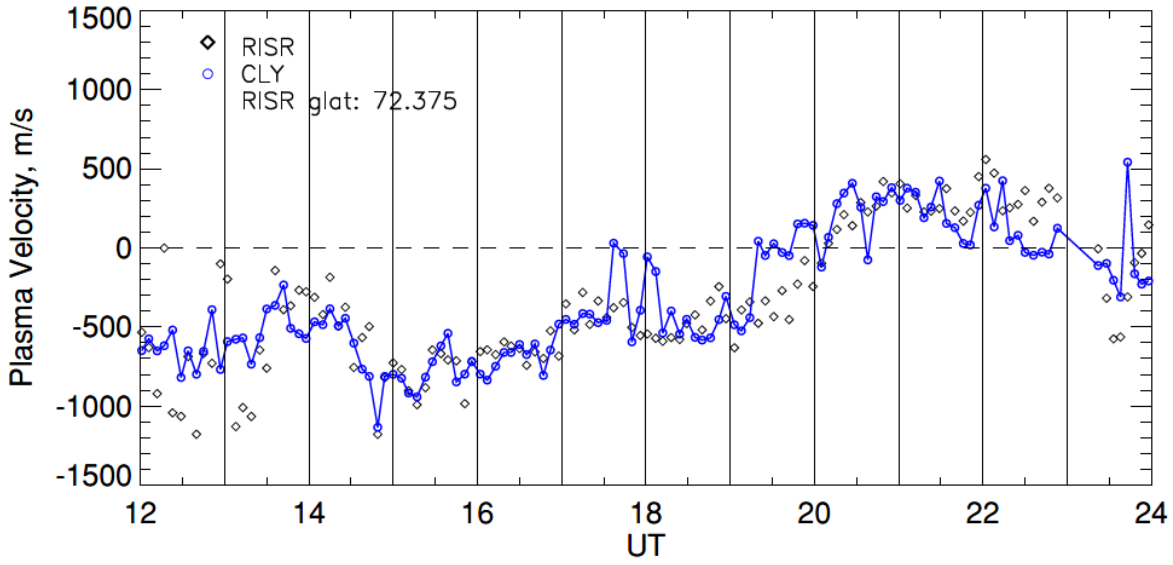

Figure 3.3: Eastward component of the $\mathbf{E \times B}$ drift as measured by RISR (black diamonds, 5-min resolution data) and matched velocity medians of Clyde River (CLY) observations (blue circles, 5-min medians of original 1-min measurements in beams/gates "overlapping" the region of RISR observations) for the event of 04 March 2016.

One important conclusion from Figure 3.3 is that the velocities measured by the two independent instruments are relatively close to each other, although seldom coinciding. In general, the blue line magnitudes (CLY values) are smaller than the black diamonds (RISR values). This is a well-known feature from previous publications (e.g., Xu et al. [2001]). An interesting detail of the data is that between 17 and 19 UT, there are several points where CLY velocities are close to zero while RISR velocities are around -500 m/s. A potential reason for such strong differences will be discussed later in Section 3.8.1.

To better visualize the differences between the velocities in Figure 3.3, we plot the pairs of data as a scatter plot in Figure 3.4. The cloud of points in Figure 3.4 is spread around the bisector of perfect agreement with the exception of a cluster of low CLY velocities of < 200 m/s at RISR velocities around -500 m/s. Since the data are stretched along the bisector, we can expect a linear

relationship between the two quantities, and we can characterize the relationship in terms of the best-fit line applied to the large blue dots that are velocity medians in bins (with a 100 m/s step) of RISR velocity. We use median values because they better represent a typical value for data that show significant number of outliers. Performed computations of average values gave a comparable value, although variability on the plot was high. The slope of the line is 0.68 and is consistent with the results of other observations, for example, Koustov et al. [2016] and references therein. We note that as we used here a different approach in data handling, the estimated slope is a very robust result across various methods of comparison between the HF velocity and the $\mathbf{E}\times\mathbf{B}$ drift.

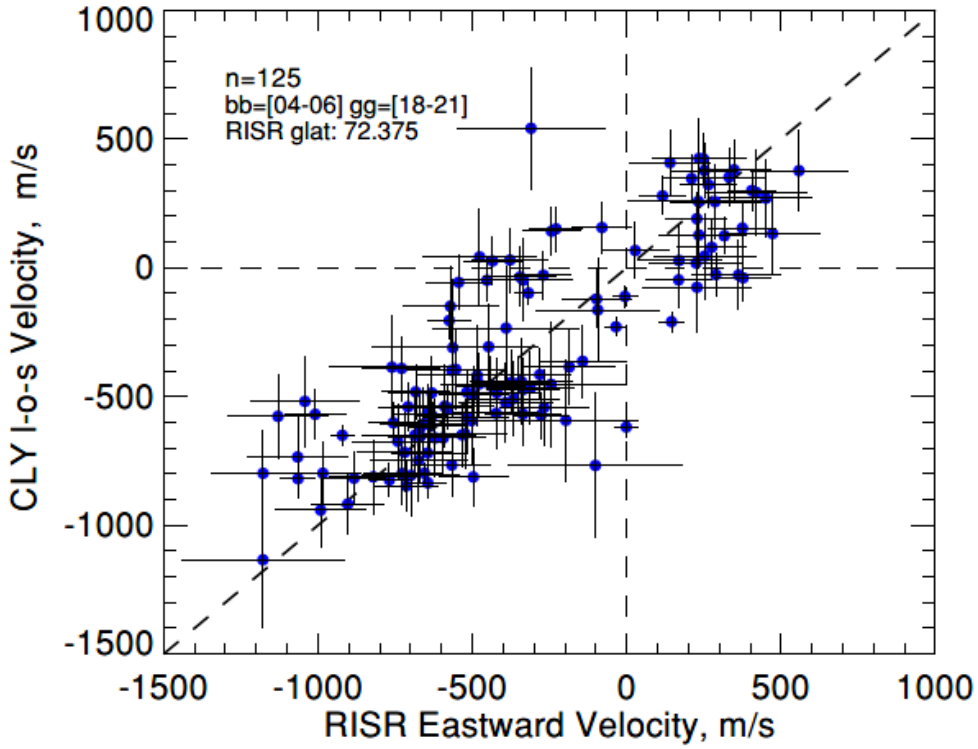

Figure 3.4: A scatterplot of the Clyde River (CLY) l-o-s velocity versus $\mathbf{E}\times\mathbf{B}$ Eastward velocity component as inferred by RISR. The CLY radar beams and gates considered are shown in the top left corner. The black vertical and horizontal lines are the standard deviations of all CLY and RISR velocities, respectively.

3.5 Analysis of the entire database

A similar approach has been applied to all data available for 2016 as presented in Table 3.1. To give a general sense of typical velocities measured by the systems, we present in Figures 3.5a and 3.5b the histogram distributions, separately, for CLY-RISR and RKN-RISR joint observations. In

both cases, the velocities were mostly between -400 m/s and 400 m/s. The HF velocities show somewhat narrower distribution than the RISR velocities (as expected from the data of Figure 3.3).

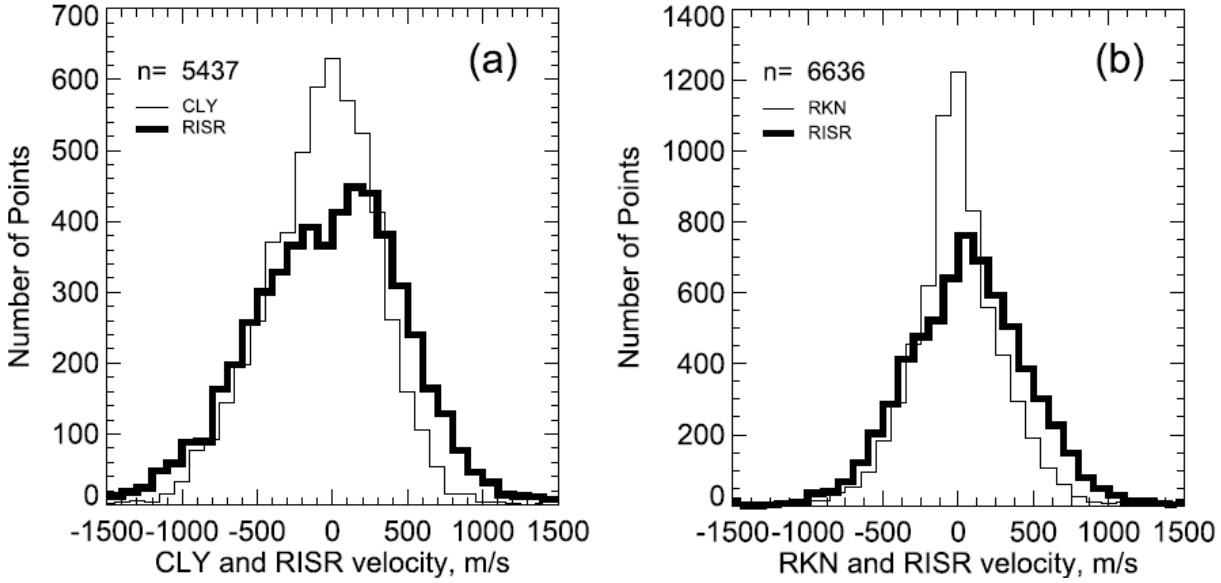

Figure 3.5: Histogram distribution of the velocities, measured by the RISR radar, (a) CLY and (b) RKN PolarDARN radars.

3.5.1 CLY-RISR comparison

In Figure 3.6a we plot the CLY l-o-s velocity versus the RISR Eastward $\mathbf{E \times B}$ component for all 55 events in the entire database. The total number of points was more than 5000, which is a significant number compared to earlier studies. Overall, both positive and negative velocities are well represented. The best linear fit line to the CLY binned velocity (using 100-m/s bins of the RISR velocity), the blue dots in Figure 3.6a, gives a slope of 0.51. This is poorer agreement than that for 04 March, presented in Figure 3.3. We point at one interesting effect in Figure 3.6a. Namely, the CLY velocities are clustered around -100 m/s, while RISR velocities vary in between -700 to -100 m/s. We also binned the data of Figure 3.6a based on bins of the CLY velocity, which are shown as red dots. The dots are fairly close to the line of perfect agreement. Not very strong differences between the stretching of the red and blue dots in Figure 3.6a indicates that the velocities are related almost linearly, especially in the range -500 m/s to +500 m/s.

The same data are shown as a contour plot in Figure 3.6b. The majority of points are close to the bisector, in agreement with the conclusion drawn from Figure 3.6a.

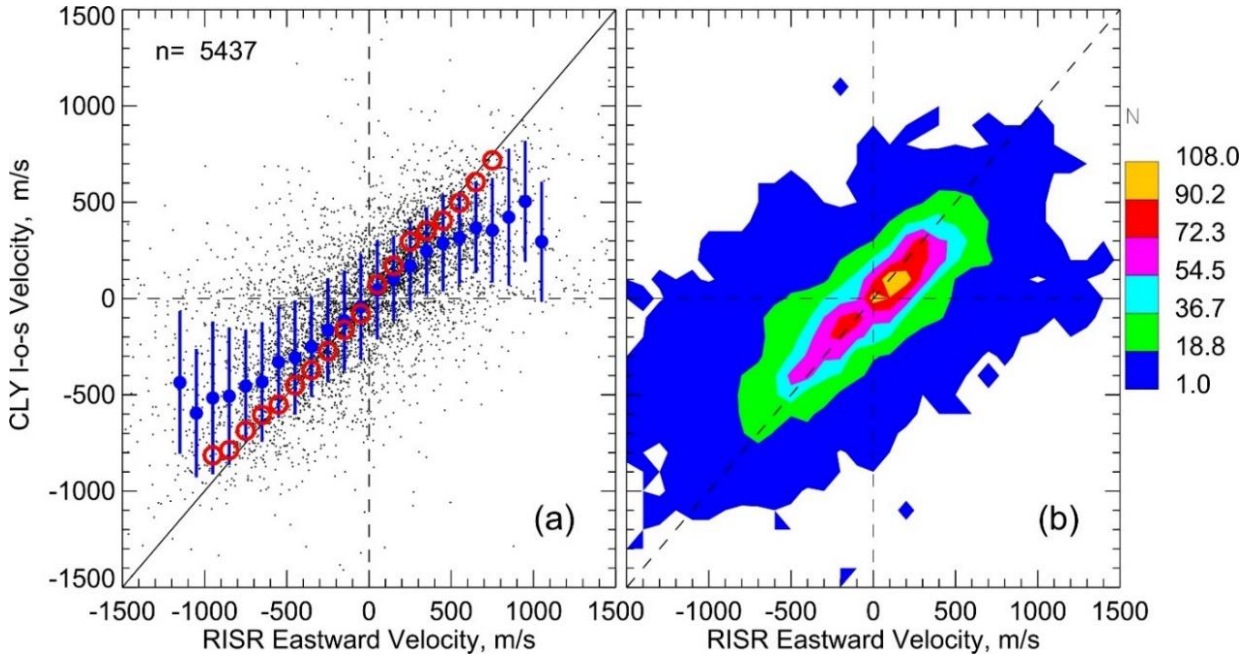

Figure 3.6: (a) Scatterplot of the Clyde River (CLY) l-o-s velocity versus the $\mathbf{E \times B}$ Eastward velocity component as inferred by RISR. The total number of points *n* is shown in the top left corner. The blue dots are the medians of the CLY velocity in 100-m/s bins of RISR measurements. The blue vertical lines are the standard deviations of the CLY velocity in each bin. The red open circles are medians of the RISR velocity in 100-m/s bins of CLY measurements (b) Contour representation of the number of points in the velocity data of panel (a).

3.5.2 RKN-RISR comparison

To compare RKN and RISR velocities, we considered all 55 events RISR events listed in Table 3.1. Steps similar to the CLY analysis were undertaken. The total number of points was higher here in accordance with the generally better echo occurrence for the RKN radar [Ghezelbash et al., 2014]. Both positive and negative velocities were well represented in the data set as well. The results of the analysis are presented in Figure 3.7.

Figure 3.7 gives smaller a slope of 0.38 for the linear fit line suggesting statistically smaller RKN velocities as compared to CLY velocities for the same RISR velocities. Whether this effect is significant is hard to judge; clearly, the slope would improve if measurements at large RISR magnitudes (these bins do not have many points) are not considered. So, one can claim that the slopes are comparable for the CLY and RKN radars. The RKN data also showed presence of large amount of points with very low-velocity magnitude of < 100 m/s as seen as horizontally stretched clouds of points. This issue will be discussed later in Section 3.8.1.

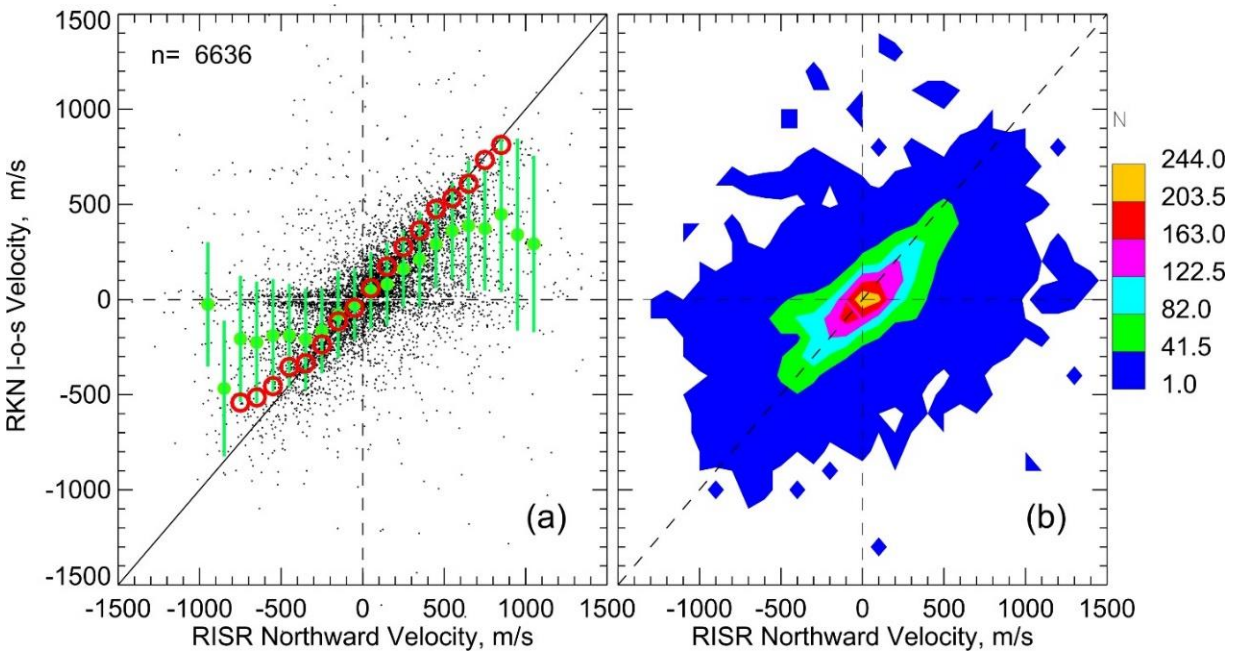

Figure 3.7: (a) Scatterplot of the Rankin Inlet (RKN) l-o-s velocity versus the $\mathbf{E \times B}$ Northward velocity component as inferred by RISR. The total number of points *n* is shown in the top left corner. The green dots are medians of the RKN velocity in 100-m/s bins of RISR measurements. The green vertical lines are the standard deviations of the RKN velocity in each bin. The red open circles are medians of the RISR velocity in 100-m/s bins of RKN measurements. Contour representation of the number of points in the velocity data of panel (a).

3.6 2-D comparison of RISR-C and SuperDARN vectors

As mentioned earlier, comparisons of coherent and incoherent radar velocity measurements have been mostly focused on gate-by-gate comparison in one direction. This is important in order to understand the reasons for velocity disagreements for the instruments. However, of equal importance is the practical question of the difference in the determined vectors of the instruments. Similarity of vector estimates by RISR and SuperDARN is expected, but to what degree is highly unknown (see Section 2.3). In this section, we undertake a comparison of 2-D velocity vectors obtained by the RISR and SuperDARN radars.

3.6.1 Approach to the analysis

The approach to the data analysis was as follows. First, we limited comparison to the area where the CLY radar was monitoring echoes, beams 4-6 and range gates 18-21 (Figure 3.1). This choice was for a simple reason that 2-D vectors inferred from SuperDARN mapping could be checked with respect to the original raw data by the RKN and CLY radars, and we have made this comparison in all cases. SuperDARN convection vectors are given on a grid of 1° in magnetic latitude (assigned latitudes are 80.5° and 81.5°) and about 7° in magnetic longitude (at MLATs of $80^\circ - 82^\circ$, the area of interest). We selected the 3 closest grid node locations at MLAT=81.5° and the 2 closest grid node locations at MLAT=80.5°. For each vector location, the eastward component of the flow was computed at each vector location and the median value (out of 5 although for some periods it was as low as 1 measurement) was selected as a representative value of the eastward plasma flow component according to a specific SuperDARN map. In terms of time, because RISR measurements considered had 5-min resolution, standard SuperDARN convection maps with 5-min integration time were produced (the files have been processed by M. Schmidt). This is not a traditional temporal resolution for SuperDARN maps (which is 2 min); such data processing has been done to avoid the need for additional averaging of 2-min SuperDARN maps. Unfortunately, the beginnings of RISR measurement intervals were rather irregular over time, while SuperDARN maps were produced over exact time slots such as 0-5 min, 10-15 min and so on. For comparison, only data from the two systems that were less than 2 min apart were considered. For this reason, even when both radar systems were operational, the actual number of joint points per hour was below the expected number of 12.

For RISR, velocity vectors were usually available such as for all the points shown by the black circles in Figure 3.1. For the comparison with SuperDARN vectors, only measurements at geographic latitudes between $71.625^\circ - 73.125^\circ$ (given with a resolution of 0.25°) were considered and median values of the Eastward component were computed.

Obtained data pairs were entered into a common dataset for all the events marked by white color in Table 3.1, i.e., by considering the same events as for the l-o-s velocity comparison of Section 3.3. We stress that although the data for comparison was along one specific direction, geographic east, two-dimensional vectors were used in determination of the velocity component for both systems.

3.6.2 Results of vector comparisons

Figure 3.8 plots the eastward component of the plasma flow as determined by to the two systems. Only the contour representation is considered here. We note that the comparison covers a significant range of possible velocities +/- 750 m/s. Overall agreement of the data held, which was expected. There are several details of the plot that are consistent with what has been reported in Sections 3.4 and 3.5. First of all, the SuperDARN map velocities were somewhat smaller than those of RISR; in agreement with the SuperDARN underestimation effect. This is recognized by the noticeable shift of the distribution maxima from the bisector of ideal agreement, especially at RISR positive velocities.

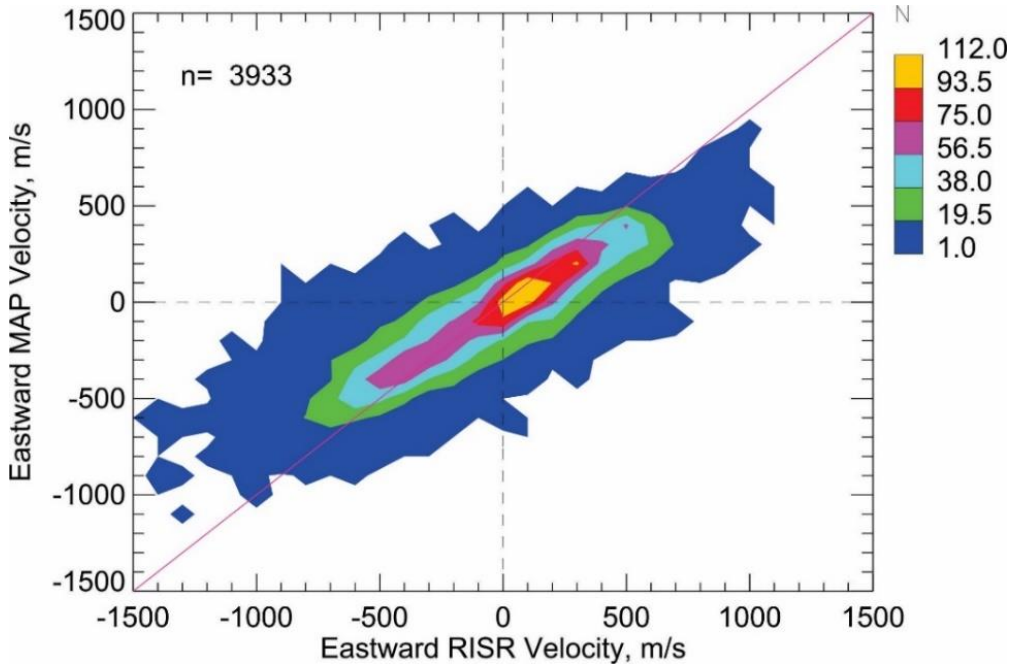

Figure 3.8: Contour plot of the SuperDARN Eastward plasma velocity component (in the area of joint observations with the RISR-C radar, medians in several grid points of the SuperDARN convection maps) versus the same velocity, but as measured by the RISR-C radar in the common area. Observations from January-December 2016 have been considered, with the total number of points n=3993.

Secondly, the underestimation effect is progressively more significant at the larger RISR velocities. This feature is seen at both positive and negative RISR velocities. Finally, as it was the case in the past, there were a number of points for which the radars showed different velocity

polarity. This was more frequent for the small RISR velocities. Although the plot of Figure 3.4 shows good consistency of the data provided by the systems, in individual measurements the differences were as large as a factor of 2. We will report on one interesting case of such a disagreement later in Section 3.9.3.

3.7 PolarDARN-RISR comparison with HF velocity corrected for the index of refraction effect

As discussed in Chapter 2, the SuperDARN HF velocity must be corrected for the index of refraction effect. This cannot be easily done on a regular basis because the information on the electron density in the ionosphere is not readily available. For the joint RISR-PolarDARN observations considered in this chapter, the situation is more favorable because RISR regularly reports the electron density profiles in each of its beams. In this section, we compare RISR and PolarDARN l-o-s velocities by considering the index of refraction effect.

Since in our work we deal with specific CLY and RKN beams, we consider RISR electron density in beams that reasonably match the HF measurement directions. In the world-day RISR mode, these are RISR beam 8 for CLY observations and beam 3 for RKN observations, Figure 3.1. The electron density profiles in these beams have been processed by Mr. Clayton Graff, an undergraduate student at the U of Saskatchewan (summer of 2017), and provided to the author of this thesis. For the HF velocity correction, we adopted the maximum electron density in the F region profile. This is an acceptable practice in recent comparisons [Gillies et al., 2010; Koustov et al., 2016; Gillies et al., 2018].

Figure 3.9 presents scatter plots of CLY and RKN velocities versus RISR velocity. The datasets here are reduced ones for both radars. This is because we dropped from each overall dataset a number of days for which the slope of the best fit lines was below 0.3-0.4 due to significant presence of low-velocity echoes; these very well might be associated with ground-scatter contamination as will be further discussed in Section 3.9.2. Additionally, many of these events had a significant amount of points with opposite polarity of the velocities. This is an indicator that the radars sensed quite different areas in space, and their comparison does not make sense. Events that have been removed from consideration at this stage for the CLY-RISR case are marked by grey coloring of the cells in Table 3.1.

The plots of Figure 3.9 look very similar to the corresponding plots in Figures 3.6a and 3.7a except the data spread is reduced, and the slope of the linear fit line is much closer to 1. Both these features were expected. We again assessed the plots by applying the linear fit line to the HF velocity medians in 100-m/s bins of RISR velocity, but now considered the range of almost linear dependence, between -500 and +500 m/s of RISR velocity. The slopes of the best-fit line improved here, from 0.51 (CLY) and 0.38 (RKN) to 0.75 (CLY) and 0.74 (RKN), respectively. This improvement is consistent with previous studies except the slopes are not very close to 1. Our reasoning for the effect will be given in Section 3.8.

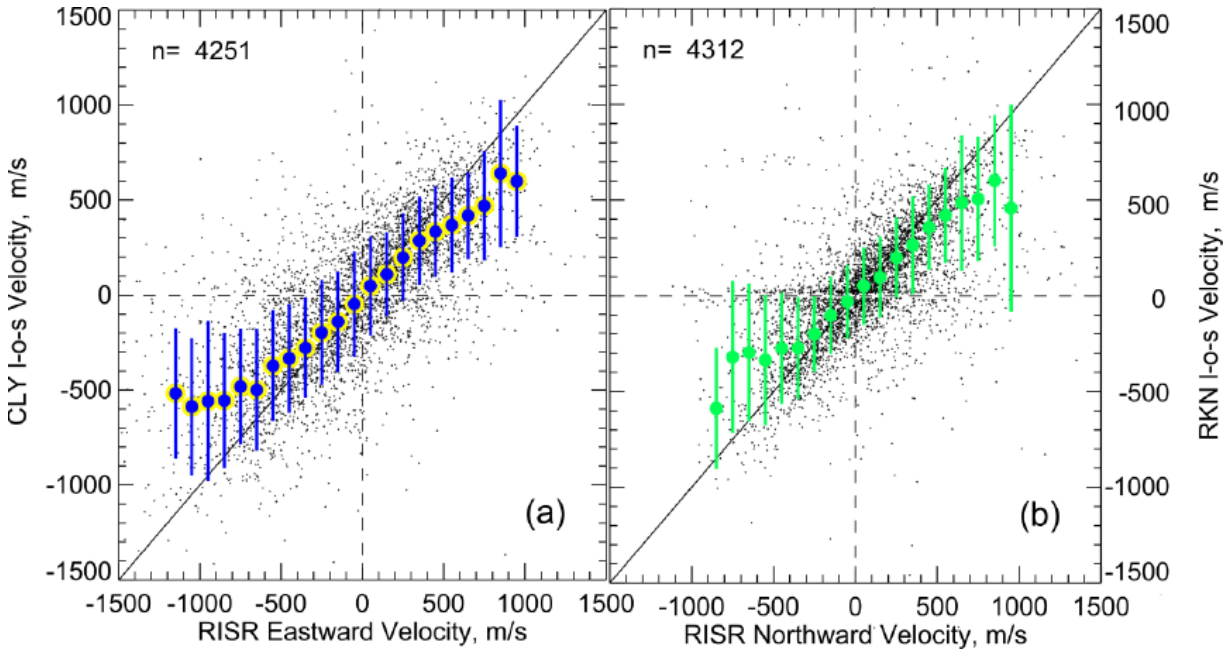

Figure 3.9: (a) Scatterplot of the Clyde River (CLY) l-o-s velocity versus the $\mathbf{E\times B}$ Eastward velocity component as measured by RISR. The total number of points *n* is shown in the top left corner. The blue dots enclosed by yellow circles are medians of the CLY velocity in 100-m/s bins of RISR measurements. The blue vertical lines are the standard deviations of the CLY velocity in each bin. (b) The same as (a) but for the RKN measurements.

3.8 Does the HF velocity underestimation depend on the $\mathbf{E\times B}$ magnitude?

Our analysis in the previous section showed that the index of refraction effect affects the interpretation of velocities measured by the CLY and RKN radars, in line with previous studies. To further investigate the role of this effect, we used an approach first undertaken by Koustov et al. [2016] who considered the velocity ratio $R = Vel_{HF}/Vel_{RISR}$. The issue to look at is whether there

is any trend in *R* values depending on the $\mathbf{E}\times\mathbf{B}$ magnitude. Koustov et al. [2016] noticed that the velocity ratio *R* is smaller at the largest $\mathbf{E}\times\mathbf{B}$ drifts, even after the index of refraction correction has been made. Such an HF velocity decrease was observed by Xu et al. [2001]. Data of Gillies et al. [2018] showed a similar effect, although it was not discussed in the paper. The data in our Figure 3.6 suggests that this trend exists as well, but a more refined analysis is required.

Figure 3.10 shows the velocity ratio *R* for the CLY radar as a binned color plot. While producing this diagram, each CLY velocity was corrected for the index of refraction effect. One dominating feature of the data is R being close to 1 for negative RISR velocities. Contrary to this, R values are clustered around 0.8 for positive RISR velocities in a wide range of velocities between 300 and 700 m/s. The data also show that at larger velocities, R becomes progressively smaller. To indicate this trend more explicitly, we placed in Figure 3.10 the median values for R values in 100-m/s bins of the RISR velocity.

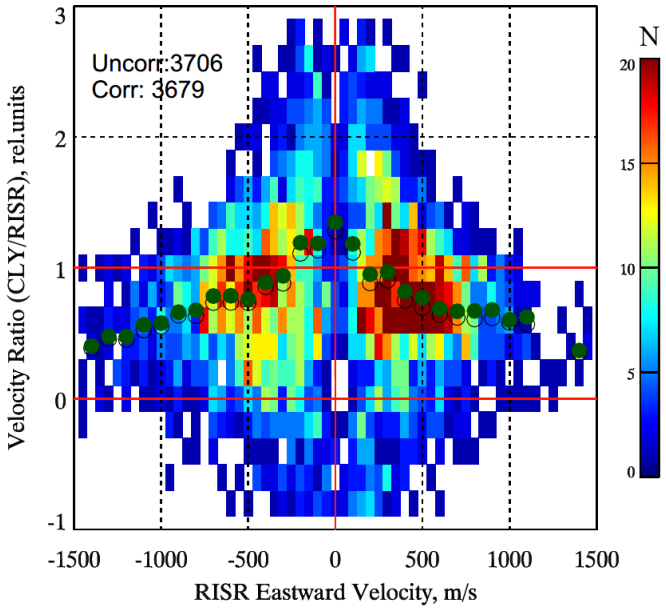

Figure 3.10: Plot for the ratio $R = Vel_{HF}/Vel_{RISR}$ (with HF velocities being corrected for the index of refraction effect) as a function of RISR velocity for reduced data set considered in Figure 3.9a. Green open circles indicate median ratios in 100-m/s bins of the RISR velocity (only measurements with $0 \le R \le 3$ were considered so that the number of points here is smaller than that in Figure 3.9a). Closed circles indicate median ratios for the case of the CLY velocity being corrected for the index of refraction effect (the number of points is slightly smaller in this case, as indicated in the top left corner). The color bar indicate the number of measurements (N).

For completeness, we showed R medians for the case of no corrections being applied to CLY velocities. The solid dots plotted show that the corrected *R* values are close to 1 in a broad range of RISR velocity, between -500 to +500 m/s, but at larger velocity magnitudes >700 m/s, the ratio goes down. The amount of such points is not large, but they are significant and the trend cannot be ignored. We also comment that *R* values are much closer to 1 at small RISR velocity magnitudes. This is mostly owing to an increase in the occurrence of points with $R>1$ at smaller RISR magnitudes. Comparing ratio medians for the cases of index of refraction corrected and uncorrected data, Figure 3.10 confirms, once again, that the index of refraction effect is an important factor decreasing velocity reported by HF radars but, on the other hand, the effect does not change the data dramatically implying that it is not the only factor that affects the HF velocity.

3.9 Discussion of reasons for occasional strong SuperDARN-RISR disagreements

Disagreements in measurements of the plasma flow by HF and RISR radars may be attributed to some factors. Here we discuss three effects. Number one is, now classical, the effect of the index of refraction on the HF velocity in SuperDARN measurements. The second effect is potential ground scatter contamination or misidentification of ionospheric HF echoes, and the third one is the effect of non-uniformity of ionospheric flows.

3.9.1 Does the HF velocity underestimation depend on the time of the day?

To investigate the role of the index of refraction effect, Gillies et al. [2018] plotted the velocity ratio *R* (for the RKN radar) against UT time. The idea was that the HF velocity decrease due to the index of refraction effect should be strongest whenever the electron density in the scattering regions is highest. For the winter/equinoctial ionosphere over Resolute Bay, the largest densities are regularly observed at near local noon and in the afternoon hours (18-22 UT) (e.g., Ghezelbash et al., [2014]). It is therefore expected that the velocity ratio *R* would be smallest at near noon/afternoon hours. This was exactly what has been found by Gillies et al. [2018] for the RKN radar. To assess whether this is the case for CLY measurements, we consider here ratios *R* as a function of time.

As shown in Figure 3.10, ratios *R* vary significantly, from unexpected large values of well above 1, to less than 1, and even unexpected negative values. This implies that the ratio can only

be assessed in a statistical sense. Figure 3.11 gives examples of the histogram distribution of ratio *R* for the CLY-RISR observations in one-hour periods, with one histogram for the nighttime and one histogram for the daytime. According to Figure 3.11, the distributions for nighttime and daytime conditions are very similar except that the daytime data have more points involved and the maximum is more pronounced. The range of the velocity ratio *R* is mostly from -2.0 to 2.0. We assessed the distribution by computing the average-weighted and median values; the values obtained seem to be close to one another all the time. The weighted-average distribution is less than 0.4 for the nighttime (a) and close to 0.8 for the daytime (b).

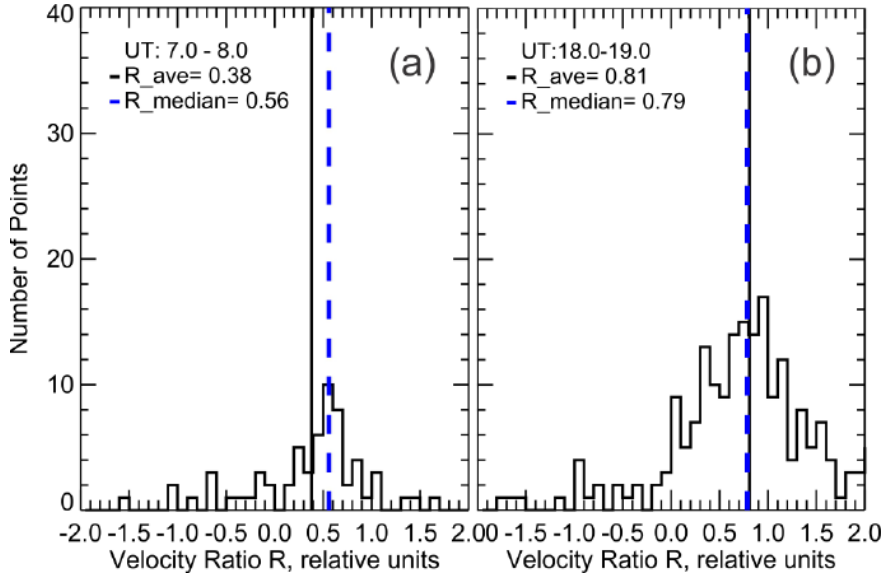

Figure 3.11: Histogram distribution of the ratio *R*, the CLY to RISR velocity, for (a) nighttime (7-8 UT) and (b) daytime (18-19 UT). Data in all joint RISR-CLY events in 2016 were considered. The black vertical line and blue dash line are the average-weighted (R_ave) and median (R_median) of the velocity ratio distribution, respectively. Their values are shown in the top left corner of both plots.

In Figure 3.12, we show how the ratio *R* changes versus time for the day (the HF velocity was corrected here for the index of refraction effect). We report here hourly values of median ratios *R*, similarly to Gillies et al. [2018]. The general trends for the radars are somewhat different. For CLY, the ratio is smaller during nighttime (midnight is at about 07:00 UT) and larger during daytime (noon is at about 19:00 UT). The RKN data show two distinct decreases at 4 and 10 UT. One can say that there are 2 local enhancements in the RKN data, at near late-afternoon hours and at near midnight hours.

The diurnal trend for CLY in Figure 3.12 contradicts the expectation that the index of refraction fully controls the effect of velocity underestimation in HF radar measurements. The RKN data also do not show visible daytime enhancement, contrary to Gillies et al. [2018]. We hypothesize that inconsistency with their data could be because we use here merged RISR velocity data.

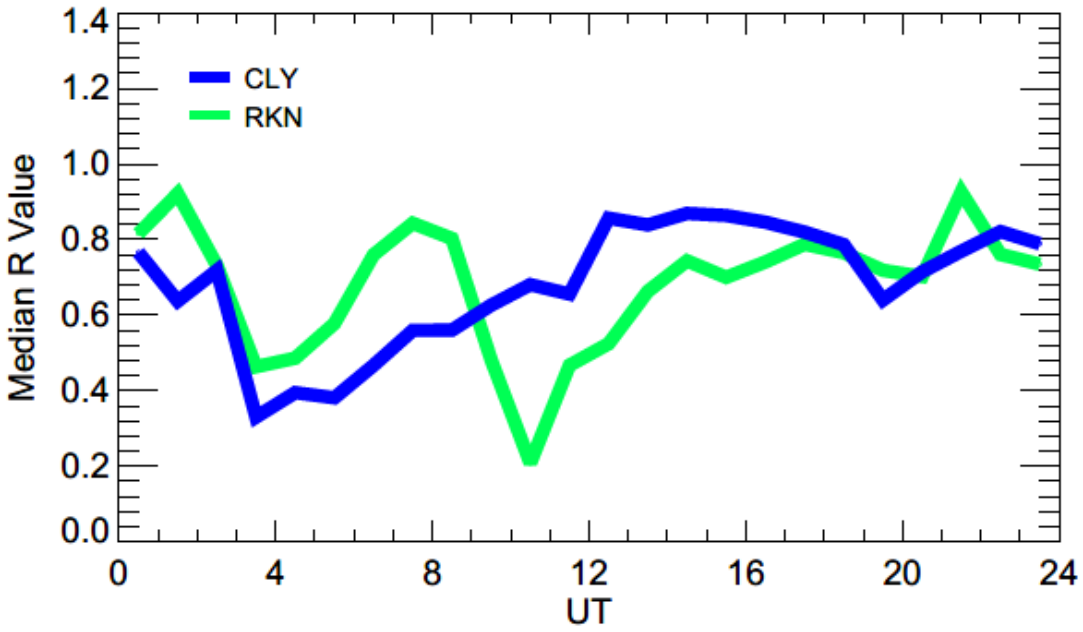

Figure 3.12: Line plot of the hourly median velocity ratio *R* versus UT for the Clyde River (CLY) and Rankin Inlet (RKN) radars. The data sets are the same as for Figure 3.9a, b.

The absence of clear daytime velocity underestimation effect suggests that other factors are likely to affect the CLY-RISR comparison as well, especially for the CLY radar. We hypothesize that HF velocity measurements are biased for observations in the midnight sector. As earlier noted, the flows here can be highly patchy with occasional occurrence of regions with enhanced flow magnitude (low electron density) and decreased flow magnitude (high electron density). We argue that in a case of a patchy ionosphere, there is a good chance that the ratio *R* would be smaller as compared to the case of a uniform ionosphere and homogeneous flow. Flow enhancements/decreases affect both RISR and HF measurements, but in a profoundly different manner. RISR radar would average the velocity in patches with enhanced and depleted electron density, and it would report what can be classified as the "background" flow velocity. In the presence of electron density patches with enhanced and decreased $\mathbf{E}\times\mathbf{B}$ flows, HF radars would automatically detect stronger signals from those areas where the electron density is enhanced, and

the electric field (flow magnitude) is decreased so that it would show somewhat smaller velocity than the background value measured by an incoherent scatter radar. The effect has been discussed by Uspensky et al. [1989].

3.9.2 PolarDARN measurements in the presence of ground scatter

Low HF velocities with magnitudes under 100 m/s can be associated with the occurrence of mixed signals containing ionospheric and ground scatter echoes [Ponomarenko et al., 2007], or sometimes simply misidentified ground scatter. To give an example of such an event, we present here data of RKN observations on 04 March 2016, Figure 3.13a. Here we show, by black diamonds, the original raw values of the RKN velocity in beams 5-7 and gates 20-22 considered in the RKN-RISR comparisons of Figure 3.7. The large blue open circles are the medians of the velocity in 5-min bins of measurements, which were close to the 5-min intervals of RISR observations. These are the values that have been used for producing Figures 3.7 and 3.9. The strip of red vertical bars show the occurrence of ground scatter detection by the RKN radar in the same beams and gates. In this event, ground scatter occurred all the time, see the red vertical bars, but at certain different times (for each gate the radar reports either ionospheric or ground scatter signal), the radar reports occurrence of ionospheric echoes with low velocity. It is very likely the echoes were ground scatter. This situation occurred in some other periods of our joint RISR-PolarDARN database.

Something different happened for CLY observations 2 hours earlier in the same event. Figure 3.13b shows CLY data for a 2-hour period, 1700-1900 UT. This is a shortened period of data presented in Figure 3.3. Here again, the large blue open circles are the medians of the CLY velocity in 5-min bins of measurements matched to 5-min intervals of RISR observations. These are the values that have been used for Figures 3.3, 3.4, 3.6, and 3.7. From 17:00 to 17:30 UT, the blue circles overlap with the majority of the black diamonds at velocities ~ -500 m/s. For these times, the RISR and CLY data agree reasonably well (compare with Figure 3.3). A few low-velocity points exist during this period, but they constitute a small portion of the data. Between 17:30 and 18:15 UT, these two kinds of points exist as well, but the low-velocity points dominate so that the median values are small resulting in significant differences between the CLY 5-min velocity medians and the RISR velocities. If these low-velocity echoes did not occur, the CLY radar would report values close to -500 m/s, which would be in good agreement with the

simultaneous RISR measurements (compare with the data of Figure 3.3). Such low-velocity medians contribute to the cluster of points seen in Figure 3.4 and mentioned in Section 3.4. On the basis of the data presented, we suggest that the low-velocity HF points are misidentified ground scatter. This is consistent with an opinion expressed by Gillies et al. [2018], who investigated joint RKN-RISR data. We note that within the data set considered there are several other days when the effect was very strong, especially for the RKN radar. Further analysis of raw ACF data is needed to confirm our conclusion. This extensive work is left for a future project.

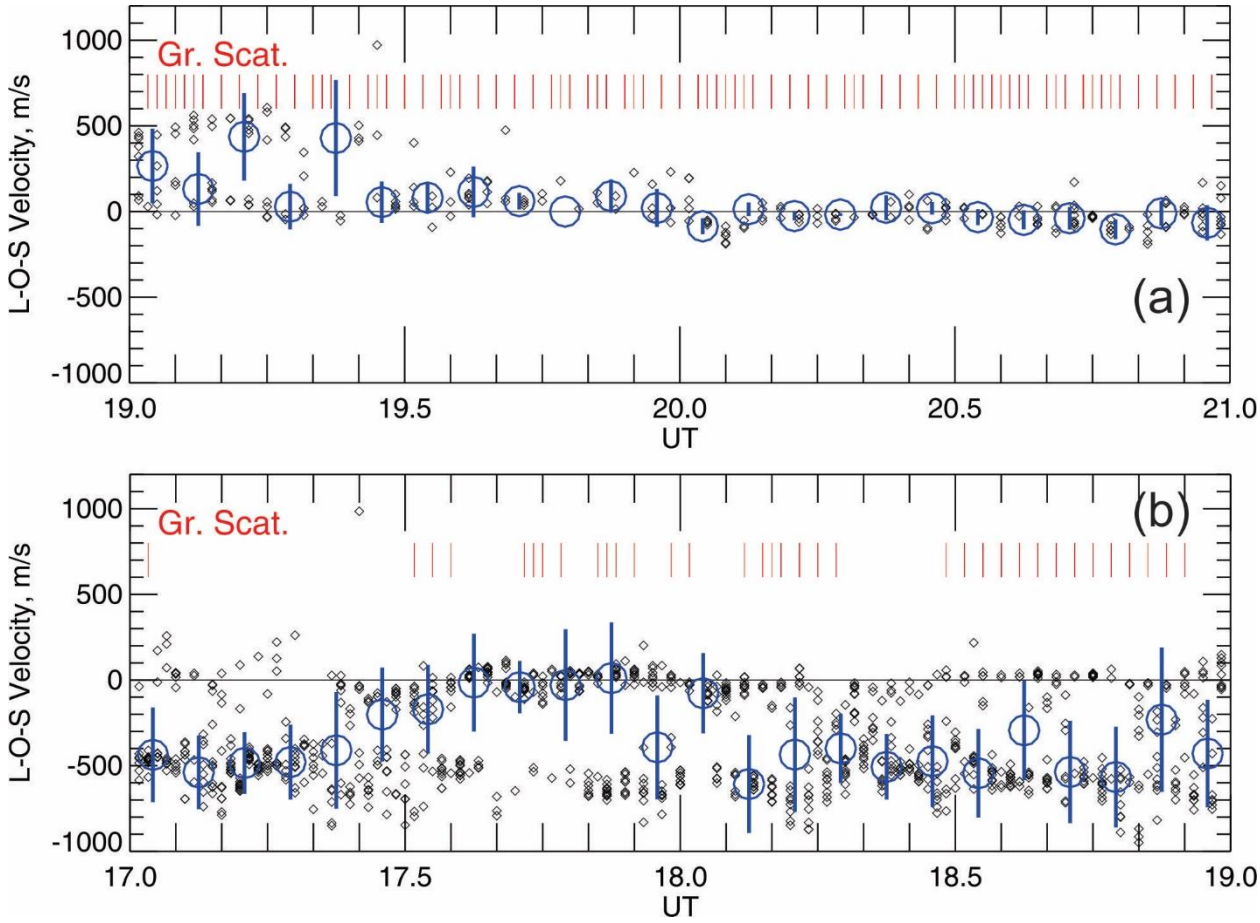

Figure 3.13: Line-of-sight (l-o-s) velocity and ground scatter occurrence versus time for the event of 04 March 2016. (a) Black small diamonds are the Rankin Inlet (RKN) l-o-s velocity as measured in beams 5-7 and gates 20-22. The blue circles and blue vertical lines are the RKN velocity medians and standard deviations in each 5-min of measurements, respectively. The red vertical lines show the occurrence of ground scatter for the RKN observations in the same beams and gates. (b) The same as (a) but for the CLY radar (beams 4-6, gates 18-21) and 2-hour earlier period.

Although the signal misidentification does not happen all the time, the impact on the SuperDARN convection data could be significant.

3.9.3 RISR and SuperDARN observations of sheared flows

Investigating our database, we identified one special situation when the RISR-SuperDARN velocity disagreements were particularly strong. Figure 3.14 gives an example of CLY-RISR observations on 4 March 2016, where RISR and CLY velocities differ consistently by several hundred m/s over a period of almost 2 hours.

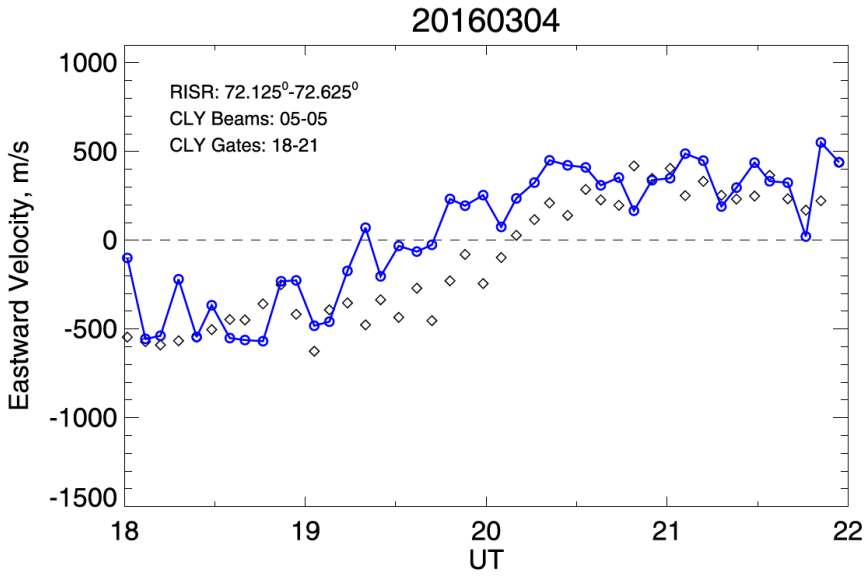

Figure 3.14: (a) Eastward component of the $\mathbf{E \times B}$ drift as measured by RISR (black diamonds, 5-min resolution data) and matched velocity medians of CLY observations (blue circles, 5-min medians of original 1-min measurements in beams/gates "overlapping" the region of RISR observations) for the event of 04 March, 2016.

We also checked the convection maps for this period. Figure 3.15 shows that the RISR-based eastward velocity component changed its sign at about 20 UT (black curve). The CLY l-o-s velocities (blue line) followed RISR velocity temporal variations, but the variability was much larger, especially after 20 UT. The eastward component of the SuperDARN map velocity is shown in Figure 3.15 by the pink line. This line is consistent with both the CLY l-o-s velocity and RISR velocity up until ~ 20 UT, but strong disagreement is seen afterward. Here the SuperDARN map velocity polarity was negative, while the other two quantities were positive. The velocity disagreement between the instruments is seen in Figure 3.15b as a cluster of points in quadrant 4.

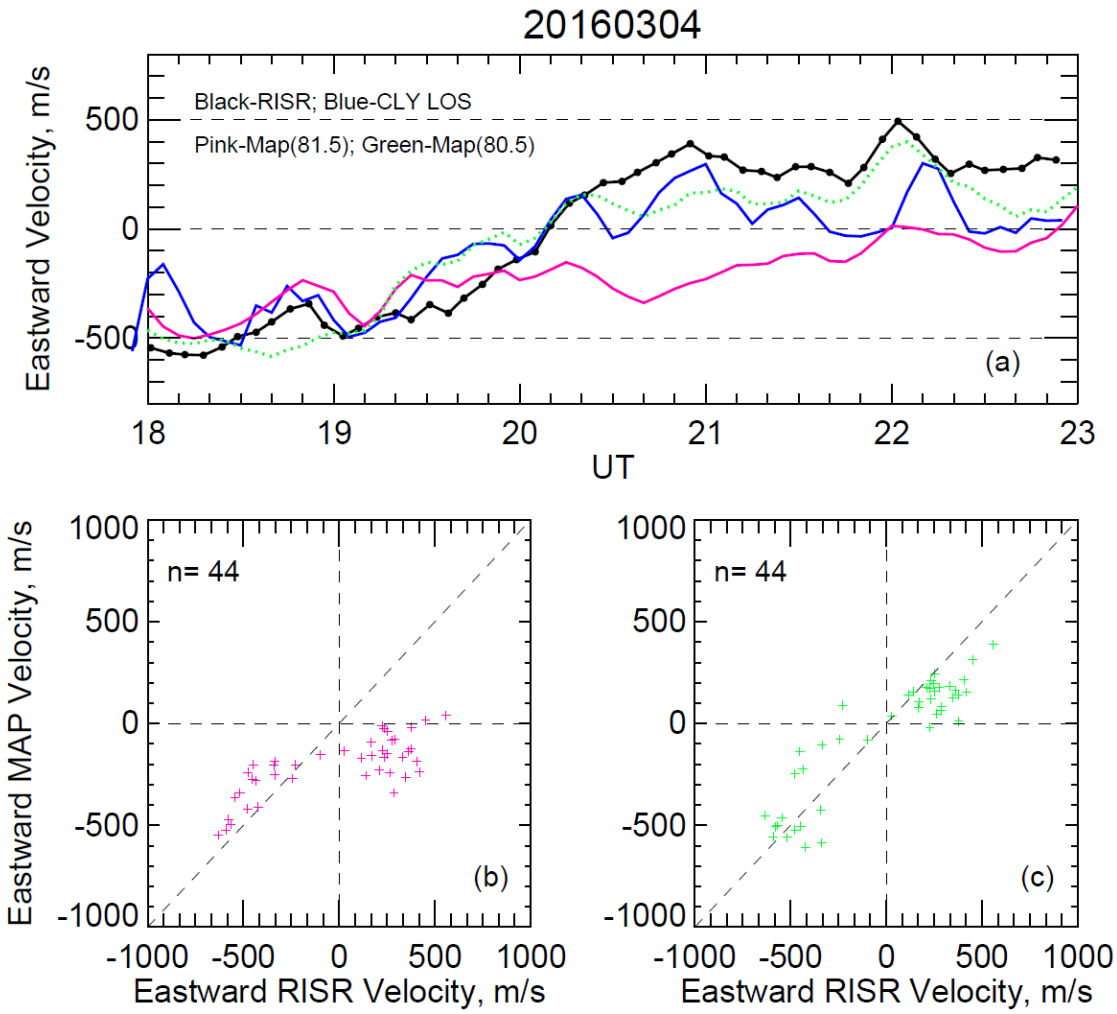

Figure 3.15: (a) Eastward plasma velocity in the area of joint RISR-C – SuperDARN radar observations as measured by the RISR (black), CLY radars (blue) and inferred from SuperDARN 5-min convection maps at MLAT=81.5° (pink) and MLAT=80.5° (green). (b) Scatter plot of nearly coinciding measurements (in time and space) of the eastward plasma velocity by RISR-C and all SuperDARN radars (inferred from 5-min convection maps).

By reviewing the SuperDARN convection maps and CLY velocity scan maps, we realized that the above observations were carried out in the presence of strong sheared flows. Figure 3.16a illustrates, just for one CLY velocity scan, the typical spatial velocity distribution within the radar FoV, for the above event. A sharp change in the l-o-s velocity polarity from positive values in low number beams to negative values in high number beams is noticeable. The polarity transition occurs in the central beams 5-7. Figure 3.16b gives a global-scale map of plasma flow inferred from all SuperDARN measurements. The map has a number of vectors originated from the RKN and INV radar measurements on a top of those from CLY measurements. The presence of highly-

curved flows is obvious in the near noon hours. Under these conditions, both SuperDARN and RISR can have difficulties in the construction of a 2-D vector field.

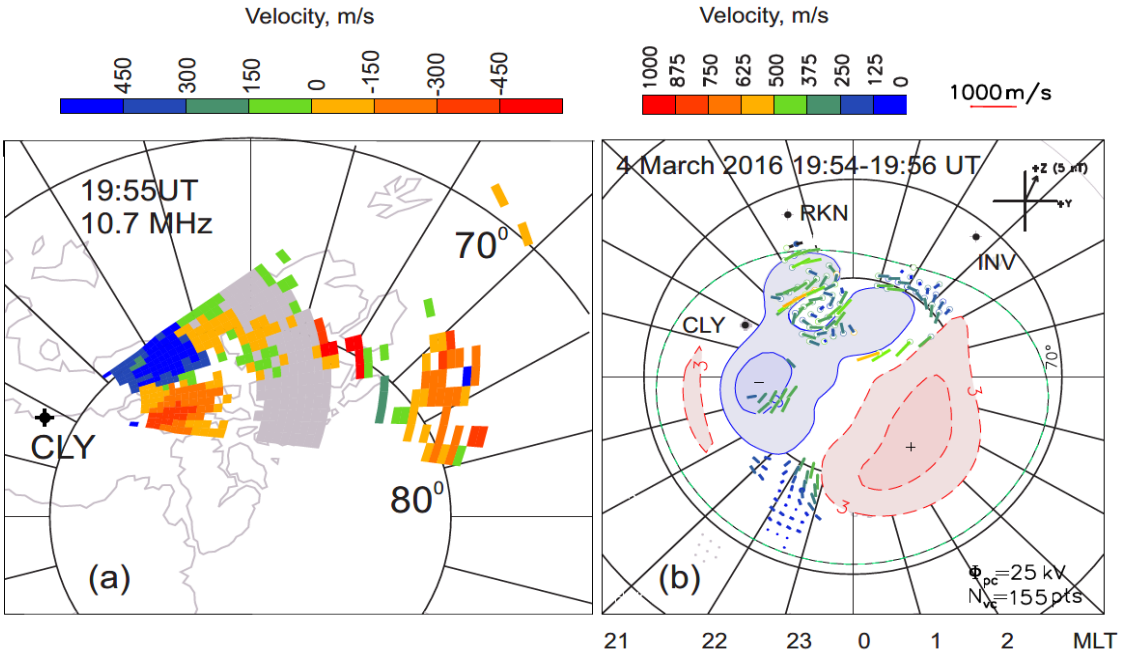

Figure 3.16: (a) A Clyde River (CLY) l-o-s velocity map at 1955 UT on 04 March 2016 and (b) a standard 2-min convection maps inferred from all SuperDARN radar measurements for the same period.

We comment that the flows seen in Figure 3.16 are sunward, roughly along the magnetic meridian at near noon hours, signifying occurrence of a reverse convection cell. This is highly expected since the IMF B_z was steady at about +5 nT starting from 18:30 UT all the way until ~22 UT for this event.

Evaluation of the extent the SuperDARN and RISR vectors are affected by the curvature of the flow is difficult. We realized visually that the centers (foci) of the convection cells, according to RISR and SuperDARN, do not coincide in latitude for many cases in this event. Also, we realized that, while selecting the SuperDARN map data at lower latitudes, the agreement between the RISR and SuperDARN map data improves dramatically. To investigate further, we determined the location of the convection reversal boundary (CRB) for the reverse convection cell (like that shown in Figure 3.16) by considering the standard 2-min SuperDARN maps, CLY velocity-scan maps, and by looking at the reversal in the latitudinal profile of the RISR velocity (these are given for 5-min intervals). The data are presented in Figure 3.17. One feature is visible here: the CRB is located almost 2° higher MLAT for SuperDARN at the beginning of the event, and the differences are

minimal toward the end of the event. Plotted in Figure 3.17 is the CRB location according to solely the CLY velocity-scan maps and it is closer to that inferred from RISR data, suggesting that perhaps the SuperDARN fitting procedure is the major factor for the larger differences between the SuperDARN maps and RISR measurements in this specific event. This is not to say that RISR measurements are completely precise; they are very likely also subject to errors under these strongly-curved flows.

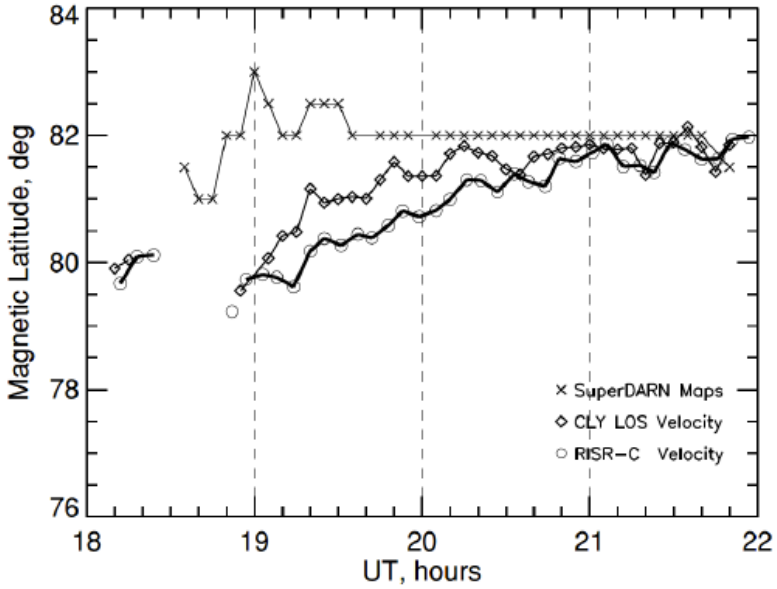

Figure 3.17: Magnetic latitude of the flow reversal location within the dayside reverse convection cell as inferred from SuperDARN convection maps (crosses), CLY l-o-s velocity measurements in various beams (diamonds) and RISR measurements (circles) for the event of 04 March, 2016.

3.10 Conclusions

The analysis undertaken in this chapter allows us to make several conclusions.

1. The CLY radar velocity measured in beams 4-6 is statistically comparable to the $\mathbf{E \times B}$ component of the plasma drift along these beams (azimuthal plasma flows) as measured by the incoherent scatter radar RISR-C. The same conclusions are drawn for the RKN radar measurements of the $\mathbf{E \times B}$ flow component in the meridional direction. This implies that the velocity data provided by these radars are reliable and suitable for convection mapping involving all the SuperDARN radars. The comparisons complement the previous validation work for the RKN and INV radars.

2. The slope of the best linear fit line to the CLY velocity variation versus the $\mathbf{E}\times\mathbf{B}$ component (as measured by RISR) is on the order of 0.5 if all the available data are considered without their scrutiny. Correction of HF velocities by the index of refraction effect and removing data with obvious ground-scatter contamination improves the slope to 0.75. The velocity correction has been done by assuming maximum values of the electron density at the F region peak. The slope of the linear fit line for the corrected data is still below 1 implying that additional factors affect the relationship.

3. The effect of HF velocity underestimation for the CLY radar becomes progressively larger for faster plasma drifts. The effect is evident for velocities above ~ 500-700 m/s. This implies that other factors, on a top of the index of refraction effect, affect HF SuperDARN velocities.

4. It is suggested that one of these additional factors is a bias in HF radar measurements of the velocity because HF radars get stronger signals from ionospheric regions with enhanced electron density where the electric field $\mathbf{E}\times\mathbf{B}$ drift is decreased as compared to the background plasma. This hypothesis is supported by the presented data on the diurnal variation of the HF velocity ratio to the RISR velocity that shows a clear decrease during nighttime and not daytime.

5. Large disagreements between HF and RISR velocity measurements were found for very low CLY and RKN velocities, below 100-200 m/s in magnitude. For many of these periods, the HF radars detect ground scatter echoes in one of the close gates-beams. This implies that some ionospheric echoes could be misidentified by the FITACF technique. This effect is more pronounced for the RKN radar.

6. In a case of highly-curved/distorted plasma flows, such as near dayside reversed convection flows occurring under strong IMF $B_z > 0$, the differences between RISR and SuperDARN velocity vectors can be large. One of the reasons for disagreement is a minor error in locating the center of the convection cell while performing the fitting procedure. Data for one such event were presented, but how widespread the effect is needs to be seen.

7. Reasonable agreement between the velocities of the two systems implies that the RISR technique of the $\mathbf{E}\times\mathbf{B}$ derivation from individual radar beams is a reliable method most of the time. It is expected that the method is less reliable in the midnight sector, where the flows are often very irregular, and strong vertical motions occur. It is symptomatic that the agreement between the velocities measured by the instruments was worst during nighttime.

CHAPTER 4

CONSISTENCY OF VELOCITY MEASUREMENTS BY THE CLYDE RIVER AND INUVIK RADARS

Comparisons of the SuperDARN l-o-s velocities with measurements of other independent instruments is an important step in assessing HF coherent radars as instruments for plasma flow measurements. As we described in Section 2.3, this is ongoing work within the SuperDARN community, and our results of Chapter 3 is another contribution in this area. Not less important, however, is assessing self-consistency of velocities measured by various SuperDARN radars. This can be done in at least two ways.

One way is to compare data for two radars looking in just about opposite directions. This is a unique geometry available for several SuperDARN pairs. In this case, velocities are expected to be different in the polarity only. Koustov et al. [2014] presented this kind of plot for the Southern Hemisphere Dome C and McMurdo observations. The data were obtained at range gates 10 for both radars. These are not typical ranges of SuperDARN F region measurements, and comparisons at farther ranges are essential.

The second way of assessing the consistency of SuperDARN velocity measurements is to consider a case of echo detection with three radars in a "common" area of observations. In this case, the l-o-s velocities can be merged into full vectors by pairing data from 2 or 3 radars. Such work had been undertaken for VHF radars [Nielsen et al., 1983]. So far there has not been such an attempt for SuperDARN. In this chapter, we investigate the PolarDARN velocity data consistency confirmation using both methods.

4.1 Geometry of PolarDARN radar observations and methodology of the velocity comparison

Figure 4.1 shows the details of the geometry of PolarDARN radar observations. The Clyde River (CLY) and Inuvik (INV) radars have their fields of view (FoVs) oriented toward each other with significant overlap. We show here, by color, the centers of two radar beams that will be of interest for this study. These are RKN beam 2 and INV beam 15. The beams intersect each other at range

gates ~23. Three gates for each radar are indicated in Figure 4.1 by short arc segments. The common INV-RKN observational zone also overlaps with the CLY radar FoV. For the CLY radar, the beam of interest to us is beam 5. Its center-line is not shown in Figure 4.1, but blue open circles indicate centers of several of its range gates. Several INV radar cells in beam 15 co-locate with several radar cells of the CLY radar, and the direction of the respective beams is almost opposite. This unique geometry of the INV and CLY radars allows us to assess the consistency of the velocities they measure using the first approach stated above. It is important that the CLY and INV ranges to the region of the comparison be about the same; for this reason, we will term the comparison at this point the "symmetry point." For the symmetry point, we adopt the central radar gate to be 23 for CLY and 25 for INV. The central gate for the RKN radar is 23, see Figure 4.1.

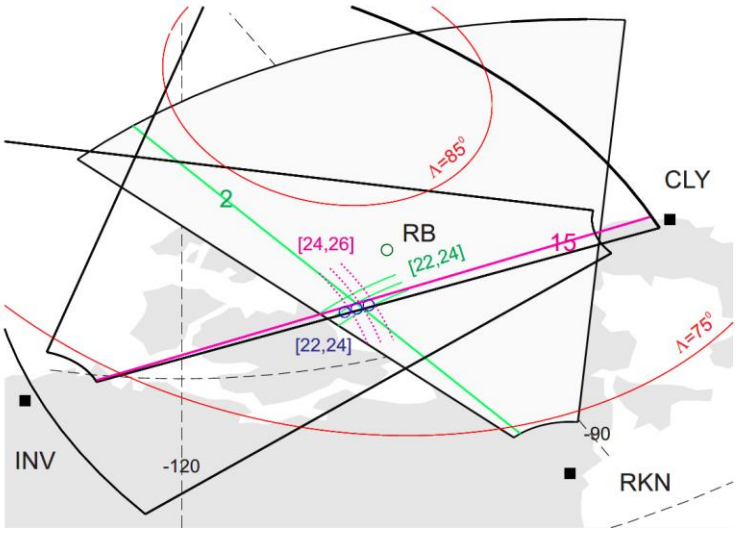

Figure 4.1: Fields of view of the Inuvik (INV), Clyde River (CLY) and Rankin Inlet (RKN) PolarDARN radars near the Resolute Bay (RB) zenith, for range gates 5-50. Pink and green straight lines show the centers of beams 15 and 2 for the INV and RKN radars, respectively. Dashed lines are range marks for the centers of the range gates considered ([24,26] for INV and [22,24] for RKN). Blue circles are centers of the Clyde River range gates [22,24] for its beam 5. The red contour lines are for MLAT= $75°$ and $85°$.

The second type of comparison was done by considering velocity measurements by the INV-RKN pair and the CLY-RKN pair. We cannot use the CLY-INV pair as the directions of observations nearly coincide. The goal of this comparison was to assess what kind of error one might encounter while merging the velocity data at beam crossings. Although the merge technique is rarely used in modern SuperDARN research, it is the general opinion that in an area with good echo coverage, the two methods, the merge technique and the Potential FIT technique, produce vectors of about

the same magnitude and direction. With this consideration of investigating the consistency of merge vectors, one can estimate the magnitude of possible uncertainty in the Potential FIT technique.

For both types of comparisons, data from the CLY, RKN and INV radars for the entire year 2016 were considered. All comparisons were performed by computing PolarDARN velocity median values in 3 range gates and one beam. We first examined the consistency of the velocity measurements between the CLY and INV co-aligned beams for measurements in cells with about equal separation from the radars (gates [24,26] for INV and [22,24] for CLY). We then investigated the degree of velocity agreement between the instruments for observations close to either the INV or CLY radar locations. In this case, we considered data in range gates [14,16] for INV and [32,34] for CLY in the first case, and then in gates [34,36] for INV and [12,14] for CLY. Data for operating frequencies bands of 10 MHz and 12 MHz are considered separately. This was to avoid the necessity to correct the measured velocity for the index of refraction effect, as discussed and presented in Chapters 2 and 3. At each frequency band, we considered every 5-min period of measurements and found the median value of the velocities that were usually given for each 1-min interval. We then plotted median CLY l-o-s velocity versus median INV l-o-s velocity for each event and, ultimately, produce a combined plot that covered the entire year 2016. This final product is presented in Figure 4.2.

4.2 Results of the l-o-s comparison

Figures 4.2a and 4.2b show that most of the points under consideration are located near the bisector of perfect agreement. This holds both for positive and negative velocities, in the range of +/- 1000 m/s. Thus, the available data cover the entire range of typical l-o-s PolarDARN velocities. The number of points is ~15,000 for the comparison at 10 MHz and ~10,000 for the comparison at 12 MHz. This is a significant database. No clear tendency can be inferred by eye inspection of Figures 4.2a,b; the clouds of points are symmetric with respect to the bisector of perfect agreement. The cloud is more widespread for the comparison at 10 MHz, but the data consistency looks as being comparable at 10 and 12 MHz. In the past, e.g., Gillies et al. [2018], special attention had been paid to measurements close to 400 m/s as this is the ion-acoustic speed and suspicions were that some SuperDARN echoes are coming from the E region. In a case of Figure 4.2a,b, no evidence

for such a feature can be found. Moreover, at 12 MHz both radars show very consistent velocity magnitudes close to 500 m/s.

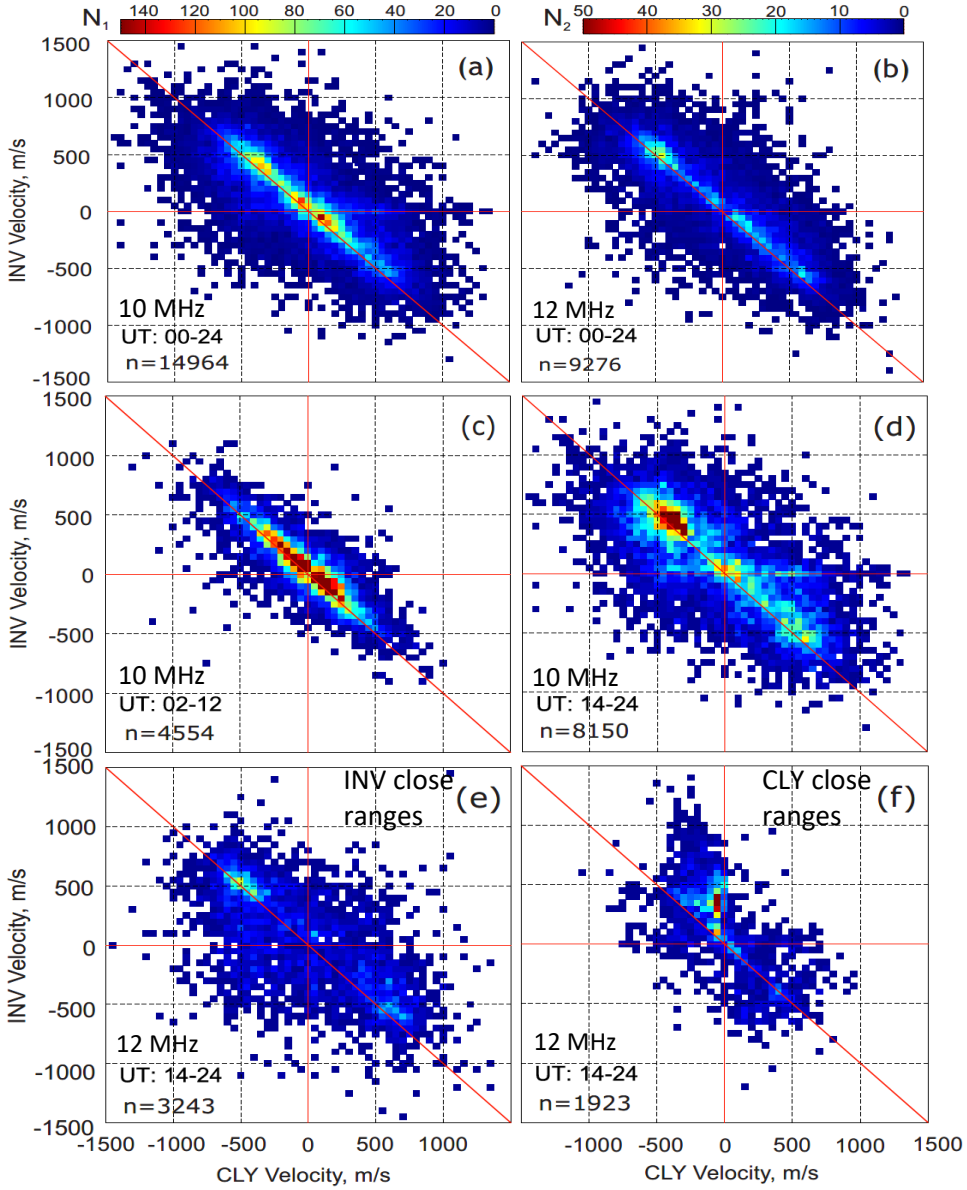

Figure 4.2: Color-coded plots of the Inuvik (INV) radar l-o-s velocity versus the Clyde River (CLY) radar l-o-s velocity (median values) in nearly coinciding beams (beam 15 for INV and beam 5 for CLY) for observations in the entire 2016. (a) Data at ranges of about equal separation (gates [24,26] for INV and [22,24] for CLY) at the radar operating frequency of 10 MHz for both radars. (b) The same as (a) but for the radar operating frequency of 12 MHz. (c) and (d) The same as (a) but for nighttime (02-12 UT) and daytime (14-24 UT), respectively. (e) Data at ranges close to INV (gates [14,16] for INV and [32,34] for CLY) at the radar operating frequency of 12 MHz for both radars (f) The same as (e) but for ranges close to CLY (gates [34,36] for INV and [12,14] for CLY). Colorbar for number of measurements N_1 applies to panels (a) and (b) while color bar for number of measurements N_2 applies to panels (c) through (f).

Figures 4.2c and 4.2d present the 10-MHz data that are split according to the nighttime and daytime periods of measurements. One reason for such consideration is that, according to our results in Chapter 3, the velocity agreement is different during daytime and nighttime. If the reason for disagreements in the RISR-CLY comparison of Chapter 3 is only owing to the index of refraction effect, then in the INV-CLY velocity comparison of this chapter, the differences should not exist because the index of refraction effect works for both HF radars involved. In the case of significant differences found, one might think that different propagation conditions are responsible for having different velocities, both for this comparison and that of Chapter 3.

Figure 4.2c shows that nighttime data from the radars are well clustered around the bisector of perfect agreement, while the daytime data are more spread about the bisector. In fact, only a small cluster of points around 500 m/s for INV(-500 m/s for CLY) is seen. The worse consistency of the measurements during daytime is also evident from the size of the cloud of points in Figures 4.2c and 4.2d. One may conclude that perhaps propagation conditions affect the velocities measured, for example through noticeable lateral deviations of the radar beams.

Figures 4.2e and 4.2f show velocity comparisons for observations closer to INV and CLY radar locations (along the co-aligned beams 15 and 5), respectively. The radar frequency is 12 MHz, and only daytime data are considered. The objective here was to consider worst case conditions for the F region echo detection close to either of the INV or CLY radars. In the daytime ionosphere, the electron density is high enough in the both F and E regions so that the radars have a chance to receive echoes from both of these regions. As we mentioned in Chapter 1, Section 1.4, the E region echo velocity can be at the ion-acoustic speed of ~ 400 m/s. Gates 12-14 correspond to ranges where simultaneous echo detection from F and E regions can be expected.

One can see that for the location close to INV, Figure 4.2e, the scatter plot is similar to that of the symmetry point in Figure 4.2d, except being somewhat more round. For the location close to CLY, Figure 4.2f, the cloud of points is not symmetric. One can notice a significant amount of points in quatdrant 2 that are located well above the bisector implying that the CLY velocity magnitudes are below the INV velocity magnitudes. We interpret this result as an indication that while the INV radar detects F region echoes, the CLY radar detects many echoes from the E region with velocity magnitudes well below the $\mathbf{E}\times\mathbf{B}$ l-o-s component. This result implies that the far range gate for the E region echoes, that is traditionally considered to be 10 (e.g., Makarevich [2008]), can be actually 15 or even larger for the CLY radar.

4.3 Results of the merge velocity comparison

Figure 4.3 explains the concept of our merge velocity comparison. Here we show the l-o-s velocity measured by the INV radar as a blue vector, the l-o-s velocity measured by the RKN radar as a black vector, to form the merged vector $\mathbf{V}_{\text{rkn-inv}}$ represented as a large blue vector. Similarly, by combining l-o-s velocities of the RKN-CLY pair, another merge velocity vector is obtained $\mathbf{V}_{\text{rkn-cly}}$ (large red vector). Our objective was to estimate the difference in the merged velocity magnitudes and azimuths. We computed the merged velocity vectors and their orientation using the equations described in Section 2.1.5. The vectors' azimuths were referenced from the direction of the RKN radar beam.

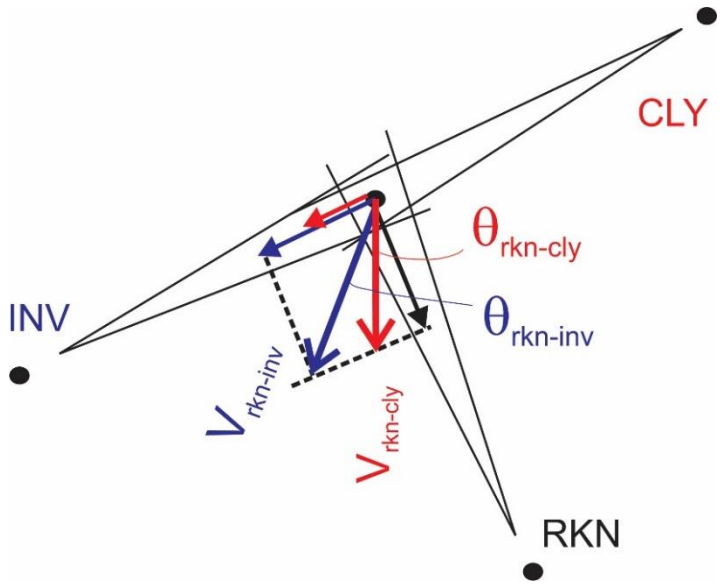

Figure 4.3: A cartoon explaining the geometry for Inuvik (INV), Clyde River (CLY) and Rankin Inlet (RKN) PolarDARN radar measurements in beams and gates selected for the comparison. $\mathbf{V}_{\text{rkn-inv}}$ is the merged velocity vector inferred from RKN and INV l-o-s velocities. $\mathbf{V}_{\text{rkn-cly}}$ is the merged velocity vector inferred from RKN and CLY l-o-s velocities. $\theta_{\text{rkn-cly}}$ and $\theta_{\text{rkn-inv}}$ are the orientation of merged velocity vectors inferred from two independent pairs of radars. Angle θ is referenced from the direction of RKN observations.

Figure 4.4a plots the merged velocity vector magnitude for the $\mathbf{V}_{\text{rkn-inv}}$ pair versus the merged velocity vector magnitude for the $\mathbf{V}_{\text{rkn-cly}}$ pair. Reasonably good correlation for velocity magnitudes is seen. We assess the merged velocity magnitude difference in 2 ways. First, we

produce histogram plots for the difference in the magnitudes (Figure 4.4b) and second, we produce histogram plots showing the ratio of one merged velocity vectors to the other (Figure 4.4c). We also present a histogram distribution of the difference in the direction of merged velocity vectors (Figure 4.4d). We then apply a Gaussian fit to the histogram plots to estimate the mean and width of the distributions quantitatively.

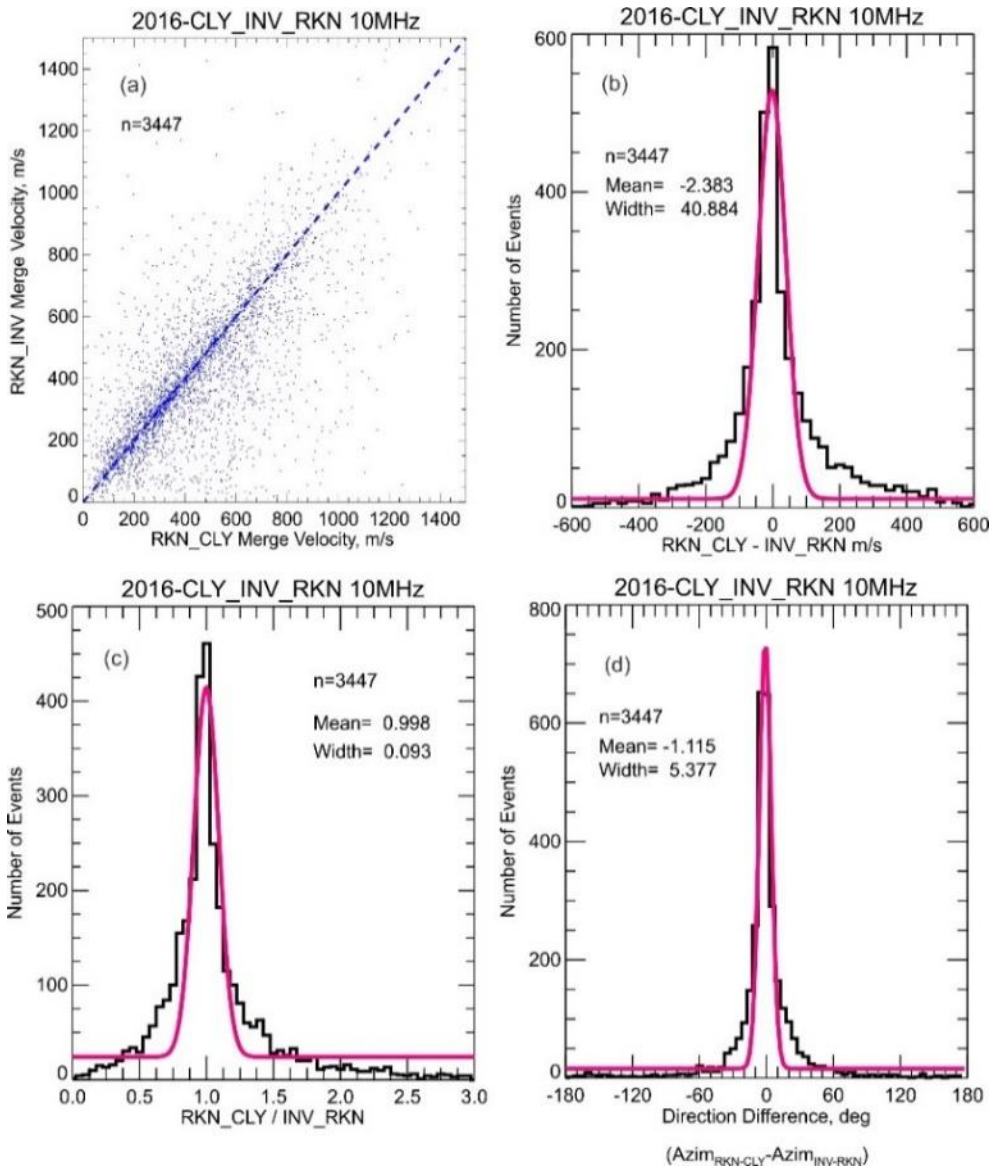

Figure 4.4: (a) A scatterplot of the RKN-INV merged velocity vector magnitude versus RKN-CLY merged velocity vector magnitude. Total number of points *n* is shown in the top left corner. Histogram distribution of the (b) magnitude difference between the merged vector pairs, (c) ratio of the merged vector pairs and (d) azimuth difference between the merged vector pairs. The pink curve represents the Gaussian fit to the respective histograms. The mean and width of the distributions are shown on each histogram plot.

Table 4.1 below presents a summary of the mean values obtained from the Gaussian fit for different frequencies and time sectors, 00:00–24:00 UT (All day), 02:00–12:00 UT (Nighttime sector) and 14:00–24:00 UT (Daytime sector). The velocity magnitude difference is close to zero in all cases, statistically speaking, but it can be as large as $\pm 40.9/2$ m/s, according to the width of the distribution. The velocity ratio for all cases considered is close to one, which is not a surprise from the data of Figures 4.2a,b. The difference in the azimuths of vectors is not large, statistically on order $\sim 1^\circ$, but deviations could be up to $\pm 5.37^\circ/2$, according to the width of the distributions.

Table 4.1: Mean of magnitude difference and azimuthal difference between the merged velocity vector pairs for the PolarDARN.

Mean	All data (10 MHz)	All data (12 MHz)	Nighttime (10 MHz)	Daytime (10 MHz)	CLY (10 MHz)
Magn. diff. (m/s)	-2.383	-3.698	-2.381	4.371	19.525
Width (m/s)	40.884	55.160	26.714	113.065	85.082
Velocity ratio	0.998	0.992	0.999	0.985	1.003
Azim. Diff. ($^\circ$)	-1.115	-0.632	-1.637	-0.684	-0.606
Width ($^\circ$)	5.377	6.422	5.780	5.251	3.920

Statiscally speaking, the results of the merge velocity comparison for the symmetry point of observations strongly supports the notion that the PolarDARN radar velocities are reasonably consistent with each other and they accurately characterize the $\mathbf{E}\times\mathbf{B}$ plasma flow.

We also performed a comparison of merged velocities for the case of observations in the region close to the CLY radar where we found that the CLY-INV velocity agreement is not very good, Figure 4.2f. To accomplish this, we repeated the entire process of obtaining full velocity vectors we described above, but this time with different radar beams/gates: CLY– beam 5, gates [12,14]; INV – beam 15, gates [34,36 and RKN beam 9 gates [21,23]. In this case, the mean merge velocity difference is about 20 m/s and the width of the distribution is larger at ~85 m/s. The difference in the azimuths of the vectors is also larger in this case, -0.6°. Although these results imply deterioration in the merged vector consistency, the effect is not very strong.

4.4 Conclusions

Both comparisons showed that the CLY velocity is statistically consistent with measurements of each of the complementary instruments. For the comparison involving three radars, the mean values obtained from estimating the differences in both magnitude and azimuth between the two merged velocity vectors was reasonably small, and this points to a conclusion that all three radars measure velocities accurately amongst themselves. This was also evident from the mean values (close to 1) we obtained for the ratio of the merged velocity vectors.

CHAPTER 5

AZIMUTHAL PLASMA FLOWS IN THE POLAR CAP AS SEEN BY THE CLYDE RIVER RADAR

5.1 Introduction

Plasma flow patterns in the high latitude ionosphere are the subject of many studies, as outlined in Chapter 1. This work has resulted in establishing major flow configurations for quasi-steady states of the magnetosphere-ionosphere system. These patterns, in general, have been attributed to a number of magnetospheric processes (Chapter 1). However, there are numerous details of the patterns that are not well described and not well understood. Here we undertake a modest attempt to clarify one aspect of convection patterns, namely the seasonal changes in the patterns for southward orientation of the Interplanetary Magnetic Field (IMF) $B_z < 0$.

The literature on this topic is very limited because not much experimental data have been available so far. This lack of data is not a surprise because addressing this issue on the long-term with continuous measurements on a global scale is required. Prior to the introduction of SuperDARN, this task was addressed with minimal data sets obtained through satellite missions [Rich and Hairston, 1994; Förster et al., 2007, Haaland et al., 2007] and incoherent scatter radar measurements [de la Beaujardiere et al., 1991]. The original SuperDARN-based model of high-latitude plasma flows, which dominated the research for two decades, the Ruohoniemi and Greenwald [1996] model, did not have any seasonal dependence. The first attempt to infer the seasonal changes on ionospheric plasma flows with SuperDARN by Ruohoniemi and Greenwald [2005] ended up with a slightly negative result. One reported result was that the shape of the potential contours changed slightly toward summer with the high-latitude flows being more "round" for a dusk convection cell (their Figure 8). Some aspects of a publication by de la Beaujardiere et al. [1991] have also been confirmed. These are (1) a shift of the convection contours and the center of the large-scale cells toward the midnight sector in summer, and (2) overall rotation of the convection cells to earlier magnetic longitude (MLT) hours in summer so that the flow "throat" is shifted to earlier MLTs.

In a recent effort to create an improved statistical model of the high-latitude plasma flow patterns based solely on SuperDARN measurements, Cousins and co-authors [Pettigrew et al., 2010; Cousins and Shepherd, 2010] sorted the radar data according to the intensity of an external driver, the solar wind electric field ($\mathbf{E_{sw}}$), as well as in terms of the tilt of the Earth's magnetic dipole. In their model the seasonal changes of the patterns can be assessed, although it is not straightforward as the model instantaneous outputs need to be averaged over seasons. Koustov et al. [2015] undertook another approach. These authors considered monthly averaged convection patterns that were obtained for specific bins of the transverse component of the IMF, $B_T = \sqrt{B_z^2 + B_y^2}$, and by involving gridded velocities at all latitudes. These authors reported noticeable seasonal variations of the polar cap velocity magnitude. Their approach, however, can be questioned because average IMF conditions for individual months are not quite the same, and this might introduce biases.

In this chapter we consider average plasma flow velocities in the azimuthal direction inferred from Clyde River (CLY) radar observations in beams 4-6 and range gates 18-21. These beams and gates cover the area of joint RISR-C and CLY observations that have been investigated in Chapter 3 of this Thesis. Having validated the CLY measurements gives us confidence that the results obtained reflect true seasonal changes of the flow.

5.2 Azimuthal flows for all time sectors

We consider here 4 years of continuous CLY observations between 2013 and 2016, which is the entire dataset that was available to us at the time of the beginning of this study. The data have been first matched with information of the solar wind and IMF conditions. Our prime interest is on the IMF B_z and B_y components, as these are the base parameters used in various SuperDARN studies (e.g., Ruohoniemi and Greenwald [1996, 2005])

The IMF data were taken from the OMNI database, see Section 1.3. To accommodate the fact that some time is required for the solar wind disturbance to reach the high-latitude ionosphere from the bow shock (to which the OMNI data are set), a time delay of 8 min was introduced. This value was taken as an average for various conditions, in accordance with Jackel et al. [2010]. Data with one-minute resolution, for both CLY and OMIN, were considered. Because of some

uncertainty in the IMF propagation delay, there might be some mislabelling in assigning the radar data to a specific IMF bin, but because of the coarse binning we adopted, this only can be relevant for near zero values of the IMF. The IMF near zero values are not very frequent however in the database because the IMF has near zero values only in the course of transitions to various more steady states with non-zero values.

The CLY velocity data were assessed by computing hourly median values and binning with respect to the IMF. In this initial study we adopted a simple criteria: the data were selected according to the sign of IMF B_z (< 0 or > 0) and B_y (< 0 or > 0). Although this is very crude binning, it provides significant data coverage which is critical for summer observations when the CLY echo occurrence rates plummet by a factor of >3 as compared to winter time [Ghezelbash et al., 2014].

Figure 5.1 shows the azimuthal component of the polar cap flow velocity according to the CLY radar observations versus universal time (UT) for 48 consecutive months of observations. The observation zone is roughly at the magnetic latitude of $\sim 81°$.

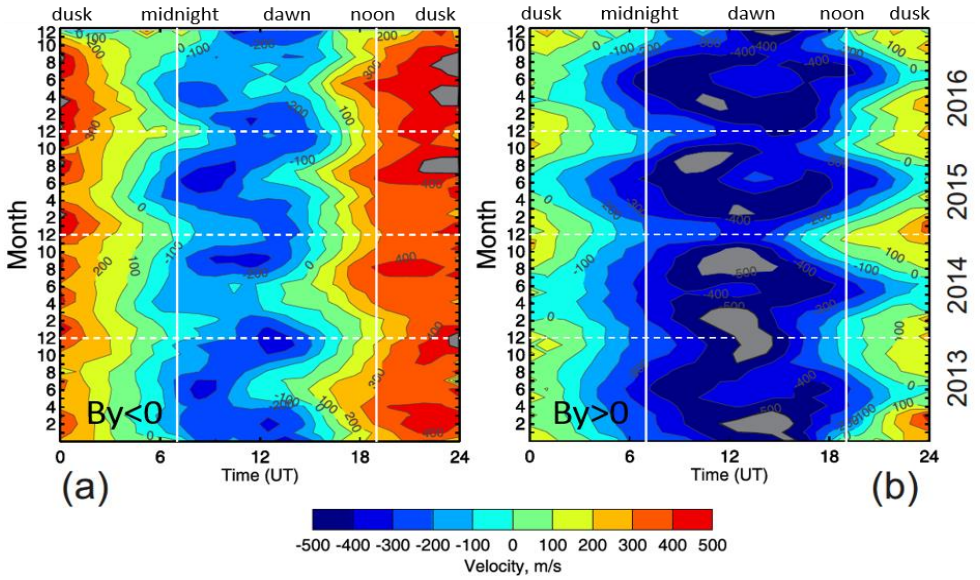

Figure 5.1: Color-contour plots of the azimuthal component of the polar cap flow velocity according to the Clyde River (CLY) radar (at magnetic latitude of $\sim 81°$) versus universal time (UT) for 48 consecutive months of observations in 2013-2016. (a) and (b) are for the IMF conditions $B_z \le 0, B_y \le 0$ and $B_z \le 0, B_y \ge 0$, respectively. The grey colored regions reflect domains where the velocity magnitude values are one step above the color bar shown at the bottom. Vertical lines correspond to magnetic midnight (~7 UT) and noon (~19 UT) for the area of echo detection.

Figures 5.1a and 5.1b are for the IMF conditions $B_z \le 0, B_y \le 0$ and $B_z \le 0, B_y \ge 0$, respectively. Vertical lines on both plots correspond to magnetic midnight (~7 UT) and noon (~19 UT) for the area of echo detection.

Both Figures 5.1a and 5.1b show a fairly consistent pattern in velocity change. Considering Figure 5.1a, prior to midnight, positive velocities are seen. Positive velocity implies the plasma flow toward the radar, away from magnetic noon on the MLAT-MLT plane, which is what is expected in the afternoon-dusk sector. Then, between 6-7 UT and 16-17 UT, velocities are negative, corresponding again to the ionospheric flow away from the magnetic noon. Later on, after passing the noon sector, the velocities are positive again. These changes of the velocity polarity reflect the fact that the radar monitors, on average, the 2-celled convection pattern with anti-sunward flow at dawn and dusk. This is precisely what one would expect for the plasma flow in the polar cap (Chapter 1). One interesting fact about velocity magnitudes in Figure 5.1a is that the magnitudes are larger in the dusk sector (~ 500 m/s) as compared to the dawn sector (~ 400 m/s), see grey colored "islands" for the data. The other feature of the data in Figure 5.1a is that the red contour color dominates over the pattern. Perhaps another feature is that the flow velocity magnitudes, while considering data over the same months, can be faster for IMF $B_y > 0$ at dawn and IMF $B_y < 0$ at dusk, which is consistent with previous SuperDARN reported observations as by Koustov et al. [2015].

Although Figure 5.1b for the IMF $B_y > 0$ shows a similar pattern in velocity changes versus UT, the details are quite different. First of all, one can see that here the blue contour color dominates. Secondly, the negative (dawn) velocity magnitudes are larger than those at dusk by ~ 200 m/s (300 m/s at dusk versus 500 m/s at dawn). The third obvious difference is that the transition to negative velocities starts earlier and ends later in UT, as compared to Figure 5.1a.

Both plots in Figure 5.1a, b show some summer-winter differences with this effect being more evident in Figure 5.1b for IMF $B_y > 0$. Here one can notice that during afternoon-dusk hours (20-24 UT), the transition of the negative velocity to the positive velocity starts much later in UT time in summer. One can also notice that during dusk-midnight hours (02-06 UT), the transition of the positive velocity to the negative velocity starts much earlier in UT time in summer. In effect, negative velocities last for much longer periods of the day in summer as compared to winter.

Data of Figure 5.1a for MIF $B_y < 0$ show that negative velocities last for much shorter periods of the day in summer as compared to winter. This is quite in contrast to the case of IMF $B_y > 0$ of Figure 5.1b.

The less obvious features of Figures 5.1a and 5.1b are as follows. The maxima in dawn velocity magnitudes seem to be often achieved during winter or close to equinox months for the case of IMF $B_y > 0$ (Figure 5.1b). This is also the case for the dusk velocity magnitudes. The data for IMF $B_y < 0$ (Figure 5.1a) shows local maxima in summer as well for dawn data and not clear preferential season for dusk.

5.3 Azimuthal flow differences at dawn and dusk

The data of Figure 5.1 are somewhat inconclusive if one wants to know the exact velocity values in a specific time sector, and thus conclude on the seasonal changes, because a minor car-box smoothing (3 values for a running average) was applied. Figure 5.2 gives a more precise assessment of the velocity magnitude seasonal changes for $B_y < 0$ and $B_y > 0$ in the dawn (10-14 UT, top panels) and dusk (20-24 UT, bottom panels) sectors.

Considering the dawn sector observations for IMF $B_y > 0$, panel (b), here velocity magnitudes in excess of 500 m/s occur predominantly in winter (2013-2014) or closer to equinoctial time (2015). For IMF $B_y < 0$, panel (a), velocity magnitudes up to 300 m/s occur predominantly in winter, while in summer the magnitudes drop down to ~ 100 m/s. This is consistent with Figure 5.1a where summer velocities at dawn are of large magnitudes at somewhat earlier time and of smaller magnitudes later on.

Now consider the dusk sector observations. For IMF $B_y < 0$, panel (c), velocity magnitudes enhancements to 400-500 m/s occur predominantly in winter and closer to equinoctial times, and the summer velocity magnitudes are less. For IMF $B_y > 0$, panel (d), velocity magnitudes up to 200-300 m/s occur predominantly in winter, while in summer the plot shows frequent occurrence of negative velocities of -500 m/s. On average, the velocity here can be negative or close to 0, and this is exactly what is seen in Figure 5.1b at dusk hours. Thus, we can conclude that the change in

the pattern of azimuthal flow occurs because, in summer, there is the frequent occurrence of the velocities with the polarity opposite to those expected for a standard 2-cell plasma flow pattern.

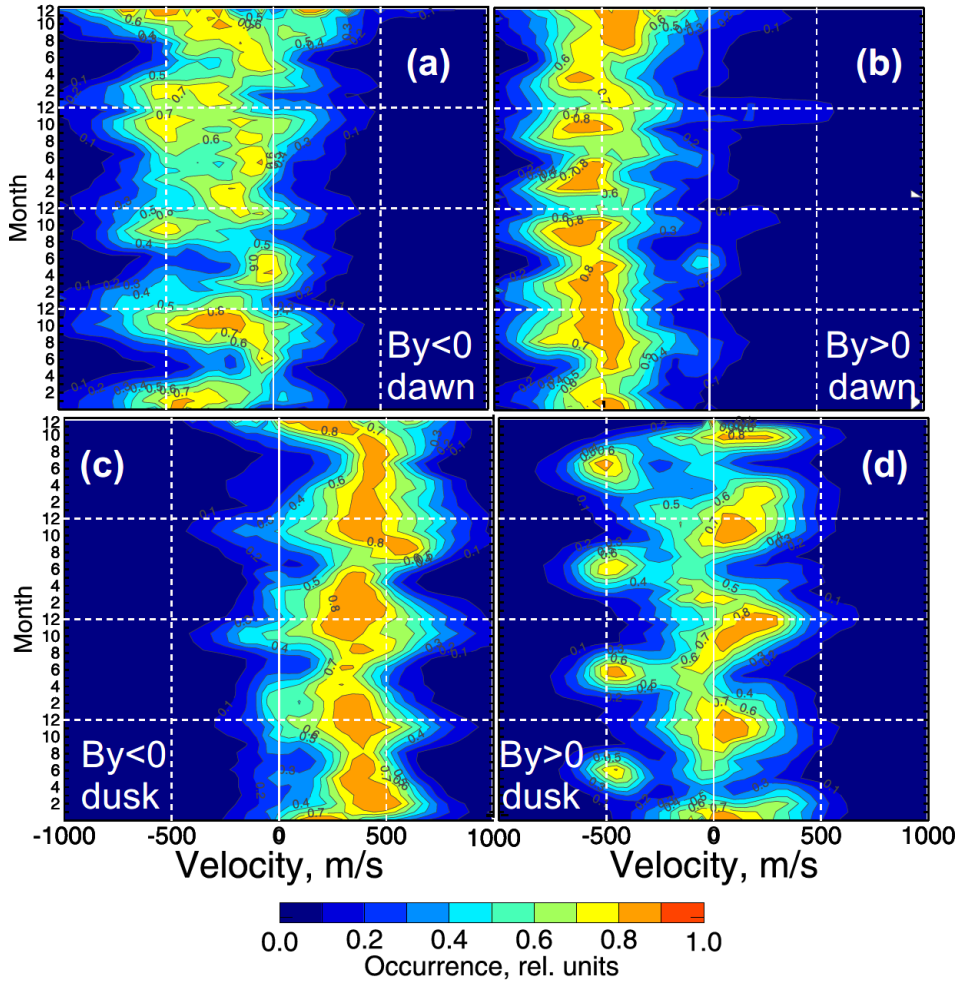

Figure 5.2: Color-contour plots of the occurrence of various velocities measured by the Clyde River (CLY) radar in the azimuthal direction (at magnetic latitude of ~ 81°) during 48 months of continuous observations in 2013-2016. (a) and (b) are the velocity averaged over dawn hours of 10-14 UT while (c) and (d) are the velocity averaged over dusk hours of 20-24 UT.

5.4 Summer-winter differences according to DMSP observations and CLY data

To be able to assess the above results on the seasonal variations in the polarity and intensity of the polar cap azimuthal plasma flows seen by the CLY radar, we discuss here results published by Rich and Hairston [1994]. These authors considered DMSP F8 and F9 measurements in the northern hemisphere during the period of September 1987 to December 1990 for the IMF condition

$5nT \leq |B_t| \leq 11nT$. These are somewhat larger values for the IMF as compared to our dataset for the period of relatively low Sun's activity, but these are the only data on seasonal change in plasma flow that we were able to find in literature.

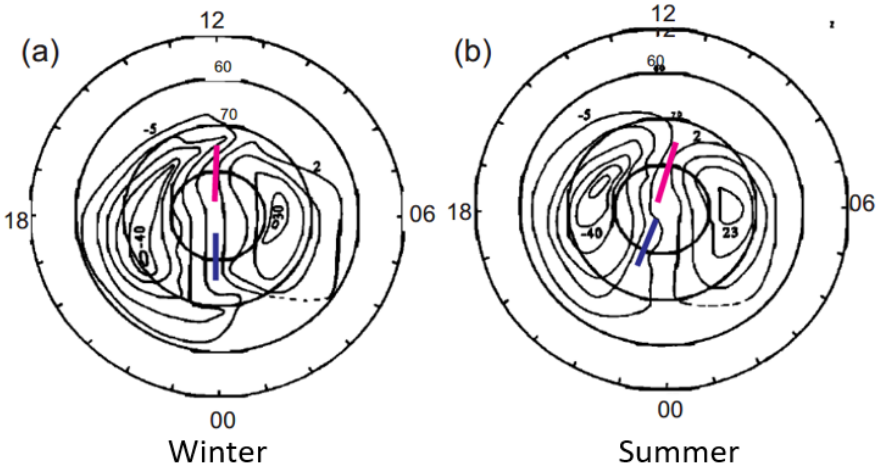

Figure 5.3: This plot is an adaptation of the original data presented by Rich and Hairston [1994]. Shown are contours of equal potential (with a step size of 7 kV, maximum and minimum values are shown by small characters) inferred from DMSP observations of the ion drift between September 1987 and December 1990. The data were selected whenever B_t was in between 5 and 11 nT, $B_z < 0$ and $B_y < 0$. In addition, the IMF clock angle was required to be around $135°$. Dashed lines denote those parts where no actual measurements were available. The pink and blue bars indicate MLT sectors where the flow is almost along magnetic meridians. Left panel (a) is for winter conditions, while right panel (b) is for summer conditions.

Figures 5.3a, b show contours of equal potential (with a step size of 7 kV), with maximum and minimum values marked by small characters, for IMF $B_z < 0$ and $B_y < 0$: (a) for winter and (b) summer. In addition, the IMF clock angle was required to be around $135°$. Both plots show a well developed 2-cell convection pattern although not of the same degree of symmetry. Contours of plasma motion (which is along the contours) in the central polar cap are within the smallest circle of $80°$ latitude. One can conclude that the flow here is mostly in the anti-sunward direction, which is consistent with the literature (e.g., Cousins and Shepherd [2010]). The foci of the convection cells are at about the same MLTs and MLATs in winter and summer, which disagrees with the ISR results by de la Beaujardiere et al. [1991], but a strong effect is not expected. Since the CLY radar monitors azimuthal flows, we marked in Figures 5.3a, b the MLTs when the flow is almost meridional on the dayside (the pink bars) and on the nightside (the blue bars). At these times, the CLY radar should measure nearly zero velocity.

Comparing winter and summer patterns in Figure 5.3a, b, one can conclude that the near-zero velocities should be observed at about ~ 24 MLT in winter and ~22 MLT summer on the nightside (the blue bars) and at about ~12 MLT in winter and ~ 11 MLT is summer for the dayside (the pink bars). Effectively, the cells rotate toward earlier MLT time in summer. These features imply that, in summer, the CLY radar would have to see a transition from negative to positive velocities several hours prior to the local magnetic noon and from positive to negative several hours prior to the local magnetic midnight. This is exactly what is observed in Figure 5.1a.

Figures 5.4a, b show contours of equal potential for IMF $B_z < 0$ and $B_y > 0$ (a) for winter and (b) summer. Here additionally, the IMF clock angle was required to be around $225°$. Both plots show a well developed 2-cell convection pattern as well. Here the cells are rotated toward pre-noon hours in winter and a more round pattern is seen in summer, which is quite apparent. Comparing winter and summer patterns in Figures 5.4a, b, one can conclude that near-zero velocities should be observed at about the same time of ~ 22 MLT in winter and ~ 21 MLT in summer on the nightside (the blue bars) and at about ~11 MLT in winter and ~ 14 MLT in summer for the dayside (the pink bars). These features imply that, in summer, the CLY radar would have to see a transition from negative to positive velocities on the dayside and from positive to negative velocities on the nightside several hours prior to the local magnetic noon and midnight, respectively. This is exactly what has been observed in Figure 5.1a for the dusk observations, but not for the dawn observations.

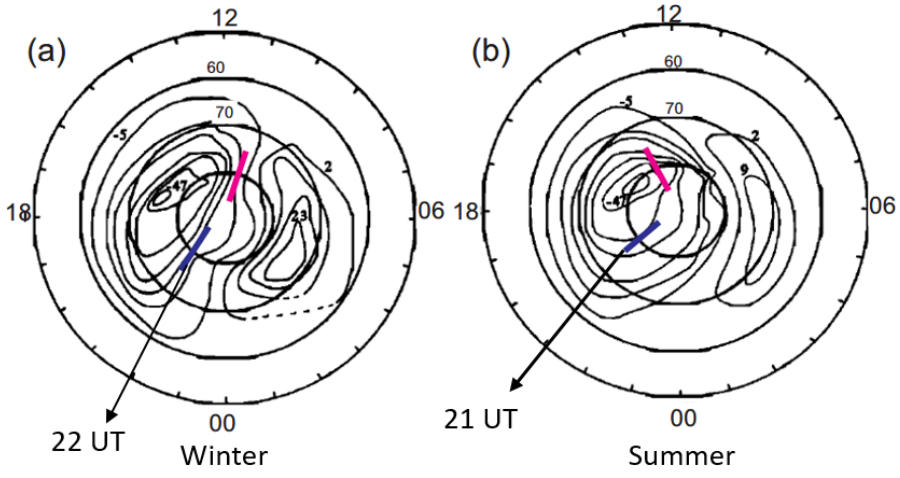

Figure 5.4: The same as in Figure 5.3 except for IMF $B_z < 0$ and $B_y > 0$. In addition, the IMF clock angle was required to be around $225°$.

One can conclude that the CLY data of Figure 5.1a, b are generally consistent with the DMSP data of Figures 5.3 and 5.4 as far as the times for velocity polarity change are considered. This implies that the summer high-latitude flow patterns for IMF $B_y > 0$ are more round than in winter and than for the patterns for IMF $B_y < 0$ in any season.

The other important observational conclusion for summer observations on frequent the occurrence of polar cap flows with the unexpected polarity, such as negative velocities of ~ -500 m/s on Figure 5.2d, does not fit the flow pattern presented in Figure 5.4b. One possible reason for this disagreement is the shift of the dusk convection cell toward the Pole so that the focus is located not at $80°$ as in Figure 5.2b, but at $81° - 82°$. Whether this is a correct interpretation requires 2-D plasma flow determination, which is beyond the current project.

5.5 Conclusions

Analysis of CLY data on the azimuthal component of the plasma flow in the polar cap at magnetic latitudes ~ $81°$ and IMF $B_z < 0$ shows that there are several noticeable changes from winter to summer, depending on the IMF B_y component involved. Over a day duration, summer flows are positive for more extended periods for IMF $B_y < 0$ and negative for more extended periods for the IMF $B_y > 0$. These observations can be interpreted as a result of summer flow patterns, especially for IMF $B_y > 0$, being more round. In terms of the flow velocity magnitudes, while considering data over the same months, the flows can be faster for IMF $B_y > 0$ as compared to those at $B_y < 0$ in the dawn sector, but the flows can be faster for IMF $B_y < 0$ as compared to those at $B_y > 0$ in the dusk sector. The winter-summer differences in the azimuthal component of plasma flow are not dramatic and, not surprisingly, no significant seasonal changes in the plasma flow patterns can be found while SuperDARN 2-D convection maps are considered. This is because the radar data are significantly smoothed while the plasma flow maps are being built.

CHAPTER 6

SUMMARY, CONCLUSIONS, AND SUGGESTIONS FOR FUTURE RESEARCH

In this Thesis, we focused on three themes, assessing HF velocity versus $\mathbf{E\times B}$ drift, reasons for PolarDARN velocity agreements with ISR drifts, and polar cap azimuthal plasma flows. We now summarize the major achievements in each of these themes and make suggestions for further expansion of the work done.

6.1 Assessing HF velocity versus $\mathbf{E\times B}$ drift

At present, comparisons of HF velocities with $\mathbf{E\times B}$ measurements by ISRs have been made extensively, covering a variety of time sectors, radar locations, and HF radar ranges. These measurements, including those reported in this thesis, unequivocally support the notion that the HF SuperDARN radars measure the $\mathbf{E\times B}$ l-o-s component reasonably well. In this thesis, we demonstrated, for the first time, that the CLY PolarDARN radar velocities (observed at ranges of ~900 km, in beam 5) are consistent with the eastward component of the $\mathbf{E\times B}$ drift derived from the RISR-C measurements of plasma flow. This result implies, on the other hand, that the RISR-C technique for the velocity pattern derivation by Heinselman and Nicolls [2008] works reasonably well despite some assumptions made.

We also showed that the agreement between the two types of radars is not ideal; the lines of linear fit had slopes in the range of 0.5-0.7, which is comparable with the slopes in other experiments, but slightly lower than usual. We showed that the correction of HF velocities for the index of refraction effect does not increase the slope of the line to 1 mostly because of still existing underestimation effect at large $\mathbf{E\times B}$ drifts of > 700 m/s. In addition, the underestimation effect was found to be stronger at nighttime and its compensation by considering the index of refraction effect was less successful than at daytime.

We hypothesized that bias in HF radar measurements occurs because HF radars get stronger signals from ionospheric regions with enhanced electron density where the electric field/ $\mathbf{E\times B}$ drift is decreased as compared to the background plasma. This hypothesis is consistent with

the presented data on the diurnal variation of the ratio of the HF velocity to the RISR velocity that shows a clear decrease during nighttime and not daytime.

Despite the generally positive outcome of our HF – RISR radars velocity comparisons, there are still issues that warrant further joint observations. One of these is the effects of lateral refraction for HF radio waves. Recent e-POP – SuperDARN experiments demonstrated that HF radio beams often experience significant lateral deviation [Perry et al., 2016]. In agreement with this notion, Koustov et al. [2016] presented one example of RKN-RISR observations when the HF velocity was well above the $\mathbf{E}\times\mathbf{B}$ component of the plasma drift for the area of the comparison. The effect lasted for tens of minutes and was explained by the lateral refraction of RKN beams. Since RISR-N and RISR-C measurements cover now latitudes both southward and poleward of Resolute Bay, there is a chance to isolate such events and test with the data whether the scenario of large lateral deviations of HF radio beams is realistic and investigate how often it happens.

Another important issue is the relationship between the velocity of E region echoes and the $\mathbf{E}\times\mathbf{B}$ drift. This relationship has not been discussed in this thesis because the CLY-RISR observations have been carried out at ranges of ~900 km from CLY where E region echoes are not expected. However, Gillies et al. [2018] demonstrated that the RKN radar shows occurrence of E region echoes at very far ranges, at ~2000 km, through the 1½ hop propagation mode. Such events are unique but very important to investigate because reasons for low velocity E region HF echoes are poorly understood.

6.2 Reasons for PolarDARN velocity disagreements with ISR drifts

The largest disagreements between HF and RISR velocities were found for periods with very low CLY and RKN velocities, below 100-200 m/s in magnitude. For many of these periods, the HF radars detected ground scatter echoes in one of the gates-beams adjacent to the considered beam/gate. We suggested that some ionospheric echoes could be misidentified by the FITACF technique. We noticed that the effect is more pronounced for the RKN radar.

We also noticed that in a case of highly-curved/distorted plasma flows, such as near the dayside reverse convection flows occurring under strong IMF $B_z > 0$, the differences between RISR and SuperDARN velocity vectors can be large. We hypothesized that an additional potential

reason for disagreement was violation of the assumption that the flows are uniformly affecting both systems.

One interesting conclusion of this thesis work is the HF radar velocity underestimation at large plasma drifts. For velocity magnitude < 500 m/s, the RISR-PolarDARN agreement was remarkably good, but at magnitudes above 700 m/s, HF velocities were smaller. It is interesting that a similar tendency is seen in the gate-by-gate comparison by Gillies et al. [2018], although it was not discussed in the paper. Koustov et al. [2016] reported the effect of smaller HF velocity magnitudes while considering the RISR-N and RKN and Inuvik (INV) data in three different comparisons, by comparing the data trends along the beams. In all three comparisons, the effect was seen for both westward and eastward drifts and existed after the correction of HF velocities for the index of refraction effect. No preferential time sector was identified. Importantly, the approaches to data comparison were quite different.

One possible explanation of this underestimation at large velocities is microstructure in plasma flows, as explained in section 3.8. This idea, however, cannot be tested with the currently available instruments. An alternative explanation was suggested by Dr. A. Reimer of the Stanford Research Institute, USA [Reimer et al., 2018]. He pointed out that the currently-employed FITACF procedure for derivation of the HF velocity relies on the linearity of the phase versus lag number curve. This condition is not always satisfied; the artificial shift of the phase at points with discontinuity of the phase (due to 2pi ambiguity in phase angle) often results in underestimated values. Ribeiro et al. [2012] noticed this tendency as well. This is a very attractive idea to pursue. Events with strong HF velocity underestimation can be easily identified for the dataset considered in this thesis.

Work with PolarDARN raw data can also shed light on the reasons for HF velocity misidentification. This is an old and general problem for SuperDARN experimentation. Again, events of ground scatter misidentification/contaminations are easy to identify in the database considered.

Work on both above effects is important, but unfortunately, it requires significant software development for the analysis of raw data (that have not been considered in this thesis). For this reason, such work is left for future efforts.

We also (Chapter 4) put effort in checking consistency between measurements of two PolarDARN radars, CLY and INV, looking in about the same scattering region but from opposite

directions. Our major goal was to evaluate if inconsistencies are related to the ranges of HF measurements. We did find evidence for importance of the range, but the scatter of the points was too significant to investigate the differences. Perhaps part of the problem is too large scattering volumes. Conducting joint observations with 15-km range gates would be interesting.

6.3 Polar cap azimuthal plasma flows

In this theme of the thesis, the work has been just started. We focused on one issue, seasonal variation of the velocity of flows in the azimuthal direction monitored by the CLY radar at a magnetic latitude of $\sim 81^\circ$. As demonstrated in Chapter 5, there is seasonal variation in plasma flow for IMF $B_z < 0$ depending on the polarity of B_y.

One important expansion of the work is consideration of velocity data in terms of external drivers, such as IMF B_y values. Other azimuthally-oriented SuperDARN radars, such as those at Longyearbyen in the Northern hemisphere and South Pole in the Southern hemisphere, are of interest as well. One important difference with the CLY radar is that these radars monitor echoes at $\sim 5^\circ$ lower geomagnetic latitudes and regularly detect flows from within the polar cusps. Unfortunately, data for Longyearbyen has just started arriving in the Saskatoon data center at the time of this thesis work. The South Pole data are not in abundance either, with significant gaps, so that seasonal variations are hard to investigate.

REFERENCES

Abooalizadeh, Z. (2015). Long-term variations in the high-latitude plasma flows inferred from SuperDARN radar data, MS thesis, Univ. of Saskatchewan, Saskatoon, Canada. (Available at http://hdl.handle.net/10388/ETD-2015-04-2041 (last access: September 2018))

Akbari, H., Bhatt, A., La Hoz, C., & Semeter, J. L. (2017). Incoherent scatter plasma lines: Observations and applications. *Space Science Reviews, 212*, 249–294, doi 10.1007/s11214-017-0355-7

Andre, D., Sofko, G. J., Baker, K., & MacDougall, J. (1998). SuperDARN interferometry: Meteor echoes and electron densities from groundscatter. *Journal of Geophysical Research, 103*, 7003; 7015

Axford, W. I., & Hines, C. O. (1961). A unifying theory of high-latitude geophysical phenomena and geomagnetic storms. *Canadian Journal of Physics, 39*, 1433–1464

Bahcivan, H., Tsunoda, R., Nicolls, M., & Heinselman, C. (2010). Initial ionospheric observations made by the new Resolute incoherent scatter radar and comparison to solar wind IMF. *Geophysical Research Letters, 37*, L15103, doi:10.1029/ 2010GL043632

Bahcivan, H., Nicolls, M. J., & Perry, G. (2013). Comparison of SuperDARN irregularity drift measurements and F-region ion velocities from Resolute bay ISR. *Journal of Atmospheric and Solar: Terrestrial Physics, 105-106*, 325–331

Baker, K.B. (2003). FITACF: SuperDARN Tutorial. SuperDARN workshop, Finland

Baumjohann, W., & Treumann, R. A. (1997). Basic Space Plasma Physics. *Imperial College Press, London, UK*

Cousins, E. D. P., & Shepherd, S. G. (2010). A dynamical model of high-latitude convection derived from SuperDARN plasma drift measurements. *Journal of Geophysical Research, 115* (12), doi:10.1029/2010JA016017

Cousins, E. D. P., & Shepherd, S. G. (2012). Statistical maps of small-scale electric field variability in the high-latitude ionosphere. *Geophysical Research Letters, 117*, A12304, doi:10.1029/2012JA017929

Crooker, N. U. (1992). Reverse convection. *Journal of Geophysical Research, 97*(A12), 19,363–19,372

Davies, J., Lester, M., Milan, S. E., & Yeoman, T. (1999). A comparison of velocity measurements from the CUTLASS Finland radar and the EISCAT UHF system. *Annales Geophysicae, 17*, 892–902

de la Beaujardiere, O., Alcayde, D., Fontanari, J., & Leger, C. (1991). Seasonal dependence of high-latitude electric fields. *Journal of Geophysical Research, 96*, 5723–5735

Diaz, M. A., Oppenheim, M., Semeter, J. L., & Zettergren, M. (2011). Particle-in-cell simulation of incoherent scatter radar spectral distortions related to beam-plasma interactions in the auroral ionosphere. *Geophysical Research Letters, 116*, A00K10, doi: 10.1029/2010JA016096

Dougherty, J., & Farley, D. (1960). A theory of incoherent scattering of radio waves by a plasma. *Proceedings of the Royal Society of London A: Mathematical, Physical and Engineering Sciences, 259*, 79–99

Dougherty, J. (1964). Model Fokker-Planck equation for a plasma and its solution. *The Physics of Fluids, 7* (11), 1788–1799

Drayton, R. A., Koustov, A. V., Hairston, M. R., & Villain, J.-P. (2005). Comparison of DMS cross-track ion-drifts and SuperDARN line-of-sight velocities. *Annales Geophysicae, 23*, 2479–2486

Dungey, J. W. (1961). Interplanetary magnetic field and auroral zones. *Physical Review Letters, 6*, 47–48

Eglitis, P., Robinson, T. R., Rietveld, M. T., Wright, D. M., & Bond, G. E. (1998). The phase speed of artificial field-aligned irregularities observed by CUTLASS during HF modification of the auroral ionosphere. *Geophysical Research Letters, 103*(A2), 2253–2259, doi:10.1029/97JA03233

Evans, J. (1969). Theory and Practice of Ionosphere Study by Thomson Scatter Radar: A review. *Proceedings of the IEEE, 57*(4), 496–530

Farley, D., Dougherty, J., & Barron, D. W. (1961). A theory of incoherent scattering of radio waves by a plasma. ii. Scattering in a magnetic field. *Proceedings of the Royal Society of London A: Mathematical, Physical and Engineering Sciences, 263*, 238–258

Fejer, J. (1960). Scattering of radio waves by an ionized gas in thermal equilibrium. *Canadian Journal of Physics, 38* (8), 1114–1133

Fejer, J. (1961). Scattering of radio waves by an ionized gas in thermal equilibrium in the presence of a uniform magnetic field. *Canadian Journal of Physics, 39* (5), 716–740

Fejer B. G., & Kelley, M. C. (1980). Ionospheric irregularities. *Reviews of Geophysics and Space Physics, 18*, 401–454

Folkestad, K., Hagfors, T., & Westerlund, S. (1983). EISCAT: An updated description of technical characteristics and operational capabilities. *Radio Science, 18*(6), 867–879, doi: 10.1029/RS018i006p00867

Förster, M., Paschmann, G., Haaland, S. E., Quinn, J. M., Torbert, R. B., Vaith, H., & Kletzing, C. A. (2007). High-latitude plasma convection from Cluster EDI: variances and solar wind correlations. *Annales Geophysicae, 25*, 1691–1707

Ghezelbash, M., Koustov, A. V., Themens, D. R., & Jayachandran, P. T. (2014). Seasonal and diurnal variations of PolarDARN *F* region echo occurrence in the polar cap and their causes. *Journal of Geophysical Research, 119*, doi:10.1002/2014JA020726

Gillies, R. G., Hussey, G. C., Sofko, G. J., McWilliams, K. A., Fiori, R. A. D., Ponomarenko, P., & St. Maurice, J.-P. (2009). Improvement of SuperDARN velocity measurements by estimating the index of refraction in the scattering region using interferometry. *Geophysical Research Letters, 114*, A07305, doi:10.1029/2008JA013967

Gillies, R. G., Hussey, G. C., Sofko, G. J., Wright, D. M., & Davies, J. A. (2010). A comparison of EISCAT and SuperDARN *F*-region measurements with consideration of the refractive index in the scattering volume. *Geophysical Research Letters, 115*, A06319, doi:10.1029/2009JA014694

Gillies, R. G., Hussey, G. C., Sofko, G. J., Ponomarenko, P. V., & McWilliams, K. A. (2011). Improvement of HF coherent radar line-of-sight velocities by estimating the refractive index in the scattering volume using radar frequency shifting. *Geophysical Research Letters, 116*, A01302, doi:10.1029/2010JA016043

Gillies, R. G., Hussey, G. C., Sofko, G. J., & McWilliams, K. A. (2012). A statistical analysis of SuperDARN scattering volume electron densities and velocity corrections using a radar frequency shifting technique. *Geophysical Research Letters, 117*, A08320, doi:10.1029/2012JA017866

Gillies, R. G., van Eyken, A., Spanswick, E., Nicolls, M. J., Kelly, J., Greffen, M., et al. (2016). First observations from the RISR-C incoherent scatter radar. *Radio Science, 51*, 1645–1659, doi:10.1002/2016RS006062

Gillies, R. G., Perry, G. W., Koustov, A. V., Varney, R. H., Reimer, A. S., Spanswick, E. St.-Maurice, J.-P., & Donovan, E. (2018). Large-scale comparison of polar cap ionospheric velocities measured by RISR-C, RISR-N, and SuperDARN. *Radio Science, 53,* 624–639, *d*oi: 10.1029/2017RS00643

Gorin, J. D., Koustov, A. V., Makarevich, R. A., St-Maurice, J.-P., & Nozawa, S. (2012). Velocity of E-region HF echoes under strongly-driven electrojet conditions. *Annales Geophysicae, 30,* 235–250, www.ann-geophys.net/30/235/2012/, doi:10.5194/angeo-30-235-2012

Greenwald, R. A., Baker, K. B., Dudeney, J. R., Pinnock, M., Jones, T. B., Thomas, E. C., et al. (1995). DARN/SUPERDARN: A global view of the dynamics of high-latitude convection. *Space Science Reviews, 71,* 761–796

Haaland, S., Paschmann, G., Förster, M., Quinn, J. M., Torbert, R. B., McIlwain, C. E., Vaith, H., Puhl-Quinn, P. A., & Kletzing C. A. (2007). High-latitude plasma convection from Cluster EDI measurements: method and IMF-dependence. *Annales Geophysicae, 25,* 239–253

Hagfors, T. (1961). Density fluctuations in a plasma in a magnetic field, with applications to the ionosphere. *Geophysical Research Letters, 66* (6), 1699–1712

Hairston, M. R., & Heelis, R.A (1990). Model of the high-latitude ionospheric convection pattern during southward interplanetary magnetic field using de 2 data. *Journal of Geophysical Research, 95* (A3), 2333–2343

Hanuise, C., Villain J.P., & Crochet, M. (1981). Spectral studies of F region irregularities in the auroral zone. *Geophysical Research Letters, 8*(10), 1083–1086

Hargreaves, J. K. (1992). The Solar-Terrestrial Environment. *Cambridge University Press, Cambridge, UK*

Heinselman, C. J., & Nicolls, M. J. (2008). A Bayesian approach to electric field and E-region neutral wind estimation with the Poker Flat Advanced Modular Incoherent Scatter Radar. *Radio Science, 43,* RS5013, doi:10.1029/ 2007RS003805

Heppner, J. P., & Maynard, N. C. (1987). Empirical high-latitude electric field models. *Geophysical Research Letters, 92,* 4467–4489

Jackel, B. J., McKiernan, B., & Singer, H. J. (2012). Geostationary magnetic field response to solar wind pressure variations: Time delay and local time variation. *Journal of Geophysical Research, 117*, A05203, doi:10.1029/2011JA017210

Kelley, M. C. (1989). The Earth's Ionosphere: Plasma Physics and Electrodynamics. *Academic Press, San Diego, California, US*

Kelley, M. C. (2009). The Earth's Ionosphere: Plasma Physics and Electrodynamics Second Edition. *Academic Press, San Diego, California, US*

Kivelson, M. G., & Russell, C. T. (1995). Introduction to Space Physics. *Cambridge University Press, Cambridge, UK*

Koustov, A. V., St-Maurice, J.-P., Sofko, G.J., Andre, D., McDougall, J. W., Hairston, M. R., Fiori, R. A., & Kadochnikov, G. E. (2009). Three-way validation of the Rankin Inlet PolarDARN radar velocity measurements. *Radio Science, 44*, RS4003, doi:10.1029/2008RS004045

Koustov, A. V., Fiori, R. A. D., & Abooalizadeh, Z. (2015). Long-term variations in the intensity of polar cap plasma flow inferred from SuperDARN. *Journal of Geophysical Research, 120*, 9722–9737, doi:10.1002/2015JA021625

Koustov, A. V., Lavoie, D. B. & Varney, R. H. (2016). On the consistency of the SuperDARN radar velocity and $\mathbf{E}\times\mathbf{B}$ plasma drift. *Radio Science, 51*, 1792–1805, doi:10.1002/2016RS006134

Koustov, A. V., Lavoie, D. B., Kouznetsov, A., Bourchill, J., & Knudsen, D. (2017). A Comparison of Swarm Cross-Track Ion-Drifts and SuperDARN Line-of-Sight Velocities. AGU Fall Meeting 2017, 11-15 December 2017, New Orleans, SA21A-2500

Koustov, A. V., Gillies, R. G., & Bankole, P. (2018). Validation of Clyde River SuperDARN radar velocity measurements with the RISR-C incoherent scatter radar. *Annales Geophysicae, 36*, 1657–1666, doi.org/10.5194/angeo-36-1657-2018

Lacroix, P.J., & Moorcroft, D.R. (2001). Ion acoustic HF radar echoes at high latitudes and far ranges. *Geophysical Research Letters, 106*, A12, 29091–29103

Liu, H. (2010). Study of the high-latitude ionosphere with the Rankin Inlet PolarDARN radar, M.Sc. Thesis, University of Saskatchewan, Saskatoon, Canada

Makarevich, R. A. (2008). HF radar observations of high-velocity *E* region echoes from the eastward auroral electrojet. *Journal of Geophysical Research*, *113*, A09321, doi: 10.1029/2008JA013204

Milan, S. E., Davies, J. A., & Lester, M. (1999). Coherent HF radar backscatter characteristics associated with auroral forms identified by incoherent radar techniques: A comparison of CUTLASS and EISCAT observations. *Geophysical Research Letters*, *104(A10*), 22591–22604, doi:10.1029/1999JA900277

Mori, D. (2011). SuperDARN cross polar cap potential and parameters of the near-earth space. MS thesis, Univ. of Saskatchewan, Saskatoon, Canada. (Available at https://ecommons.usask.ca/bitstream/handle/10388/ETD-2011-12-266/MORI-THESIS.pdf?sequence=3 (last access: September 2018))

Mori, D., Koustov, A. V., Jayachandran, P. T., & Nishitani, N. (2012). Resolute Bay CADI ionosonde drifts, PolarDARN HF velocities, and SuperDARN cross polar cap potential. *Radio Science, 47*, RS3003, doi:10.1029/2011RS004947

Nielsen, E., Whitehead, J.D., Hedberg, L.A., & Jones, T.B. (1983). A test of the cosine relationship using three-radar velocity measurements. *Radio Science, 18(2)0*, 230–236

Papitashvili, V. O., Belov, B. A., Faermark, D. S., Feldstein, Y. I., Golyshev, S. A., Gromova, L. I., & Levitin, A. E. (1994). Electric potential patterns in the northern and southern polar regions parameterized by the interplanetary magnetic field. *Journal of Geophysical Research, 99* (A7), 13,251–13,262

Parker, E. N. (1958). Dynamics of the interplanetary gas and magnetic fields. *Astrophysics Journal*, *128*, 664–676

Perry, G. W., James, H. G., Gillies, R. G., Hussey, G. C., McWilliams, K. A., St.-Maurice, J.-P., Ridley, C. & Yau A. W. (2015). The effect of plasma density structure on HF radio wave propagation at auroral and polar latitudes measured by e-POP. AGU Fall Meeting 2015, December 17, 2015, San Francisco, USA, paper SA42A-09

Pettigrew, E. D., Shepherd, S. G., & Ruohoniemi, J. M. (2010). Climatological patterns of high-latitude convection in the northern and southern hemispheres: Dipole tilt dependencies and interhemispheric comparisons. *Journal of Geophysical Research*, *115*, A07305, doi:10.1029/2009JA014956

Ponomarenko, P. V., Waters, C. L., & Menk, F. W. (2007). Factors determining spectral width of HF echoes from high latitudes. *Annales Geophysicae, 25*, 675–687, doi:10.5194/angeo-25-675-2007

Ponomarenko, P. V., St. Maurice, J.-P., Waters, C. L., Gillies, R. G., & Koustov, A.V. (2009). Refractive index effects on the scatter volume location and Doppler velocity estimates of ionospheric HF backscatter echoes. *Annales Geophysicae, 27*, 1–13, www.ann-geophys.net/27/1/2009

Ponomarenko, P.V., Koustov, A.V., St.-Maurice, J.-P., & Wiid, J. (2011). Monitoring the F-region peak electron density using HF backscatter interferometry. *Geophysical Research Letters, 38*, L21102, doi.org/10.1029/2011GL049675

Rees, M. H. (1989). Physics and chemistry of the upper atmosphere. *Cambridge and New York, Cambridge University Press*, 297 pages

Reiff, P. H., & Burch, J. L. (1985). IMF B*y*-dependent plasma flow and Birkeland currents in the dayside magnetosphere 2. A global model for northward and southward IMF. *Journal of Geophysical Research, 90*, 1595–1609

Reimer, A.S., Hussey, G. C., & McWilliams, K. A. (2018). Statistically self-consistent and accurate errors for SuperDARN data. *Radio Science, 53*, 93-111, doi:10.1002/2017RS006450

Ribeiro, A. J., Ruohoniemi, J. M., Baker, J. B. H., Clausen, L. B. N., Greenwald, R. A. & Lester, M. (2012), A survey of plasma irregularities as seen by the midlatitude Blackstone SuperDARN radar. *Journal of Geophysical Research, 117,* A02311, doi:10.1029/2011JA017207

Rich, F. J., & Hairston, M. (1994). Large-scale convection patterns observed by DMSP. *Journal of Geophysical Research, 99* (A3), 3827–3844

Richmond, A. D. (1992). Assimilative mapping of ionospheric electrodynamics. *Advances in Space Research, 12* (6), 59–68

Richmond, A. D., & Kamide, Y. (1988). Mapping electrodynamic features of the high-latitude ionosphere from localized observations: technique. *Journal of Geophysical Research, 93* (A6), 5741–5759

Rishbeth, H., & Garriott, O. (1969). Introduction to ionospheric physics. *Springer*

Rosenbluth, M., & Rostoker, N. (1962). Scattering of electromagnetic waves by a nonequilibrium plasma. *The Physics of Fluids, 5* (7), 776–788

Ruohoniemi, J. M., Greenwald, R. A., Baker, K. B., Villain, J.-P., & McCready, M. A. (1987). Drift motions of small-scale irregularities in the high-latitude F region: An experimental comparison with plasma drift motions. *Geophysical Research Letters, 92,* N5, 4553–4564

Ruohoniemi, J. M., & Greenwald, R. A. (1996). Statistical patterns of high-latitude convection obtained from Goose Bay HF radar observations. *Journal of Geophysical Research, 101* (A10), 22,743–21,763, doi:10.1029/96JA01584

Ruohoniemi, J. M., & Baker, K.B. (1998). Large-scale imaging of high-latitude convection with Super Dual Auroral Radar Network HF radar observations. *American Geophysical Union, 103,* (A9), 20,797–20811, doi:10.1029/98JA01288

Ruohoniemi, J. M., & Greenwald, R. A. (2005). Dependencies of high-latitude plasma convection: Consideration of interplanetary magnetic field, seasonal, and universal time factors in statistical pattern. *Journal of Geophysical Research, 110* (A09204), doi:10.1029/2004JA010815

Salpeter, E. (1961). Plasma density fluctuations in a magnetic field. *Physical Review*, *122* (6), 1663

Salpeter, E. (1960). Electron density fluctuations in a plasma. *Physical Review, 120* (5), 1528

Sarno-Smith, L. K., Kosch, M. J., Yeoman, T. K., Rietveld, M., Nel, A., & Liemohn, M. W. (2016). Ionospheric electron number densities from CUTLASS dual-frequency velocity measurements using artificial backscatter over EISCAT. *Geophysical Research Letters, 121,* 8066–8076, doi:10.1002/2016JA022788

Schlegel, K. (1996). Coherent backscatter from ionospheric E-region plasma irregularities. *Journal of Atmospheric and Solar-Terrestrial Physics, 58,* 933–941

Sonett, C.P., Judge, D.L., Sims, A.R., & Kelso, J.M. (1960). A radial rocket survey of the distant geomagnetic field. *Journal of Geophysical Research, 65*(1), 55–67, doi:10.1029/JZ065i001p00055

Spaleta, J., Bristow, W.A., & Klein, J. (2015). Temporal and spatial resolved SuperDARN line of sight velocity measurements corrected for plasma index of refraction using Bayesian inference. *Geophysical Research Letters, 120,* 3207–3225, doi: 1002/2014JA020960

Tsunoda, R. T. (1988). High latitude F region irregularities: A review and synthesis. *Reviews of Geophysics, 26,* 719–760

Uspensky, M.V., Koustov, A. V., Williams, P. J. S., Huuskonen, A., Kangas, J., & Nielsen, E. (1989). Effect of unresolved electrojet microstructure on measurements of irregularity drift velocity in auroral radar backscatter. *Advances in Space Research, 9*, 119–122

Uspensky, M. V., Koustov, A. V., Sofko, G. J., Koehler, J. A., Villain, J.P., Hanuise, C., Ruohoniemi, J. M., & Williams, P. J. S. (1994). Ionospheric refraction effects in slant range profiles of auroral HF coherent echoes. *Radio Science, 29* (2), 503–517, doi:10.1029/93RS03256

Villain, J.P., Caudal, G., & Hanuise, C. (1985). A SAFARI-EISCAT comparison between the velocity of F region small-scale irregularities and the ion drift. *Geophysical Research Letters, 90* (A9):8433–8443

Villain, J. P., Greenwald, R.A., Baker, K.B., & Ruohoniemi, J.M. (1987). HF radar observations of E region plasma irregularities produced by oblique electron streaming. *Geophysical Research Letters, 92*, 12,327–12,342

Villain, J. P., Andre, R., Hanuise, C., & Gresillon, D. (1996). Observation of the high latitude ionosphere by HF radars: interpretation in terms of collective wave scattering and characterization of turbulence. *Journal of Atmospheric and Solar: Terrestrial Physics, 58*, N8–9, 943

Watanabe, M., & Sofko, G. J. (2009). The interchange cycle - a fundamental mode of magnetic flux circulation for northward interplanetary magnetic field. *Geophysical Research Letters, 36* (L03107), doi:10.1029.2008GL036682

Weimer, D. R. (1995). Models of high-latitude electric potentials derived with a least error fit of spherical harmonic coefficients. *Journal of Geophysical Research, 100* (A10), 19,595–19,607

Wiener, N. (1964). Time Series. M.I.T. Press, Cambridge, Massachusetts. p. 42

Woodman, R. F. (1967). Incoherent scattering of electromagnetic waves by a plasma, PH.D. Thesis, Harvard University. American Doctoral Dissertations, Source code: X1967, 0202

Xu, L., Koustov, A.V., Thayer, J., & McCready, M. (2001). SuperDARN convection and Sondrestrom plasma drift. *Annales Geophysicae, 19* (7), 749–759

Xu, L. (2003). SuperDARN-derived plasma convection: Comparison with other data and application to field-aligned current measurements, Ph.D. Thesis, U of Saskatchewan, Saskatoon, Canada

Xu, L., Koustov, A.V., Xu, J. S., Drayton, R. A., & Huo, L. (2008). A 2-D comparison of ionospheric convection derived from SuperDARN and DMSP measurements. *Advances in Space Research, 42*, 1259–1266, doi:101016/j.asr.2007.06.044

Yamazaki, Y., Kosch, M. J., & Ogawa, Y. (2017). Average field-aligned ion velocity over the EISCAT radars. *Geophysical Research Letters, 122*, 5630–5642, doi: 10.1002/2017JA023974